AN ON-BODY WEARABLE AND FLEXIBLE ANTENNA BASED WIRELESS MONITORING SYSTEM FOR THE DETECTION OF PULMONARY EDEMA

by

Uzay Bengi

B.S., Electrical Electronics Engineering, Boğaziçi University, 2020

Submitted to the Institute for Graduate Studies in
Science and Engineering in partial fulfillment of
the requirements for the degree of
Master of Science

Graduate Program in Electrical Electonics Engineering
Boğaziçi University
2024

AN ON-BODY WEARABLE AND FLEXIBLE ANTENNA BASED WIRELESS MONITORING SYSTEM FOR THE DETECTION OF PULMONARY EDEMA

APPROVED BY:

Assoc. Prof. Sema Dumanlı Oktar . . . .
(Thesis Supervisor)

Assoc. Prof. Ahmet Öncü . . . .

Assoc. Prof. Tuba Yılmaz Abdolsaheb . . . .

DATE OF APPROVAL: 16.04.2024

ACKNOWLEDGEMENTS

I would like to express my deepest gratitude to my advisor, Sema Dumanlı Oktar. Throughout my thesis journey, I have always felt her unwavering support, guidance, and mentorship by my side. Her dedication, expertise, and patience have been invaluable in shaping not only my academic but also my personal growth. Dr. Dumanli's insightful feedback and encouragement have been the main instrumental in helping me achieve my goals and complete this endeavour successfully. Since my senior year of bachelor's at Bogazici University, I have thought that I am truly fortunate to have had such a dedicated and inspiring advisor. I will always be thankful for her contributions to my education and development.

I would like to show my appreciation to Assoc. Prof. Ahmet Öncü and Assoc. Prof. Tuba Yılmaz Abdolsaheb for their valuable presence on my thesis committee. Also, I extend my appreciation to our collaborators Kamran Sayrafian and Katjana Ladic from NIST for their great contribution.

Additionally, I love my laboratory, BOUNTENNA. Every member of my lab has always been so kind to me and made me feel like I am with my family. I will always carry the amazing memories with them in my heart for the rest of my life. I extend my sincere gratitude to Ahmet Bilir, Anıl Tülü, Burak Ferhat Özcan, and Mehmet Emre Korkmaz, the invaluable backbone of BOUNTENNA, for their tremendous support throughout the fabrication and measurement phases of my project.

In this tough journey, I have incredibly supportive friends. I want to show my appreciation to Ayşegül Beril Acar, Merve Görkem Durmaz, Ozan Furkan Sezgen, and Zeynep Yetişken for always being there when I need them. Finally, I would like to express my deepest love to my parents Sevgi and Barkım for their endless support, encouragement, and love. I am dedicating my thesis to them.

ABSTRACT

AN ON-BODY WEARABLE AND FLEXIBLE ANTENNA BASED WIRELESS MONITORING SYSTEM FOR THE DETECTION OF PULMONARY EDEMA

Pulmonary edema(PE) is a medical condition characterized by the accumulation of excess fluid in the lungs, which can impair respiration by filling up the tiny air sacs called alveoli with saline. PE may turn into acute respiratory distress syndrome(ARDS), a severe form of lung failure with a mortality rate of 40%. PE can be detected by imaging modalities such as chest X-ray, and magnetic resonance imaging(MRI), as well as biomarkers like B-type Natriuretic Peptide(BNP). Furthermore, there has been a growing interest in utilizing wearable sensors and antennas within Wireless Body Area Network (WBAN) systems for PE detection. These WBAN applications analyze changes in dielectric properties of the human body to identify the presence of PE. This thesis introduces an alternative approach that combines localization and severity analysis using on-body antenna arrays placed on the anterior and posterior torso. The proposed antennas are fabricated on a novel High-Permittivity Flexible Substrate(HPFS). HPFS provides the desired miniaturization of the antenna due to its high permittivity and it also satisfies the user acceptance with high flexible and conformable nature. The antenna fabricated on HPFS is a coplanar waveguide(CPW) fed loop antenna operating in the Medical Implant Communication System(MICS) band. The thesis conducts a series of analyses in the numerical model, including localization and severity analyses of PE. Subsequently, the measurement setup is established, including the tissue-mimicking phantoms. Besides the measurements in the realized setup, another group of measurements on the human body is conducted for deeper analysis. Finally, the simulation and measurement results are discussed.

ÖZET

PULMONER ÖDEM TESPİTİ İÇİN BEDEN ÜSTÜ GİYİLEBİLİR VE ESNEK ANTEN TABANLI KABLOSUZ İZLEME SİSTEMİ TASARIMI

Pulmoner ödem(PE), akciğerlerde fazla sıvı birikimiyle karakterize edilen bir tıbbi durumdur, bu durum solunumu etkileyerek alveoller olarak adlandırılan küçük hava keseciklerini salinle doldurabilir. PE akut solunum sıkıntısı sendromuna(ARDS) dönüşebilir; ARDS %40 ölüm oranına sahip ciddi bir akciğer yetmezliği şeklidir. PE, göğüs röntgeni ve manyetik rezonans görüntüleme(MRG) gibi görüntüleme yöntemleri, ayrıca B-tipi natriüretik peptid(BNP) gibi biyobelirteçlerle tespit edilebilir. Ayrıca, PE varlığını belirlemek için Kablosuz Vücut Alanı Ağı(WBAN) sistemlerinde giyilebilir sensörler ve antenlerin kullanımına yönelik artan bir ilgi bulunmaktadır. Bu WBAN uygulamaları, PE'nin varlığını belirlemek amacıyla insan vücudunun dielektrik özelliklerindeki değişiklikleri analiz eder. Bu tez, ön ve arka gövdeye yerleştirilen vücut üstü anten dizilerini kullanarak lokalizasyon ve şiddet analizini bir araya getiren alternatif bir yaklaşımı tanıtır. Önerilen antenler, yüksek dielektrik sabitine sahip Yüksek-Dielektrik Sabitli Esnek Alttaş(YDEA) üzerinde üretilmiştir. YDEA, yüksek dielektrik sabitine sahip olması nedeniyle antenin istenilen minyatürleştirmesini sağlar ve ayrıca kullanıcı kabulünü, esnek ve uyarlanabilir yapısıyla karşılar. YDEA üzerinde üretilen anten, Tıbbi İmplant İletişim Sistemi(MICS) bandında çalışan bir eş düzlemli dalga kılavuzu(CPW) beslemeli halka antendir. Tezde, sayısal model üzerinde PE'nin lokalizasyon ve şiddet analizini içeren bir dizi analiz yapılmıştır. Bundan sonra, doku taklit eden fantomlar da dahil olmak üzere ölçüm düzeni üretilir. Gerçekleştirilen ölçüm düzenindeki ölçümlerin yanı sıra, daha derin bir analiz için insan vücudunda başka bir grup ölçüm yapılır. Son olarak, benzetim ve ölçüm sonuçları tartışılır.

TABLE OF CONTENTS

LIST OF FIGURES

LIST OF TABLES

LIST OF SYMBOLS

C	Circumference
c	Speed of light
E	Electric field
ff	Filling factor
H	Magnetic field
k	Wavenumber
P_{rad}	Radiated power
q	Partial filling factor
R_r	Radiation resistance
$\tan\delta$	Loss tangent
W	Power density
Z_0	Characteristic impedance
ϵ_r	Relative permittivity(Dielectric Constant)
ϵ_{eff}	Effective permittivity
η	Wave impedance
κ	Power per unit volume expanded with significance order
λ	Wavelength
λ_0	Free space wavelength
λ_g	Guided wavelength
σ	Electrical conductivity
ψ	Significance order

LIST OF ACRONYMS/ABBREVIATIONS

ARDS	Acute Respiratory Distress Syndrome
BNP	B-type Natriuretic Peptide
CPW	Coplanar Waveguide
CT	Computed Tomography
EIT	Electrical Impedance Tomography
HPFS	High-Permittivity Flexible Substrate
Hz	Hertz
ISM	Industrial, Scientific, and Medical
MedRadio	Medical Device Radiocommunications Service
MICS	Medical Implant Communication System
MRI	Magnetic Resonance Imaging
NaCl	Sodium Chloride
NaN_3	Sodium Azide
PDMS	Polydimethylsiloxane
PE	Pulmonary Edema
PET	Positron Emission Therapy
SAR	Specific Absorption Rate
SLA	Stereolithography
VNA	Vector Network Analyzer
UWB	Ultra-Wideband
WBAN	Wireless Body Area Network
WHO	World Health Organization

1. INTRODUCTION

In the contemporary landscape, there is an increasing requirement for comprehensive healthcare services globally due to population growth. A report jointly published by the World Health Organization(WHO) and the World Bank in December 2017 highlighted a significant gap, with half of the world's population lacking essential healthcare services. Also, the same report revealed that over 100 million people had been suffering from extreme poverty because of the expenses of these services [1]. Besides the lack of healthcare services, frequent or immediate access to health-related facilities might not be possible for children, the elderly population, pregnant women, people with disabilities, or those living in remote areas [2]. Therefore, there has been growing attention towards enhancing healthcare infrastructure for everyone through the integration of applications within Wireless Body Area Network(WBAN) systems [3]. Additionally, the COVID-19 pandemic has further demonstrated the importance of improving remote, noninvasive, and easily accessible telehealth applications.

WBAN systems offer a diverse array of healthcare services, encompassing vital sign monitoring, medical equipment control, diagnostic capabilities, real-time health status surveillance, and more [4]. These systems can incorporate implantable medical devices such as pacemakers, neurostimulators [5], and smart implants as well as wearable sensors and antennas. Notably, WBAN applications make use of designated frequency bands including the Medical Implant Communication System(MICS), Industrial Scientific Medical(ISM), Medical Device Radiocommunications Service(MedRadio), and Ultra-Wideband(UWB) to facilitate their functions. These allocated frequency bands are essential for the effective operation and coordination of WBAN systems within the healthcare domain. In the context of healthcare, WBAN technology has proven to be a valuable asset in the monitoring and early detection of various medical conditions as previously noted. Among these medical conditions, Pulmonary Edema(PE) which is a common symptom of pulmonary disorders, requires specific attention.

1.1. General View of Pulmonary Edema

PE is a medical condition characterized by excess fluid buildup in the human lungs. Numerous alveoli, which are responsible for respiration, exist at the end of bronchioles and become adversely influenced by the accumulation of fluid. Briefly, the presence of additional fluid in the lungs fills up alveoli and impairs respiratory function by affecting the exchange of carbon dioxide and oxygen [6]. Although there are many reasons for PE, they can be divided into two fundamental types which are cardiogenic and noncardiogenic PE [7]. Cardiogenic PE emanates from circulatory system-related issues and patients with this condition are mostly treated with diuretics and load reduction [8]. Distinctively, noncardiogenic PE might derive from various reasons such as congestive heart failure, physical damage to lung tissue, exposure to some toxins and drugs, and infections of bacteria, viruses, and fungi [9]. The illustration for physiological comparison between healthy lung, lung with cardiogenic PE, and lung with noncardiogenic PE is given in Figure 1.1. Unless early diagnosis and necessary treatment are not provided, PE may turn into acute respiratory distress syndrome (ARDS), a form of lung failure. Even though there has been detailed research and considerable progress in understanding the physiology and epidemiology of ARDS, mortality still remains at around %40 [10].

1.2. Detection Techniques of Pulmonary Edema

Particularly since the ARDS was initially defined in 1967, PE has been attracting attention due to its potential for severe damage including fatal outcomes [11]. The early and accurate diagnosis of PE is the keystone to mitigate consequential morbidity and mortality. Therefore, extensive research and applications have been conducted over the past five decades in order to advance detection and treatment methods. In addition to conventional approaches such as chest X-ray, computed tomography(CT) scan, electrical impedance tomography(EIT), etc., there are also novel emerging methods.

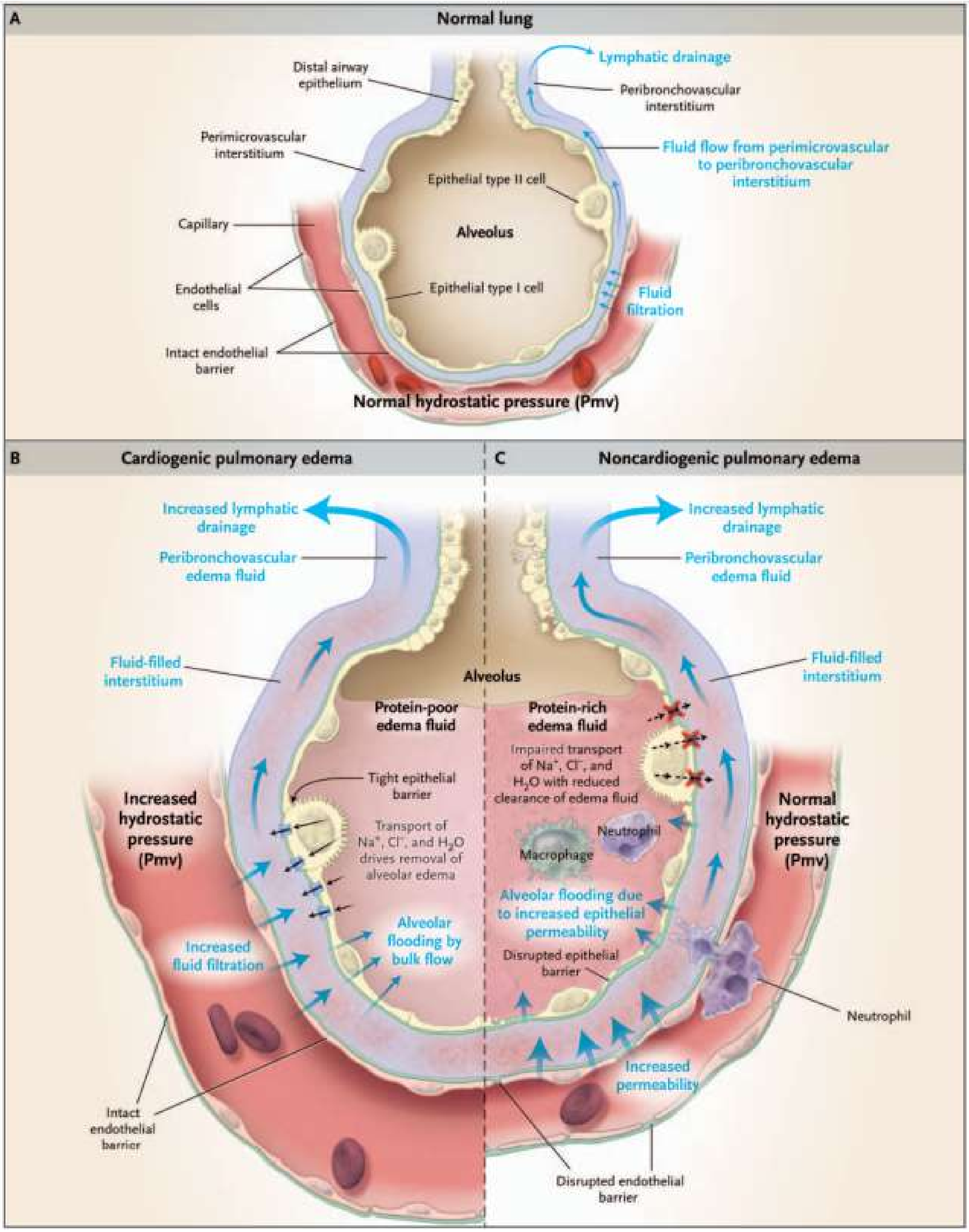

Figure 1.1. Physiology of fluid exchange in alveoli for healthy lung, lung with cardiogenic PE, and lung with noncardiogenic PE [7].

1.2.1. Detection by Imaging Modalities

One of the enduring and still used methods used by clinicians is analyzing chest X-rays. It is known that chest X-rays track fluid accumulation in the lungs by revealing interstitial and alveolar opacities [12]. However, it is crucial to note that chest X-rays utilize ionizing radiation which may induce mutation in human cells, thereby carrying a risk of cancer onset [13]. In contrast to chest X-ray, positron emission therapy(PET), magnetic resonance imaging(MRI), CT scan, and EIT offer a less risky detection due to their low-radiation or radiation-free imaging. PET, MRI, and CT scans facilitate the identification of the interstitial changes based on the opacities of the images so that clinicians can detect even minimal fluid changes and perform quantitative measurements [14]. Distinctly, EIT focuses on the internal conductivity distribution obtained by the input-output voltage patterns in order to generate images [15]. Analyzing the conductivity distribution, it is not only possible to measure lung water ratio, indicating the severity of PE, but also the localization of the fluid could be achieved [16]. Nevertheless, these techniques do not provide the information rapidly; a relatively long measurement time is necessary, and they are applied via non-portable heavy pieces of equipment [17]. Due to their lack of portability, long measurement time, and the need for trained experts, it is indispensable for patients to access such medical facilities.

1.2.2. Detection by Biomarkers

The presence of PE has severe impacts on the human body, potentially leading to fatal outcomes without treatment. Consequently, it disrupts the chemical balance within the body. Tracking the associated chemicals enables scientists to detect PE through chemical-based methods. To be exemplified, the B-type Natriuretic Peptide (BNP) level in blood is one of the most fluctuating ratios in the case of acute heart failure. Therefore, it has been demonstrated that elevated levels of BNP could be correlated with the presence of PE [18]. Additionally, tracking the B-lines observed in lung ultrasonography is accepted as another biomarker. B-line artefacts are a part of pathological condition that occurs in the case of increased lung density [19]. Therefore, they are used in both detecting pulmonary congestion in patients and assigning scores for disease severity [20, 21].

1.2.3. Detection by WBAN Monitoring Systems

With growing interest and improved research techniques, the utilization of wearable sensors and antennas within the WBAN framework for the detection of PE is gaining attention. Many new approaches and applications have emerged in the literature for easy-to-use and noninvasive detection, despite encountering challenges such as ensuring system robustness, maintaining good sensing quality, achieving low-cost production, extending battery life, and ensuring user acceptance [22]. The PE condition is detected by analyzing the changing dielectric properties of the human body in most of the proposed approaches. Therefore, it should be emphasized that the frequency-dependent dielectric property analysis of the human body is indispensable.

Dielectric properties of the human body have been studied by many researchers; nevertheless, these properties are measured via dielectric probes and it is not possible to use them on living tissues [23]. Therefore, freshly deceased animal tissues or human autopsies are used to estimate approximate dielectric properties [24]. The relationship between frequency and dielectric properties of the human body is detailed by IT'IS foundation, covering a frequency range from 10 Hz to 100 GHz [25] by using Gabriel dispersion relationships provided in [24].

Human body tissues could be evaluated as layers with varying thicknesses and compositions. To be exemplified, tissues like the brain, muscles, eyes, and kidneys have high water content, making them layers with high conductivity and high permittivity. On the other hand, tissues with lower water content such as fat, skin, and bones, are layers with low conductivity and low permittivity. Since dielectric properties are influenced by the frequency of electromagnetic waves, it is anticipated to observe distinct levels of absorption at different resonant frequencies as these waves pass through the body [26]. In Table 1.1, the dielectric properties of some body tissues at different frequencies are shown.

Table 1.1. Relative permittivity(ϵ_r) and electrical conductivity(σ) values of some body tissues at 403 MHz and 2.4 GHz.

	403 MHz		**2.4 GHz**	
Tissue	$\boldsymbol{\epsilon_r}$	$\boldsymbol{\sigma}$ **(S/m)**	$\boldsymbol{\epsilon_r}$	$\boldsymbol{\sigma}$ **(S/m)**
Brain	55.90	1.03	44.90	2.07
Bone (Cancellous)	22.40	0.235	18.6	0.788
Eye (Cornea)	59.20	1.19	51.70	2.26
Fat	11.60	0.081	10.80	0.261
Kidney	66.30	1.10	52.90	2.39
Lung (Deflated)	54.5	0.684	48.5	1.65
Lung (Inflated)	23.8	0.375	20.5	0.790
Muscle	57.10	0.797	52.80	1.71
Skin	46.70	0.689	38.10	1.44

In cases of PE, the fluid accumulating in the patient's lungs is referred to as saline, constituting a solution of sodium chloride(NaCl) and water. The saline build-up in the alveoli alters the overall density, permittivity, and conductivity of lung tissue. The detailed calculation for density is explained in [2] and the formulation of dielectric properties within the temperature range of 5-35° is validated in [27]. Additionally, assuming the validity of the estimation in [27], the dielectric properties of saline are calculated to be 72.47 in permittivity and 1.86 (S/m) in conductivity [2]. Considering the influence of saline on the properties of lung tissue, there are plenty of proposals for detection in WBAN systems discussed in the literature [28–48]. A comparison between the proposed detection method and the other closely related ones is given in Figure 1.2.

Fundamentally, techniques within WBAN for detecting PE can be divided into two categories which are sensing and imaging. Despite both aiming to detect PE, there is a trade-off between them. While sensing approaches are more compatible with on-body use which satisfies user acceptance, imaging techniques provide deeper information about PE. In order to make the implementation of designs on portable or wearable devices easier, on-body sensing approaches are exemplified in [28–35]. More primitive works only used for detection are given in [28, 29] which are the utilization of acoustic waves and the design of a microwave stethoscope respectively. Recent works utilize transmission analysis across multiple devices [30–34]. The detection of PE is confirmed by reduced signal power in [30], while other works assess both detection and severity by evaluating transmitted signal levels [31–34]. Differing from the mentioned ones, another work involves a 16-port on-body sensor estimating the dielectric properties of lung tissue through reflection coefficients, enabling both detection and severity analysis [35]. Furthermore, there are also sensing approaches that are not utilized for on-body applications. To be exemplified, in one of the early studies employing transmission analysis between off-body horn antennas, it is found that the location of the standing wave node may indicate the presence of fluid in the lungs [36]. Additionally, another work compares transmission and reflection analysis for PE detection and demonstrated that transmission analysis can detect both PE and the level of accumulated fluid [38].

The studies employing the imaging approach tend to be bulkier and require a computer with a suitable display algorithm [39–48]. A non-portable on-body antenna array system embedded in foam is suggested in [39]. This system analyzes signals reflected back to the array members to compute dielectric properties and attempts to create images of the lungs based on changes in these properties. Differing from the other imaging techniques, the works proposed in [40, 41] use transmitted signals between the antennas positioned around the body and calculate the dielectric properties of the lung tissue by using transmission parameters. Then, the derived properties are used in imaging, which facilitates both localization and severity analysis. Other exemplified works on microwave imaging of PE use reflected signals for severity analysis and localization. For instance, an antenna array system is proposed to detect and analyze PE by estimating the dielectric properties of malignant lung tissue [42–44]. Additionally, it is demonstrated that processing the reflected signal powers with algorithms is another way of imaging in [45–47]. Lastly, another antenna array system, aided by a metasurface, is presented in [48]. Its purpose is to compare reflected signal levels for localization without conducting any severity analysis.

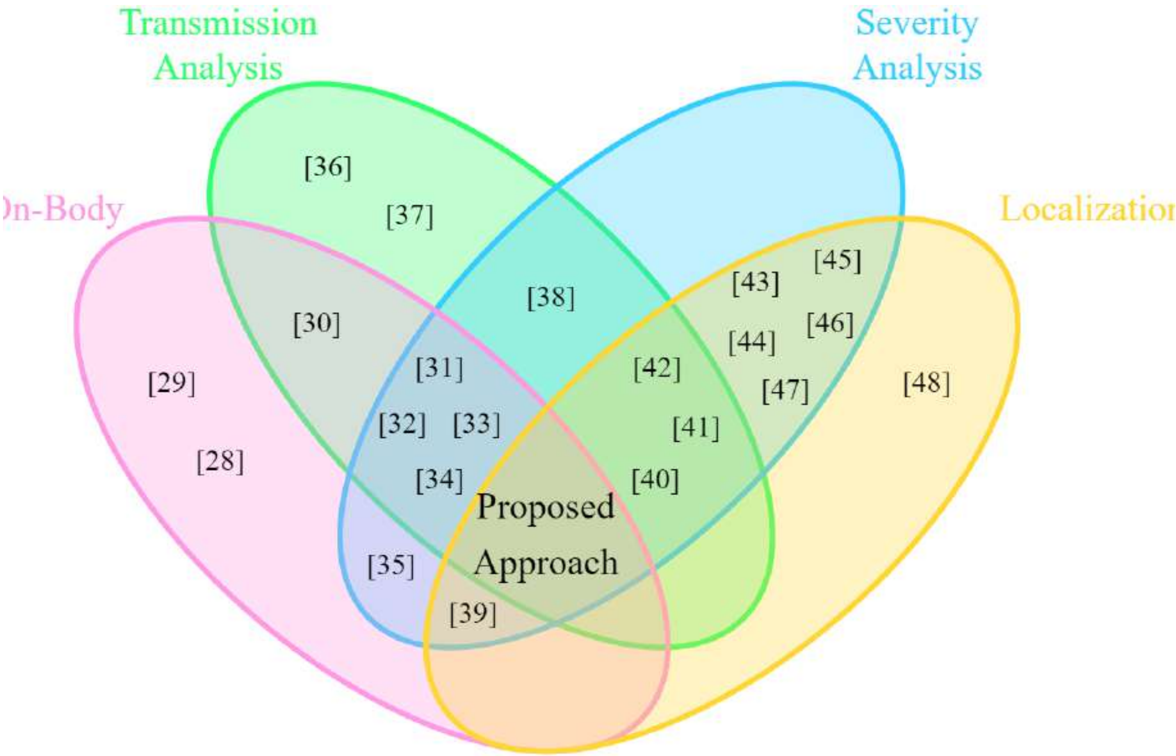

Figure 1.2. The lotus diagram for the comparison between the proposed detection method and the other works in the literature.

In this thesis, an antenna array system for PE detection is introduced. The system we propose adopts a sensing-based detection method for the application. The significance of this work lies in bridging the gap between the sensing and imaging techniques. Unlike common imaging methods that rely on bulky equipment and imaging devices, the proposed detection method can achieve localization and severity analysis by analyzing transmissions between the antennas. Also, it ensures user convenience through an on-body design.

1.3. On-Body Antennas for WBAN Applications

Antennas are excellent candidates for direct sensing due to their passive nature, eliminating the need for batteries. Therefore, on-body antennas can serve as wearable sensors in specific applications and play crucial roles in in-body, on-body, and off-body communications. As highlighted in Section 1.2.3., both the reflection and transmission performances of antennas make them suitable for body sensing. Depending on the purpose of the application, either reflection or transmission coefficients could be the indicator of the parameter to be sensed. Although utilizing the reflection coefficient is a simpler approach for monitoring the desired parameter, it is not deemed a dependable method for sensing deeper tissues within the body. As a result, the transmission coefficient between antennas is often preferred for in-body sensing. However, it's essential to note that establishing a direct mapping between the transmission coefficient and the parameter could be challenging in scenarios with poor transmission. Enhancing the transmission sensitivity is achievable through the careful design of wearable antennas. Nevertheless, it is important to consider that while the propagation into the human body should be maximized, specific absorption rate(SAR) restrictions and biocompatibility should be taken into account [22].

The literature contains a wide variety of on-body antenna designs [49–72]. These on-body antennas are intended to function for many standards, including ultra-wideband (UWB), industrial, scientific and medical(ISM) bands ($2.4-2.5$ GHz) and ($5.725-5.875$ GHz), and the medical implant communication system(MICS) band ($402-405$ MHz). A common challenge encountered in various antenna designs is ensuring user acceptability, an issue that can be successfully addressed through the utilization of flexible substrates [62–66], [68]. In literature, the discussed flexible substrates involve RF substrates with a thin profile [2] and [66], traditional wearable materials such as jean or wool fabric [63,64] or foam [62], [65], and [68]. Regrettably, in all cases, achieving miniaturization through substrate loading is not possible. This limitation stems from the low permittivity inherent of these wearable materials. Additionally, thin substrates fail to load antennas effectively due to their low filling factor. In this application, we are utilizing a novel flexible material which has high permittivity to achieve both flexibility and miniaturization simultaneously. The increment of permittivity involves the innovative practice of doping polymer substrates with high permittivity ceramic materials [73]. PDMS emerges as the most commonly used polymer, with common doping ceramics including Al_2O_3 [69], $BaTiO_3$ [73], and $SrTiO_3$ [74]. In this work, we achieved a relative permittivity value of 11.2 by doping RTV-2 silicone with graphite which has never been considered in the development of high-permittivity flexible substrates(HPFSs) before.

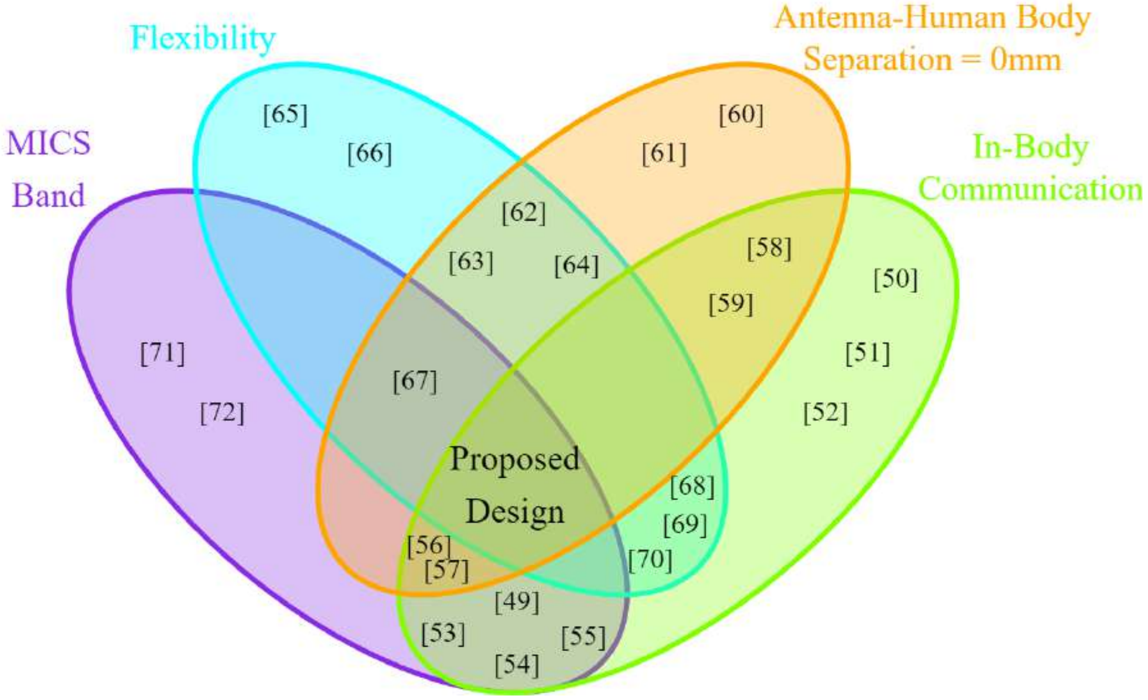

Figure 1.3. The lotus diagram for the comparison between the proposed antenna and the other related works in the literature.

The design requirements of on-body antennas vary based on their intended applications. For instance, on-body antennas used for in-body links should be optimized for efficient propagation into the human body [49–59], [68–70]. While the specific requirements vary, maintaining user acceptability remains a crucial consideration. However, in many studies within the literature, there is a tendency to prioritize performance over flexibility since in-body links are primarily utilized in medical applications rather than for consumer purposes. Among these studies, only [68], [69], and [70] employ flexible substrates. A rubber protective foam with a relative permittivity value of 1.485 is proposed as the antenna substrate [68]. However, the proposed design includes 3.94 mm of substrate height and 7.92 mm of matching layer thickness which makes it hard to utilize in wearable applications. In [69], an antenna array printed on a flexible polymer-ceramic composite comprising RTV silicon and Al_2O_3 is proposed. The antenna elements are tuned to resonate in the frequency range of $0.9 - 2.5$ GHz for head imaging. Similarly, in reference [70], another antenna array system operating at around 1 GHz printed on a custom flexible substrate for head imaging is presented. In addition to the array sensors, both designs integrate a flexible matching layer between the head and the antennas to enhance impedance matching. Distinctly, our design proposes an antenna on a flexible HPFS at 403 MHz MICS band and it is placed directly on the human body without any matching layer. This design choice leads to a higher propagation into the human body compared to designs with matching layers since there is no additional layer increasing the propagation distance.

In this thesis, we present an on-body flexible antenna designed for PE detection operating within the MICS band. Figure 1.3 provides a comparative analysis between the proposed antenna and closely related designs. The structure we propose is a coplanar waveguide-fed loop antenna. The distinctive feature of this work lies in the application of a novel high-permittivity substrate, allowing us to achieve a reasonably sized flexible on-body antenna, even at an operating frequency of 403 MHz. The high permittivity value of the fabricated substrate serves for miniaturization, resulting in a compact antenna size as well as satisfying the user's convenience with high flexibility.

2. ON-BODY FLEXIBLE ANTENNA DESIGN AND FABRICATION

In this chapter, the required background for understanding the proposed antenna and high-permittivity substrate is provided, along with a comprehensive performance analysis. The reason behind the antenna selection is explained in Section 2.1, followed by Section 2.2 which covers the fundamentals of the chosen antenna. Section 2.3 presents the novel HPFS and its fabrication procedure. The selection of the antenna structure considering the trade-off between user acceptance and antenna performance is formulated in Section 2.4. Subsequently, Section 2.5 introduces the feeding mechanism, marking the final phase of the antenna design. Following these sections, optimization and on-body performance of the proposed antenna are analyzed in Section 2.6. Finally, the fabrication process of the antenna is explained in detail in Section 2.7.

2.1. Antenna Selection

In this work, the detection of PE is aimed to be achieved by in-body sensing with on-body wearable antennas. Considering the monitoring changes in the dielectric properties of the lungs, which are deeper tissues compared to muscles and bones, the transmission coefficient analysis between the antennas on the anterior and posterior torso is a reliable method. Therefore, the in-body propagation should be maximized for effective detection and monitoring.

Initially, the study of radiation into a lossy medium and its associated mathematical expressions were explored in the context of underwater communication [75]. This work also proves that the fundamental radiation characteristics of an antenna are not valid when the antenna radiates into a lossy medium. The radiation characteristics in lossy media are later adapted to the human body in medical applications. For instance, radiation into lossy media is considered for implant antennas, where the lossy medium consists of not a single conductive layer but multiple complex biological tissues [76].

Hence, the in-body radiation efficiency of the antenna is affected by three main factors which are near-field coupling, attenuation through the body, and reflection at the tissue boundaries [76]. Considering these factors, the total radiated power reaching free space from an implant antenna is given in [77] as

$$P_{\text{total radiated power}} = P_{\text{entering the body}} \cdot e_{\text{near-field}} \cdot e_{\text{propagation}} \cdot e_{\text{reflections}} \tag{2.1}$$

where P and e are power and loss, respectively. It should be noted that loss values given in Equation (2.1) are expected to vary among individuals due to differences in body tissue compositions. Therefore, approximate values of these losses are simulated within simple body phantoms [78] and tried to be calculated hybrid combining T-matrix method [79]. By using these loss mechanisms and values, the fact that magnetic-like modes experience less near-field losses due to the non-magnetic nature of human tissues is deduced in [80]. This observation is further confirmed by comparing a simple dipole and a loop antenna in another study [81]. This work shows that a magnetic source outperforms an electrical source of the same order in the near-field frequency range, but they have similar far-field performances. That's why a loop antenna which is a magnetic antenna is a suitable choice for this thesis.

2.2. Fundamentals of Loop Antennas

Loop antennas are a cost-effective and versatile type of antenna. They might be in various forms such as rectangles, squares, triangles, ellipses, circles, and many other configurations. Their versatility arises from the fabrication choices, which include 3D-shaped conductors or conductor sheets printed on a substrate as shown in Figure 2.1. The classification of loop antennas is conveniently divided into two categories, electrically small and electrically large. Electrically small loop antennas have an overall length(circumference) of less than one-tenth of a wavelength($C < \lambda/10$), whereas the circumference of electrically large loops is about a free-space wavelength($C \sim \lambda$) [82].

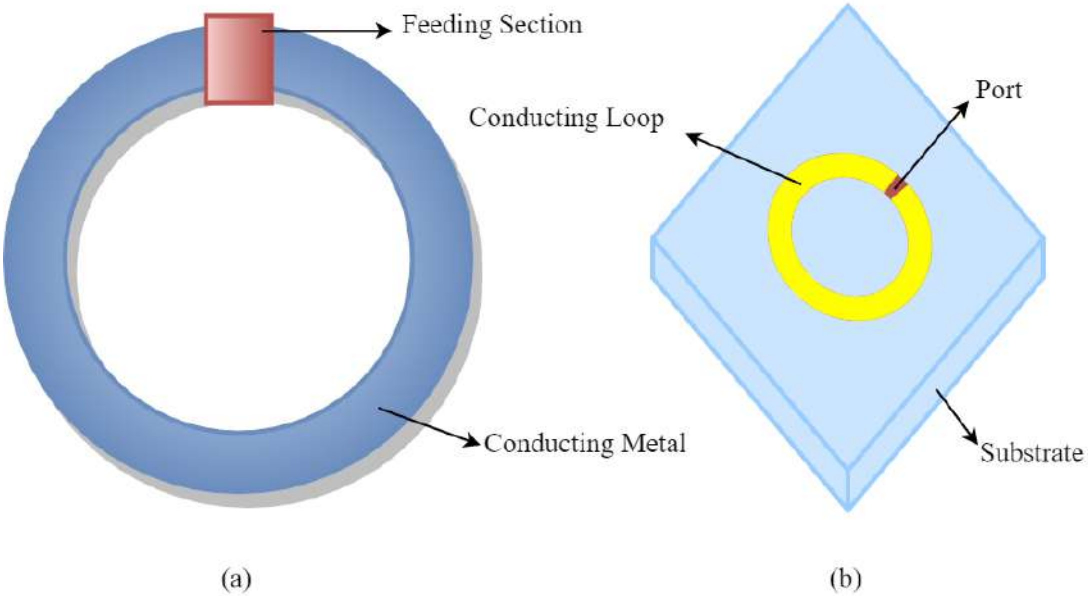

Figure 2.1. (a) 3D circular-shaped wire loop. (b) 2D conducting sheet printed on a substrate.

2.2.1. Electrically Small Loops

As mentioned above, electrically small loops have a circumference of less than one-tenth of the wavelength, leading to a uniform axial current distribution on the loop [83]. The uniform current distribution on a wire allows to application of the duality principle. The loop can be replaced with a magnetic dipole, simplifying the calculation of electric field(E_r, E_θ, E_ϕ) and magnetic field(H_r, H_θ, H_ϕ) components in spherical coordinates which are extensively explained in [82]. The resulting expressions are summarized as follows

$$H_r = j\frac{ka^2 I_0 \cos\theta}{2r^2}[1+\frac{1}{jkr}]e^{-jkr}, \tag{2.2}$$

$$H_\theta = -\frac{(ka)^2 I_0 \sin\theta}{4r}[1+\frac{1}{jkr}-\frac{1}{(kr)^2}]e^{-jkr}, \tag{2.3}$$

$$H_\phi = 0, \tag{2.4}$$

$$E_r = 0, \tag{2.5}$$

$$E_\theta = 0, \tag{2.6}$$

$$E_\phi \quad = \quad \eta\frac{(ka)^2 I_0 \sin\theta}{4r}[1+\frac{1}{jkr}]e^{-jkr}. \tag{2.7}$$

Here, k is the wavenumber, I_0 is the constant current, a is the diameter, r is the radial distance, θ is the angle between the z-axis and r vector, ϕ is the azimuthal angle and η is the wave impedance.

Depending on the field components given above, the power density and the radiation resistance could be derived. The power density can be calculated by

$$\mathbf{W} = \frac{1}{2}(\mathbf{E} \times \mathbf{H}^*) \tag{2.8}$$

where $\mathbf{W}$, $\mathbf{E}$, and $\mathbf{H}^*$ are power density components, electric field components, and complex conjugates of magnetic field components. When Equation (2.8) is integrated over a closed sphere, only the radial component of power density(W_r) contributes to the complex power P_r shown below

$$P_r = \oiint_S \mathbf{W} \cdot d\mathbf{s}. \tag{2.9}$$

The radiated power of a small loop antenna is the real part of the complex power P_r which can be reduced from the integral as

$$P_{rad} = \eta(\frac{\pi}{12})(ka)^4 |I_0|^2. \tag{2.10}$$

By using P_{rad} in Equation (2.10), the radiation resistance(R_r) can be calculated via

$$P_{rad} = \frac{I_0^2}{2}R_r. \tag{2.11}$$

Finally, the radiation resistance becomes

$$R_r = \eta(\frac{\pi}{6})(ka)^4 = \eta\frac{2\pi}{3}(\frac{kS}{\lambda}) = 20\pi^2(\frac{C}{\lambda})^4 \simeq 31.171(\frac{S^2}{\lambda^4}) \tag{2.12}$$

where $S = \pi a^2$ is the area and $C = 2\pi a$ is the circumference. The Equation (2.12) is for a single-turn loop. If the loop antenna has multiple N turns, the new radiation resistance becomes $R_r N^2$. So, it can be deduced that the radiation resistance of a small loop can be enhanced by increasing the number of turns. It should be noted that electrically small loops have a circumference of less than one-tenth of a wavelength, which causes very low radiation resistance according to Equation (2.12). Therefore, they are poor radiators and not used as transmitters in radio communication systems

[82]. However, their radiation pattern is doughnut-shaped which can be deduced from electric field components given in Equations (2.5), (2.6), and (2.7). Hence, they are commonly used as receiving antennas [83].

2.2.2. Electrically Large Loops

Electrically large loops have a current varying in both amplitude and phase depending on the position on the loop as shown in Figure 2.2. The current is continuous around the loop and starts with a maximum at the feeding point and at the center of the side parallel to the x-axis. That's why the impedance and the radiation pattern change with the loop size [84].

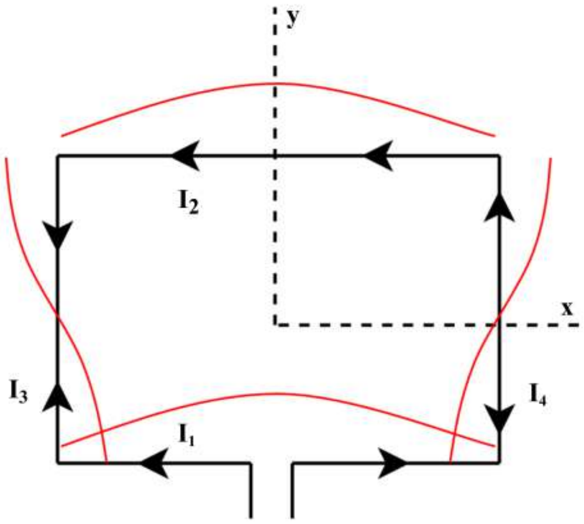

Figure 2.2. The one-wavelength square loop antenna. Each side is of length $\lambda/4$. The red curve represents the sinusoidal current distribution of the loop.

The radiation properties of large loop antennas can be derived through the calculation of vector potential as below [82]

$$A_\phi = \frac{a\mu I_0}{4\pi}\int_0^{2\pi}\cos\phi'\frac{e^{-jk\sqrt{r^2+a^2-2ar\sin\theta\cos\phi'}}}{\sqrt{r^2+a^2-2arsin\phi'}}d\phi' \qquad (2.13)$$

where A_ϕ is the vector potential of the azimuthal angle component. The simplification of the integral in Equation (2.13) is explained in both [82] and [84] and the final form of the vector potential becomes

$$A_\phi \simeq j\frac{a\mu I_0 e^{-jkr}}{2r} J_1(ka\sin\theta). \tag{2.14}$$

Here, $J_1(z)$ refers to the Bessel function of the first kind of order 1. Finally, **E** and **H** fields associated with the vector potential given in Equation (2.14) are derived as

$$\begin{aligned}
H_r &= 0, & (2.15)\\
H_\phi &= 0, & (2.16)\\
H_\theta &= -\frac{E_\phi}{\eta} = \frac{akI_0 e^{-jkr}}{2r} J_1(ka\sin\theta), & (2.17)\\
E_r &= 0, & (2.18)\\
E_\theta &= 0, & (2.19)\\
E_\phi &= \frac{ak\eta I_0 e^{-jkr}}{2r} J_1(ka\sin\theta). & (2.20)
\end{aligned}$$

Analyzing the field components above, it is observed that the radiation characteristics of electrically large loop antennas differ from electrically small loop antennas. Maximum radiation occurs perpendicular to the plane of the loop. Within the loop plane, a null appears in the direction parallel to the side with the feeding point and there is a peak lobe perpendicular to the null direction [84]. These findings of electrically large loop antennas contrast with electrically small loop antennas which exhibit an almost omnidirectional doughnut-shaped pattern. For clarity, Figure 2.3 which illustrates the 2D radiation patterns of loop antennas based on their circumference is given [85].

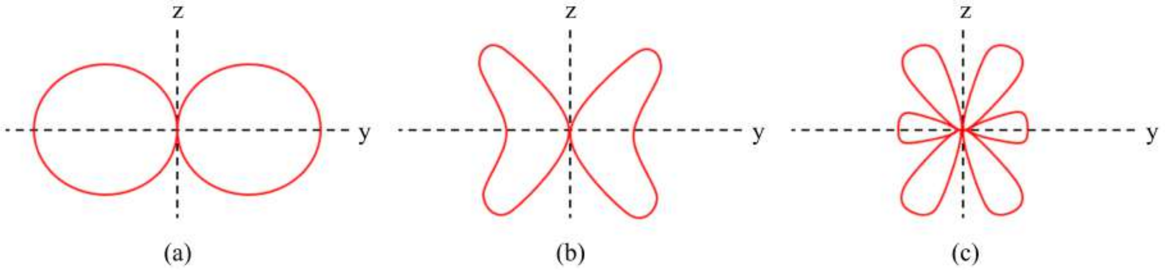

Figure 2.3. 2D radiation patterns of loop antennas with different circumferences: (a) $C = 0.1\lambda$ (b) $C = \lambda$ (c) $C = 1.5\lambda$

Furthermore, the radiation resistance and the radiated power can be calculated by the power density which is shown in Equation (2.8). The radiated power for electrically large loops becomes as

$$P_{rad} = \iint_S \mathbf{W}_{av} \cdot d\mathbf{s} = \frac{\pi(a\omega\mu)^2 |I_0|^2}{4\eta} \int_0^\pi J_1^2(ka\sin\theta)\sin\theta d\theta \tag{2.21}$$

where ω is the angular frequency. For electrically large loop antennas, the integration $\int_0^\pi J_1^2(ka\sin\theta)\sin\theta d\theta$ can be approximated to $(1/ka)\int_0^{2ka} J_2(x)dx \simeq (1/ka)$. So, the radiated power can be expressed as

$$P_{rad} = \frac{\pi(a\omega\mu)^2 |I_0|^2}{4\eta(ka)}. \tag{2.22}$$

Consequently, the radiation resistance(R_r) becomes

$$R_r = \frac{2P_{rad}}{|I_0|^2} = \frac{2\pi(a\omega\mu)^2}{4\eta(ka)} = \eta(\frac{\pi}{2})ka = 60\pi^2(ka) = 60\pi^2\frac{C}{\lambda}. \tag{2.23}$$

where the circumference $C = 2\pi a$ and $\eta \simeq 120\pi$. By comparing Equations (2.12) and (2.23), it can be deduced that large loop antennas have a higher radiation resistance compared to small loop antennas. However, radiation resistance should be revisited for on-body applications. Due to the multiplication with the effective permittivity(ϵ_{eff}), R_r value for both small and large loops increases by ϵ_{eff}^2 and $\sqrt{\epsilon_{eff}}$, respectively. Even though the human body loading increases the radiation resistance of small loops more than large loops, the radiation resistance of large loops is still hundreds of times greater because of the circumference-to-wavelength ratio. This makes them suitable for use as transmitters since their impedance can be matched to that of the human body. Large loop antennas also have directional radiation characteristics, making them ideal for use in directional arrays like helical antennas, Yagi-Uda arrays, quad arrays, and more [82]. These features make large loop antennas excellent candidates for direction-finding systems [84]. In this work, it is anticipated that the antennas placed on the anterior torso are employed for transmitting and the ones on the posterior torso are used as receivers. Consequently, a large loop antenna is designed for transmitting and receiving.

2.3. High-Permittivity Flexible Substrate(HPFS)

In this section, the substrate of the proposed loop antenna is introduced. Before giving the details about the HPFS, it is significant to highlight the concept of dielectric loading. This understanding will provide clarity on why fabricating a substrate with high permittivity is necessary.

2.3.1. Dielectric Loading of Antennas

When an antenna is fabricated on a dielectric material, the electric and magnetic field components of the antenna are affected by the material's permittivity and conductivity in its near-field. In Figure 2.1(b), a loop is printed on a dielectric material that functions as a dielectric load. When radiating elements of antennas are placed on dielectric loads, these materials are referred to as antenna substrates. The electromagnetic wave radiated by the antenna is not only propagating in the air but also in the dielectric substrate, which changes the electrical length of the antenna dimensions. Therefore, the circumference of a loop antenna can not be calculated by using the free space wavelength(λ_0). Instead, the guided wavelength should be considered, which is given by

$$\lambda_g = \frac{\lambda_0}{\sqrt{\epsilon_{eff}}}. \tag{2.24}$$

Here, λ_0 represents the free space wavelength, λ_g is the guided wavelength and ϵ_{eff} stands for the effective permittivity. When electromagnetic waves are contained in multiple media, their properties change accordingly, depending on the medium they travel [86]. As a result, the formulations typically used in free space can not be applied directly. Instead, overall permittivity and permeability should be analyzed for the wave's behaviour. Briefly, the effective permittivity represents the relative permittivity of a composite medium that includes air and any other dielectric media present. It can be calculated by

$$\epsilon_{eff} = \epsilon_{r,medium} \cdot ff + \epsilon_{r,air} \cdot (1 - ff) \tag{2.25}$$

where ff is the filling factor which measures the percentage of the electric fields penetrating through the substrate. It should be noted that Equation (2.25) is applicable when the radiating element is covered by only two media. For setups involving multiple complex media, the calculation becomes more challenging. Additionally, the filling factor, ff, is expected to be different for each type of antenna and it can be approximated with multiple simulations.

Consequently, it can be deduced that the size of an antenna can be reduced by using dielectric loading. As indicated in Equation (2.24), if the effective permittivity value is high, the guided wavelength will be small, which ultimately leads to a smaller antenna size. The objective of this project is to design an on-body loop antenna that can detect PE while ensuring the flexibility of the antenna for user acceptance. However, commercial flexible materials often lack sufficiently high relative permittivity values to achieve the desired miniaturization, as exemplified in the introduction. Therefore, a new high-permittivity flexible substrate is necessary for this project.

2.3.2. Fabrication of HPFS

The constitute materials of novel HPFS are composed of room-temperature-vulcanizing-2(RTV-2) silicone mixed with graphite powder. RTV-2 silicone is chosen as the main material for its flexibility, while graphite powder is added to adjust the dielectric properties of the silicone. The proportions of these components vary depending on the desired permittivity value during fabrication. The procedure to be followed for the fabrication of HPFS for the intended permittivity value of 11 is given step by step below:

(i) The RTV-2 silicone base and graphite powder are mixed in a mass ratio of 15 : 6 (RTV-2 silicone base : Graphite powder).
(ii) The mixture is stirred until it achieves a uniform consistency.
(iii) The curing agent of the silicone is added to the mixture in a mass ratio of 15 : 0.2 (RTV-2 silicone base : Curing agent)

(iv) The mixture is stirred for at least 4 minutes to ensure proper blending.

(v) The mixture is then poured into a pre-prepared mould to give it the desired shape.

(vi) The mould filled with the mixture is placed in a vacuum oven for an additional 4 minutes to make sure there is no air bubble left in the mixture.

(vii) The mixture is left at room temperature until it is completely cured.

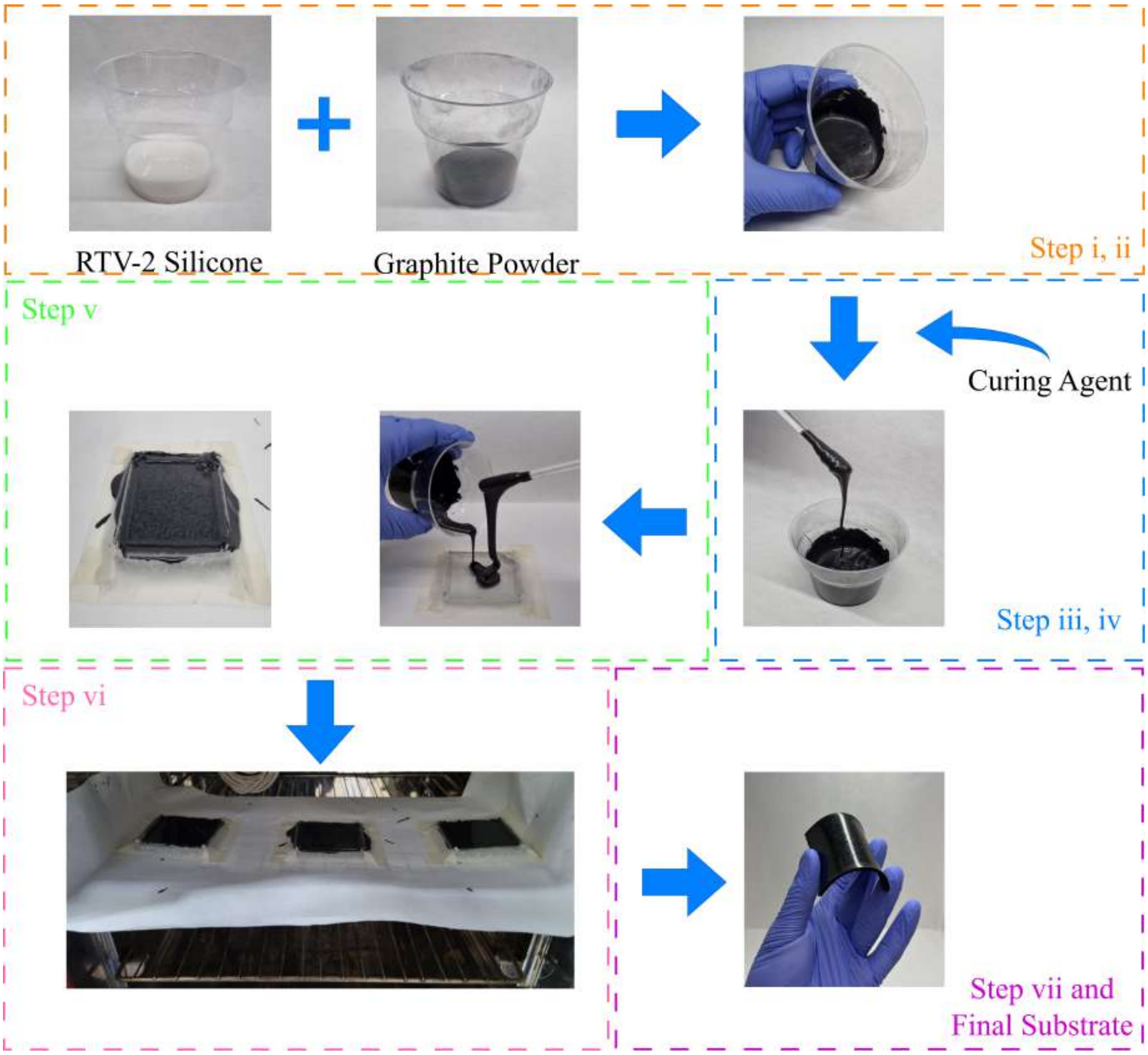

Figure 2.4. Fabrication process of HPFS.

The fabrication process given above is illustrated in Figure 2.4. Following the curing step, the relative permittivity and the loss tangent($\tan\delta$) of the fabricated substrate are measured at room temperature by using Speag's DAKS 3.5 dielectric measurement kit. The measurement is shown in Figure 2.5(a).

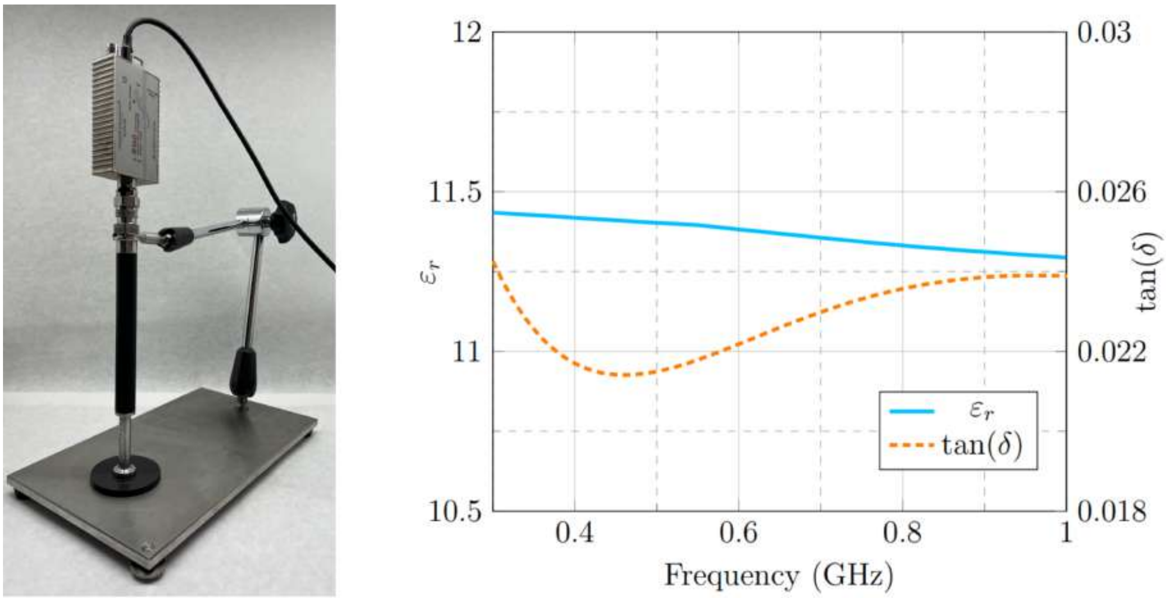

(a)

(b)

Figure 2.5. (a) Measurement of dielectric properties with Speag's DAK 3.5 probe. (b) Relative permittivity and loss tangent values versus frequency for the fabricated HPFS.

The measurement results are depicted in Figure 2.5(b). The proposed HPFS has relative permittivity and loss tangent values of 11.44 and 0.021 at 405 MHz, respectively. Notably, it can be realized that fabricated HPFS has a similar loss tangent value to FR-4 while maintaining the desired flexibility for wearable applications. It is important to mention that increasing the amount of graphite powder in the mixture can lead to higher relative permittivity, but it also increases the loss tangent. Therefore, the recipe for HPFS could be modified depending on specific requirements. For this work, the recipe mentioned above was chosen due to its suitability for in-body propagation analysis.

2.4. Selection of Antenna Structure

The trade-off between user acceptance and antenna performance has been a common issue for on-body antenna applications in the literature [50]. For in-body propagation purposes, this trade-off can be defined as the comparison between electrically large flexible antennas with relatively low radiation performance and electrically small rigid antennas with better radiation performance.

In this work, fabricated HPFS satisfies the flexibility property. However, the trade-off between size and performance remains when miniaturization is considered. Further miniaturization of the proposed loop antenna could be achieved by various methods, including altering the dielectric properties of the HPFS, adjusting substrate thickness, sandwiching the radiating loop with HPFS layers, and a conventional method, meandering. Therefore, to determine the optimal antenna structure, simulations of different loop antennas are conducted.

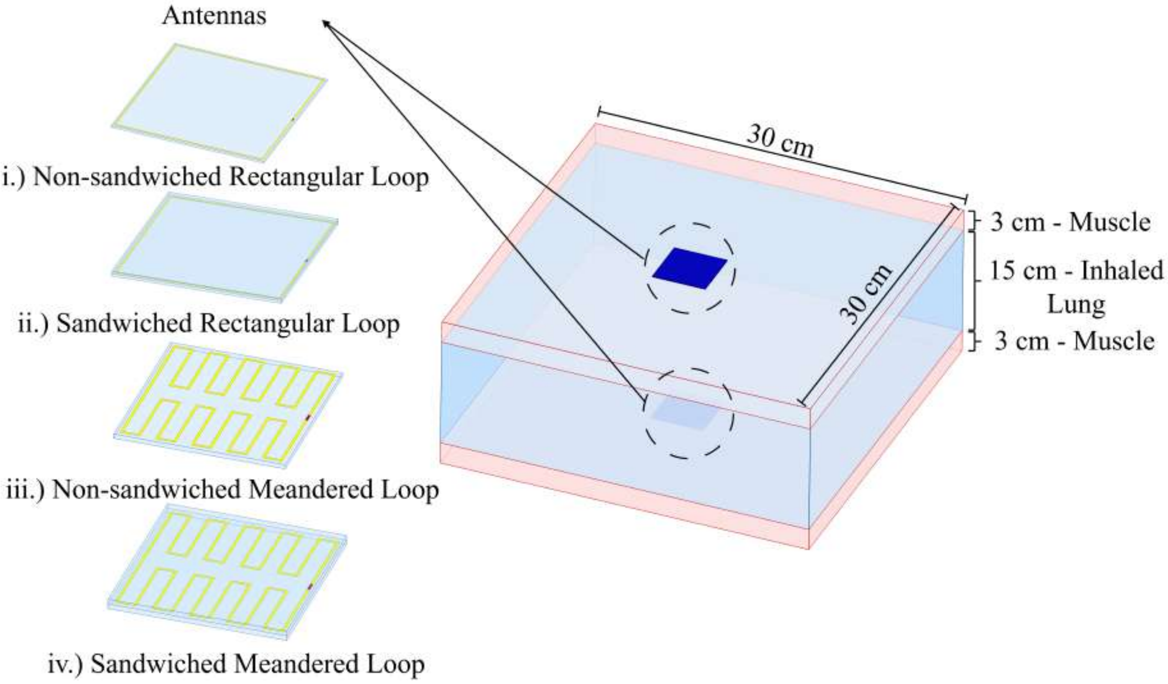

Figure 2.6. The simulation setup for antenna selection: Simplified torso phantom and different types of antennas.

The simulation setup for different antenna types is shown in Figure 2.6. Two antennas are placed on the simplified anterior and posterior torso phantom and the performance analysis is completed in a back-to-back transmission scenario. Besides meandering and sandwiching variations, the dielectric properties of HPFS layers of antennas are also altered in the simulations. Permittivity values of 5, 7, and 11 are employed for all structures given in Figure 2.6.

Table 2.1 shows the antennas designed for this work. After the analysis of a standard rectangular loop antenna, miniaturization methods are employed. Introducing a superstrate is anticipated to decrease the size of antennas due to the increment in the effective permittivity. However, it is also evident that the addition of a superstrate does not reduce the size of the antenna as well as 2D meandering does. Even though the miniaturization achieved through 2D meandering is better than the one achieved with sandwiching, the transmission power deteriorates due to the reduced aperture area and efficiency [87].

In order to compare the antenna structures given in Table 2.1, we propose a figure of merit combining the transferred power and the volume of the antenna as shown below

$$\kappa = \frac{P^{\psi}}{V^{(1-\psi)}} \tag{2.26}$$

where P is the accepted power in W, V is the total volume of the antenna in mm^3, ψ is the significance order between $[0, 1]$ and κ is the power per unit volume expanded with a constant significance order. The proposed relation in Equation (2.26) serves as a figure of merit. The significance order, ψ, is determined by the user depending on the application or other constraints. If there is no lower bound for the transmitted power, one may choose ψ to be 0 so that κ becomes maximum for the antenna with the minimum volume. On the other hand, if one cares only about the transmitted power level and has no size constraints, they can choose ψ to be 1, which makes κ maximum for the antenna with the largest power transmission.

Table 2.1. Individual dimensions and the simulation results of transmission coefficient for loop antennas differing in miniaturization, sandwiching, and substrate.

Antenna Type	**X-Y Size(mm × mm)**	**Profile(mm)**	**$\lvert S_{21}\rvert$(dB) at 403 MHz**	**Power(μW)**
Rectangular Loop				
Permittivity 5	82 × 82	1	-42.51	56.1
Permittivity 7	72 × 72	1	-43.89	45.8
Permittivity 11	62 × 62	1	-49.34	11.6
Sandwiched Rectangular Loop				
Permittivity 5	72 × 72	2	-43.17	48.1
Permittivity 7	64 × 64	2	-44.33	36.9
Permittivity 11	54 × 54	2	-50.01	10
2D Meandered Loop				
Permittivity 5	40 × 40	1	-54.29	3.7
Permittivity 7	36 × 36	1	-56	2.5
Permittivity 11	34 × 34	1	-58.02	1.5
Sandwiched & 2D Meandered Loop				
Permittivity 5	37 × 37	2	-55.75	2.6
Permittivity 7	34 × 34	2	-57.51	1.7
Permittivity 11	32 × 32	2	-58.92	1.3

In this work, ψ was chosen to be 0.3. This value provides the authors with not only a sufficient transmitted power level that can be observed on a Vector Network Analyzer (VNA) but also an acceptable size and volume for a flexible antenna application with satisfying user acceptance. Therefore, the antenna utilized for this work, corresponding to the chosen value of ψ, is a sandwiched rectangular loop antenna with the relative permittivity value of 11 for the HPFS.

2.5. Coplanar Waveguide Feeding

2.5.1. Fundamentals of Balanced and Unbalanced Structures

Most of the wire antennas have a balanced nature, meaning that currents flowing through the wires are symmetrical. In a balanced setup depicted in Figure 2.6(a), the currents flowing through the transmission lines have equal magnitude but flow in opposite directions, minimizing radiation from the transmission line. However, in unbalanced scenarios illustrated in Figure 2.7(b), there's a discrepancy in current magnitudes between the transmission lines. This leads to a net current flow in one line, causing unintended radiation which is not in the desired direction or of the desired polarization [84]. Therefore, it is clear that a balanced operation is desirable.

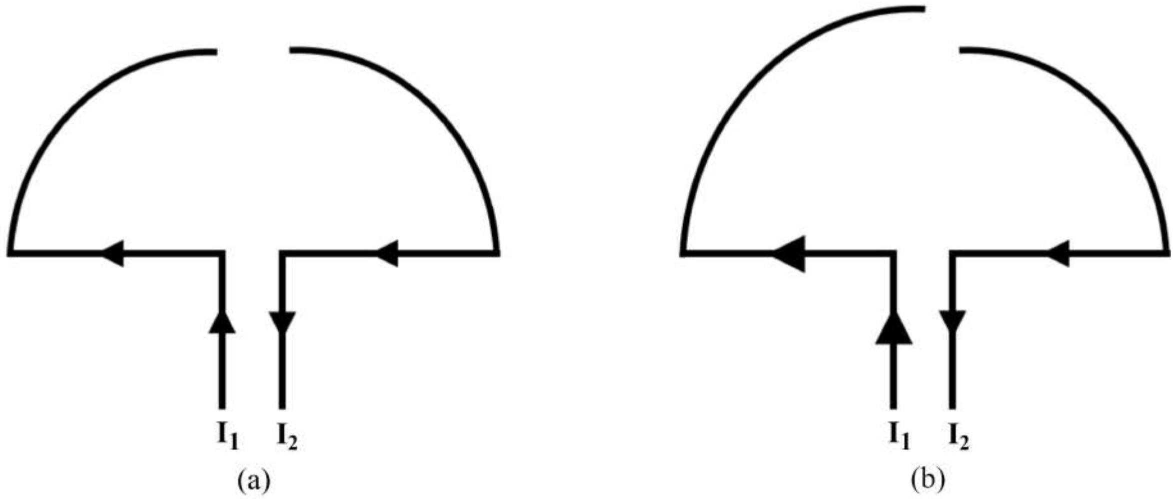

Figure 2.7. Balanced and unbalanced operations of a wire antenna: (a) Balanced currents, $I_1 = I_2$ (b) Unbalanced currents, $I_1 > I_2$.

Even though balanced operations are preferred, connecting to a coaxial cable, an unbalanced transmission line, is necessary for practical scenarios where structures are fabricated and their S-parameters are measured with a VNA. When a current flowing through a coaxial line reaches a symmetrical antenna, an additional current may flow back on the outside of the outer conductor as shown in Figure 2.8. This extra current, labelled as I_3, will lead to undesired radiation. To address this issue, a balun, abbreviation of balance to unbalance transformer, is employed in literature [88]. The purpose of the balun is to convert the balanced input impedance of the antenna to the unbalanced impedance of the coaxial line, ensuring that there is no net current on the outer conductor [84]. There are lots of balun types proposed in the literature such as folded baluns, bazooka baluns, half-wavelength baluns, ferrite core baluns, split coax baluns and so on [88].

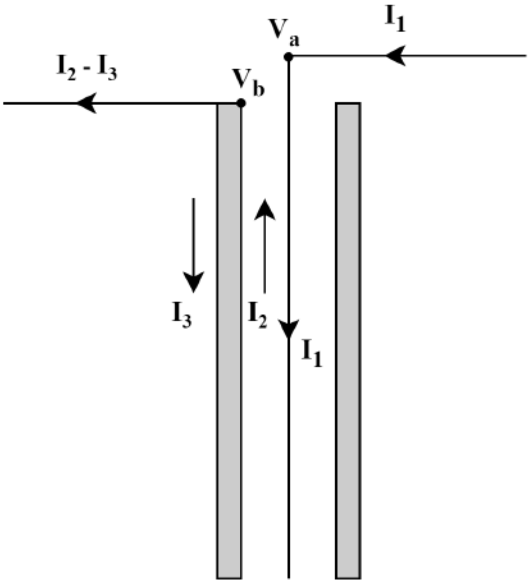

Figure 2.8. A coaxial transmission line feeding a balanced wire antenna.

In addition to baluns, antennas can utilize different feeding mechanisms to convert a balanced structure into an unbalanced one. One such mechanism is coplanar waveguide(CPW) feeding which employs two ground planes and a conducting strip in the middle of them. In a CPW, electromagnetic waves are mostly concentrated in the dielectric, allowing for optimization to minimize dispersion losses. Moreover, CPW has a single-sided nature, meaning that the ground planes do not require vias to a plane on the other side of the substrate. Therefore, they are excellent members for surface-mounted applications [89].

2.5.2. Design Procedure of Coplanar Waveguide(CPW)

CPW is a common type of planar transmission line fabricated on a printed circuit board [90]. Its typical structure is depicted in Figure 2.9. As mentioned above, CPW configuration offers advantages due to its single-sided design and property of reducing radiation losses [91], making it suitable for feeding the proposed on-body antenna.

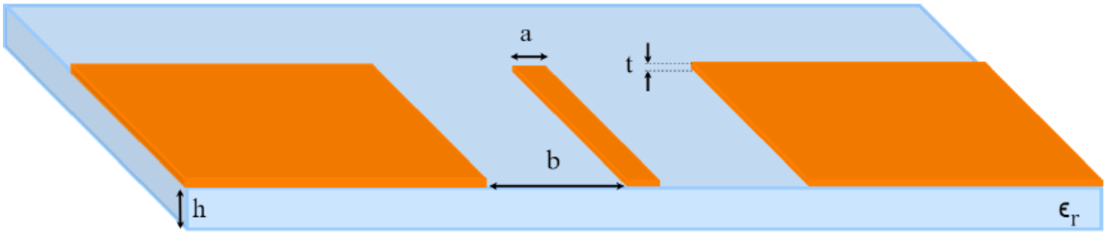

Figure 2.9. Coplanar waveguide structure and parameters of its dimensions and substrate.

The design parameters given in Figure 2.9 are trace width(a), ground spacing(b), conductor thickness(t), substrate height(h), and relative permittivity(ϵ_r) of the substrate. The design equations for designing a coplanar waveguide are given below

$$Z_0 = \frac{30\pi}{\sqrt{\epsilon_{eff,t}}} \frac{K(k'_t)}{K(k_t)}. \tag{2.27}$$

Here, Z_0 is the characteristic impedance, $K(k'_t)$ and $K(k_t)$ mean the modulus of the complete elliptic integrals. $\epsilon_{eff,t}$ can be expressed in terms of ϵ_{eff} and ϵ_r as [89]

$$\epsilon_{eff,t} = \epsilon_{eff} - \frac{\epsilon_{eff} - 1}{(b/0.7t)(K(k)/K(k')) + 1}, \tag{2.28}$$

$$\epsilon_{eff} = 1 + \frac{\epsilon_r - 1}{2} \frac{K(k')K(k_1)}{K(k)K(k'_1)} \tag{2.29}$$

where $K(k)$, $K(k')$, $K(k_1)$, $K(k'_1)$ stand for the modulus of complete elliptic integrals of k, k', k_1, and k'_1 parameters. These parameters can be calculated by

$$\begin{aligned}
k &= \frac{a}{2b+a}, \tag{2.30}\\
k_t &= \frac{a_t}{b_t}, \tag{2.31}\\
k' &= \sqrt{1-k^2}, \tag{2.32}\\
k'_t &= \sqrt{1-k^2}, \tag{2.33}\\
k_1 &= \frac{\sinh(\pi a_t/4h)}{\sinh(\pi b_t/4h)}, \tag{2.34}\\
k'_1 &= \sqrt{1-k_1^2}, \tag{2.35}\\
a_t &= a + \frac{1.25t}{\pi}[1+\ln(\frac{4\pi a}{t})], \tag{2.36}\\
b_t &= 2b + a - \frac{1.25t}{\pi}[1+\ln(\frac{4\pi a}{t})] \tag{2.37}
\end{aligned}$$

where a_t and b_t are dimension functions of t for a and b, respectively. These equations are adjusted to account for the thickness which is significant for accurate results [89]. However, these equations are relevant for a conventional CPW. In this work, the proposed antenna setup involves sandwiching, which requires a different calculation approach for the CPW. The analysis for sandwiched CPWs is detailed in [92] and this approach is adopted for designing the feeding mechanism of our proposed antenna.

Figure 2.10 illustrates the structure of sandwiched CPW. As seen in the figure, substrate thicknesses are designated as h_1 and h_2. The corresponding relative permittivities are assumed to be ϵ_1 and ϵ_2. Two metal planes acting as a shield are placed at distances of h_3 and h_4 from the CPW conductors.

In the provided analysis, the CPW conductors and the dielectric substrates are assumed to have perfect conductivity and relative permittivity, respectively. So, the structure is regarded as lossless. Additionally, the dielectric substrates are considered to be isotropic.

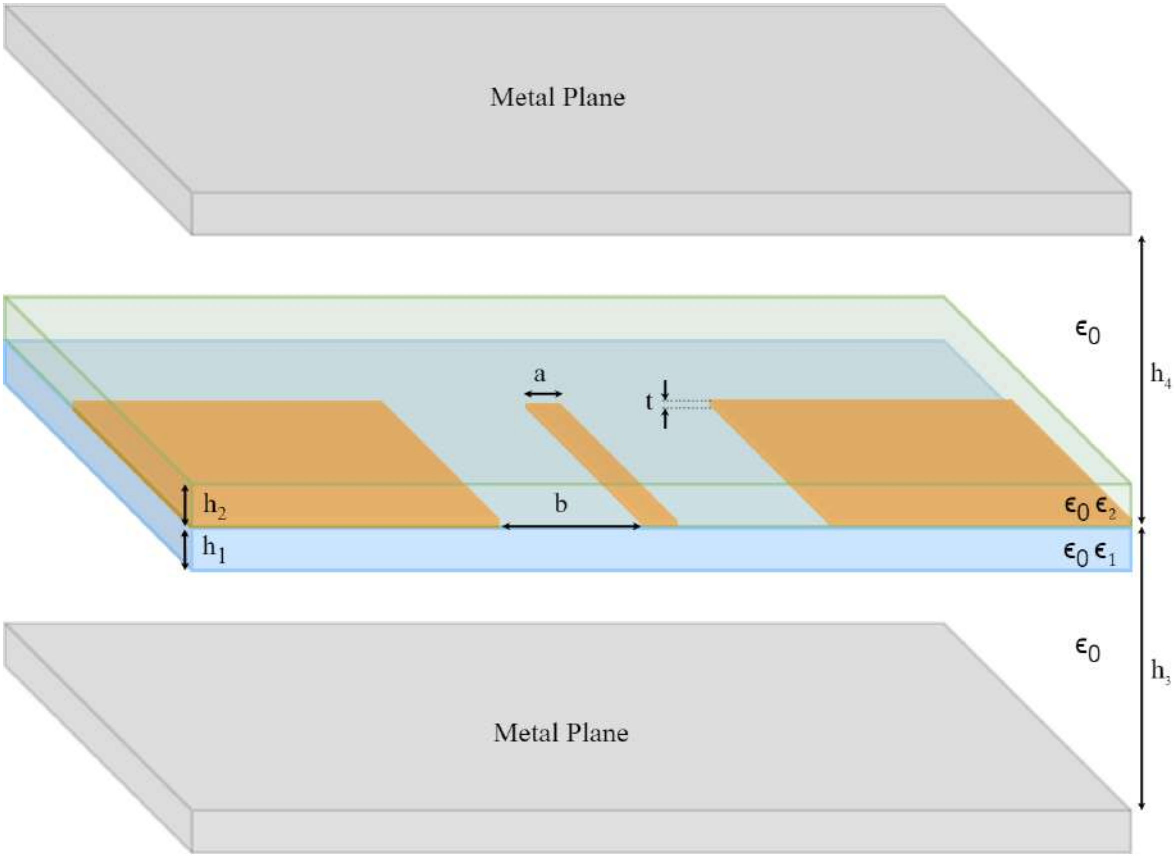

Figure 2.10. The sandwiched CPW structure between two dielectric substrates.

For the calculation of ϵ_{eff} and Z_0, conformal mapping techniques are employed. The conductor thickness(t) is assumed to be zero and magnetic walls are present along all the dielectric boundaries, including CPW slots [92]. Then, the CPW is divided into several regions and the electric field is assumed to exist only in these regions.

By using the assumptions above, C_{CPW} can be calculated as the summation of partial capacitances of these regions depicted in Figure 2.11 as below

$$C_{CPW} = C_1 + C_2 + C_{air}. \tag{2.38}$$

Here, C_1 and C_2 represent the partial capacitances of the CPW with only upper and lower dielectrics, respectively. Additionally, C_{air} denotes the partial capacitance of the CPW in the absence of all dielectrics.

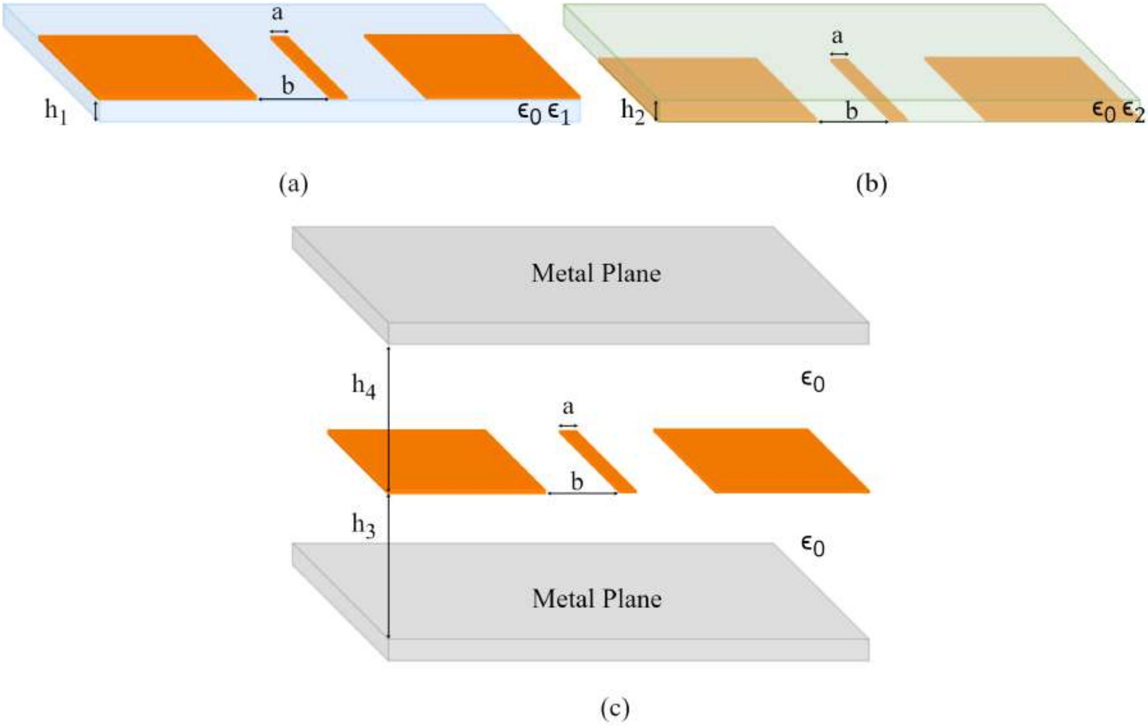

Figure 2.11. Configurations of partial capacitances for a sandwiched CPW: (a) C_1 (b) C_2 (c) C_{air}.

The partial capacitance C_1 is given by

$$C_1 = 2\epsilon_0(\epsilon_1 - 1)\frac{K(k_1)}{K(k_1')} \tag{2.39}$$

where k_1 and k_1' are calculated as follows

$$k_1 = \frac{\sinh(\pi a/4h_1)}{\sinh[\pi(a+2b)/4h_1]}, \tag{2.40}$$

$$k_1' = \sqrt{1-k_1^2}. \tag{2.41}$$

The partial capacitance C_2 is given by:

$$C_2 = 2\epsilon_0(\epsilon_2 - 1)\frac{K(k_2)}{K(k_2')} \tag{2.42}$$

where k_2 and k_2' are calculated as follows

$$k_2 = \frac{\sinh(\pi a/4h_2)}{\sinh[\pi(a+2b)/4h_2]}, \tag{2.43}$$

$$k_2' = \sqrt{1-k_2^2}. \tag{2.44}$$

The partial capacitance C_{air} is given by:

$$C_{air} = 2\epsilon_0 \frac{K(k_3)}{K(k_3')} + 2\epsilon_0 \frac{K(k_4)}{K(k_4')} \tag{2.45}$$

where k_3, k_4, k_3', and k_4' are calculated as follows

$$\begin{aligned} k_3 &= \frac{\tanh(\pi a/4h_3)}{\tanh[\pi(a+2b)/4h_3]}, & (2.46)\\ k_4 &= \frac{\tanh(\pi a/4h_4)}{\tanh[\pi(a+2b)/4h_4]}, & (2.47)\\ k_3' &= \sqrt{1-k_3^2}, & (2.48)\\ k_4' &= \sqrt{1-k_4^2}. & (2.49) \end{aligned}$$

Finally, C_{CPW} can be derived as

$$C_{CPW} = 2\epsilon_0(\epsilon_1 - 1)\frac{K(k_1)}{K(k_1')} + 2\epsilon_0(\epsilon_2 - 1)\frac{K(k_2)}{K(k_2')} + 2\epsilon_0 \frac{K(k_3)}{K(k_3')} + 2\epsilon_0 \frac{K(k_4)}{K(k_4')}. \tag{2.50}$$

Under the quasi-static approximation model, ϵ_{eff}, υ_p, and Z_0 can be determined. In this approach, ϵ_{eff} will be equal to ratio of capacitances as follows

$$\epsilon_{eff} = \frac{C_{CPW}}{C_{air}}. \tag{2.51}$$

Equation (2.51) can be expanded by substituting Equations (2.45) and (2.50) and the final form of ϵ_{eff} is determined as

$$\epsilon_{eff} = 1 + q_1(\epsilon_1 - 1) + q_2(\epsilon_2 - 1). \tag{2.52}$$

Here, q_1 and q_1 are called the partial filling factors, and they are equal to:

$$\begin{aligned} q_1 &= \frac{K(k_1)}{K(k_1')}[\frac{K(k_3)}{K(k_3')} + \frac{K(k_4)}{K(k_4')}]^{-1}, & (2.53)\\ q_2 &= \frac{K(k_2)}{K(k_2')}[\frac{K(k_3)}{K(k_3')} + \frac{K(k_4)}{K(k_4')}]^{-1}. & (2.54) \end{aligned}$$

Considering ϵ_{eff}, the phase velocity (υ_p) can be found by

$$\upsilon_p = \frac{c}{\sqrt{\epsilon_{eff}}} \tag{2.55}$$

where c is the velocity of light in free space. Moreover, the relation between Z_0 and υ_p can be defined as

$$Z_0 = \frac{1}{C_{CPW}\upsilon_p}. \tag{2.56}$$

By substituting Equations (2.45), (2.51), and (2.55) into (2.56), final expression of Z_0 can be obtained

$$\begin{aligned} Z_0 &= \frac{1}{cC_{air}\sqrt{\epsilon_{eff}}} \\ &= \frac{60\pi}{\sqrt{\epsilon_{eff}}}[\frac{K(k_3)}{K(k'_3)} + \frac{K(k_4)}{K(k'_4)}]^{-1}. \end{aligned} \tag{2.57}$$

In this work, conventional CPW is sandwiched between two identical layers. Consequently, certain parameters of the structure illustrated in Figure 2.10 are modified to $h_3 = h_4 = \infty$ and $\epsilon_1 = \epsilon_2$. According to these changes, Equation (2.46) and (2.47) simplify to

$$k_3 = k_4 = k_0 = \frac{a}{a+2b} \tag{2.58}$$

which leads to

$$K(k_3) = K(k_4) = K(k_0). \tag{2.59}$$

By substituting Equation (2.59) into Equation (2.53) and (2.54), partial filling factors become:

$$q_1 = \frac{1}{2}\frac{K(k_1)}{K(k'_1)}\frac{K(k'_0)}{K(k_0)}, \tag{2.60}$$

$$q_2 = \frac{1}{2}\frac{K(k_2)}{K(k'_2)}\frac{K(k'_0)}{K(k_0)}. \tag{2.61}$$

Also, C_{air} from Equation (2.45) simplifies to

$$C_{air} = 4\epsilon_0\frac{K(k_0)}{K(k'_0)}. \tag{2.62}$$

Finally, these adjusted parameters can be substituted into Equation (2.52) and (2.57) in order to formulate ϵ_{eff} and Z_0 as follows

$$\epsilon_{eff} = 1 + (q_1 + q_2)(\epsilon_1 - 1), \tag{2.63}$$

$$Z_0 = \frac{30\pi}{\sqrt{\epsilon_{eff}}}\frac{K(k'_0)}{K(k_0)} \tag{2.64}$$

The parameters for the sandwiched CPW are determined using the equations described above. To validate these calculations, a CPW calculator provided by [93] is used. Initially, the CPW design is completed for HPFS layers with a relative permittivity value of 11. However, the CPW is sandwiched between RTV-2 silicon layers instead of HPFS due to practical challenges in fabrication. If the feed were to be realized on HPFS, its trace width would be as low as 0.5 mm, which may increase fabrication errors because of requiring high sensitivity and also compromise durability due to the thin trace width. The optimized parameters and the comparison between HPFS and RTV-2 silicon layers are given in Table 2.2.

Table 2.2. Optimized parameters of CPW design with respect to the various sandwiching layers.

Sandwiching Layers	ϵ_r	$\mathbf{h_1}$	$\mathbf{h_2}$	**a**	**b**	Z_0
HPFS	11.2	1 mm	1 mm	0.5 mm	1.5 mm	50.6 Ω
RTV-2 Silicon	3.1	1 mm	1 mm	2 mm	1.5 mm	49.5 Ω

2.6. Coplanar Waveguide-Fed Loop Antenna and On-Body Performance

2.6.1. Effect of the Human Body and Major Challenges

In WBAN applications, antennas which are placed close to the human body are exposed to a hostile environment in terms of electromagnetic radiation [94]. Human body tissues contain water, organic molecules, ions, and electrolytes, resulting in high relative permittivity and conductivity values. Therefore, placing an antenna on or near the inherently lossy human body may have consequences such as reduced antenna efficiency, resonance frequency detuning, impedance mismatch, and distortions in radiation pattern [95].

The diverse composition of human body tissues among individuals poses an additional challenge to designing antennas that perform effectively for everyone. Moreover, it should be emphasized that the location where the antenna is placed changes the antenna performance because of the variations in dielectric properties of different tissues.

Therefore, meticulous antenna design is essential to minimize deterioration and resonance frequency shifts [96]. Consequently, antennas should be designed and optimized on human body phantoms in order to tackle these challenges [22].

2.6.2. On-Body Antenna Optimization

In the previous sections, all required steps for the antenna design are provided in detail. Based on these steps, the antenna chosen for this work is determined as a CPW-fed loop antenna fabricated on an HPFS with a relative permittivity value of 11.2. Once the antenna is chosen, its design, optimization and related simulations are conducted in ANSYS High-Frequency Structural Simulator(HFSS) [97]. The proposed CPW-fed loop antenna and its dimension parameters are shown in Figure 2.12. Also, dimension parameters are listed in Table 2.3.

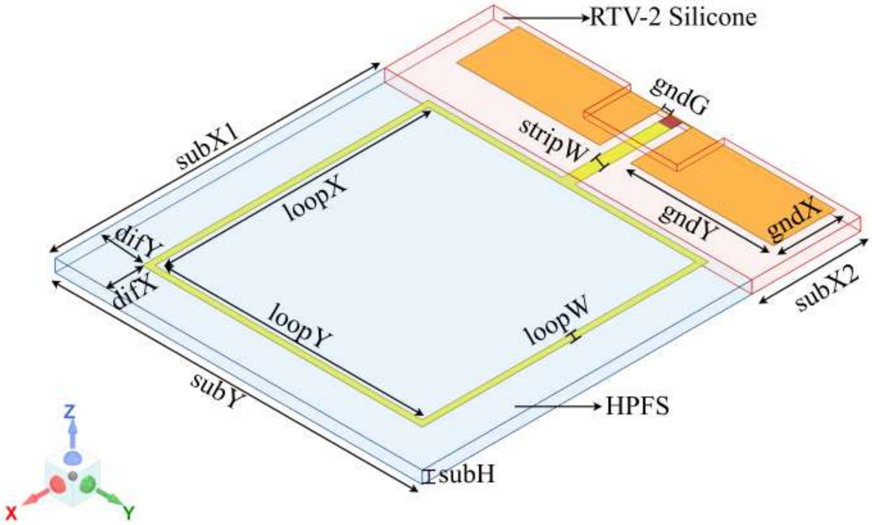

Figure 2.12. The proposed CPW loop antenna.

Table 2.3 presents the initial parameters of the proposed antenna. The main parameters of the CPW are explained in Section 2.5 and the ground dimensions(gndX and gndY) of the CPW are optimized through simulations. Substrate height is discussed in Section 2.4 and the substrate dimensions(subX1 and subY), which are directly related to the circumference(C) and difference(dif) parameters, are optimized for measurements. The loop width(loopW) is chosen as 1 mm to minimize the production error. Lastly, loop dimensions(loopX and loopY) are theoretically calculated and optimized based on the other parameters.

Table 2.3. Dimension parameters of the initial CPW-fed loop antenna.

Parameter	**Dim. (mm)**	**Parameter**	**Dim. (mm)**
loopX	56	difX	7
loopY	56	difY	7
loopW	1	stripW	2
subX1	65	gndX	10
subY	72	gndY	26.5
subH	2	gndG	1.5
subX2	17.5	C = 2loopX+2loopY	224

Initially, the effective permittivity of the sandwiched loop antenna structure is assumed to be 11.2 and the one-wavelength circumference is calculated to achieve the frequency of operation 403 MHz. As a reminder, the calculation is as follows

$$c = \lambda_0 f, \tag{2.65}$$

$$C = \lambda_g = \frac{\lambda_0}{\sqrt{\epsilon_{eff}}}. \tag{2.66}$$

In Equation (2.65), the free space wavelength of the loop for 403 MHz operation frequency is calculated as 74.4 cm. Subsequently, the size of the loop is found as 22.4 cm by using Equation (2.66). The return loss plots of the proposed antenna on the simplified body phantom depicted in Figure 2.6 is demonstrated in Figure 2.13. By using the C value of 22.4, the operation frequency of the antenna appears at 306 MHz. Therefore, it is required to make a parametric analysis to match the antenna at 403 MHz. In order to increase the resonant frequency, C should be decreased since C is directly proportional to λ_g. The deviation from the calculation given in Equation (2.66) can be attributed to the miscalculated ϵ_{eff}.

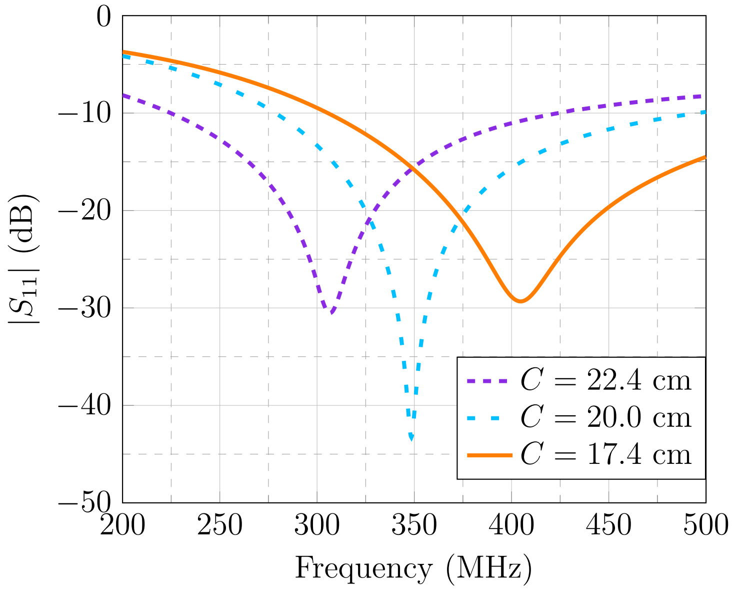

Figure 2.13. Reflection coefficient plots for different circumference(C) values of the proposed loop antenna.

The calculation of ϵ_{eff} is conducted through Equation (2.25), however; it is necessary to know the filling factor(ff) of the loop antenna. As mentioned in Section 2.3, ff can be determined by reverse engineering for each antenna type. With a C value of 17.4 cm, yielding the desired resonant frequency as shown in Figure 2.13, ϵ_{eff} should be approximately 18.5. If Equation (2.25) is adjusted for the introduced antenna setup, it becomes as follows

$$\epsilon_{eff} = 18.5 = \epsilon_{r,HPFS} \cdot ff + \epsilon_{r,Muscle} \cdot (1 - ff). \tag{2.67}$$

According to Equation (2.67), ff of the proposed loop antenna is found to be 85% by substituting the relative permittivity values of the HPFS and muscle tissue at 403 MHz. After the fine-tuning procedure, the final dimension parameters are listed in Table 2.4.

Figure 2.13 illustrates that the proposed antenna has a bandwidth of approximately 200 MHz. This relatively large bandwidth is advantageous for tackling any detuning caused by changes in dielectric load or bending. Additionally, the simulation setup depicted in Figure 2.14 is prepared to check the conformability of the proposed antenna. In order to mimic real-life applications, the proposed antenna is wrapped around a cylinder representing the human torso. The phantom model is similar to the one in Figure 2.6. The effect of bending is analyzed by variating the outer radius(Rout) of the cylinder gradually.

Table 2.4. Dimension parameters of the optimized CPW-fed loop antenna.

Parameter	**Dim. (mm)**	**Parameter**	**Dim. (mm)**
loopX	44	difX	7
loopY	43	difY	7
loopW	1	stripW	2
subX1	53	gndX	10
subY	59	gndY	23
subH	2	gndG	1.5
subX2	17.5	C = 2loopX+2loopY	174

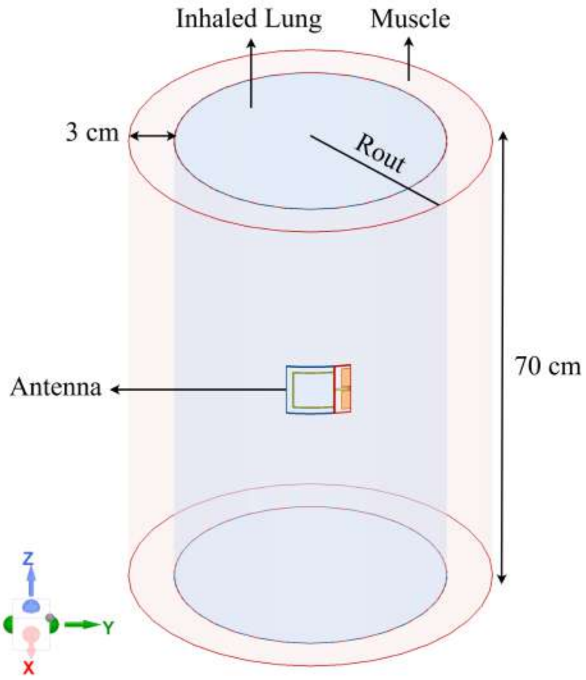

Figure 2.14. The simulation model prepared for the conformability analysis.

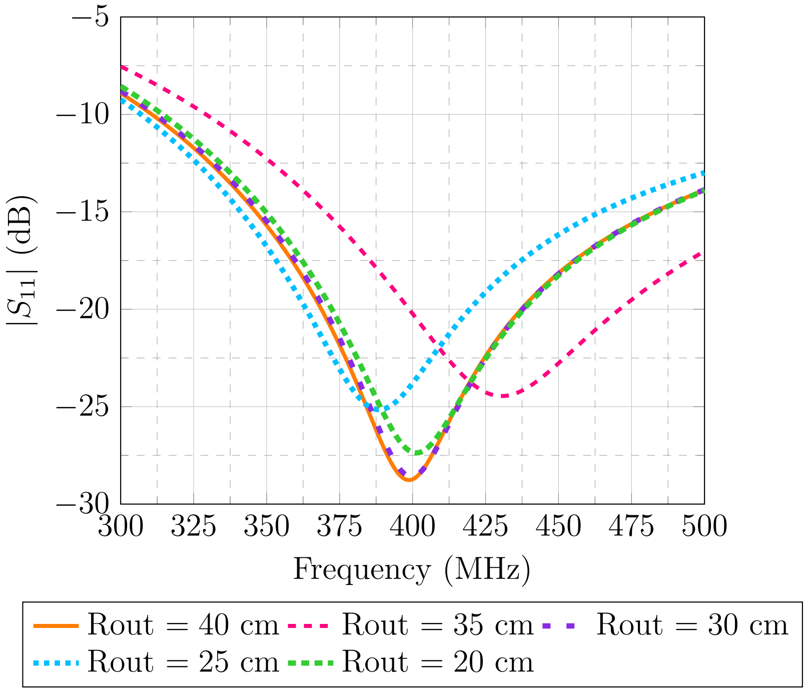

Figure 2.15. The conformability analysis, the reflection coefficient plots for variating Rout values.

As seen in Figure 2.15, the proposed antenna exhibit a consistent $|S_{11}|$ performance with less than 6.5% detuning. The reflection coefficient value is less than -20 dB for each Rout value throughout the MICS band. Therefore, it can be deduced that the antenna is well-suited to use in a wearable application.

Furthermore, the on-body radiation pattern of the proposed antenna is illustrated in Figure 2.16. The radiation pattern is simulated at the antenna's first resonant frequency(403 MHz) with a maximum gain of -18.95 dB. The reason behind this relatively low gain value might be attributed to the presence of lossy human tissue in the near-field of the antenna. Moreover, the 1 g average SAR value simulated at the resonant frequency for an incident power of 10 mW is found to be 0.292 W/kg abiding by the limit of 2 W/kg set in the European Standards.

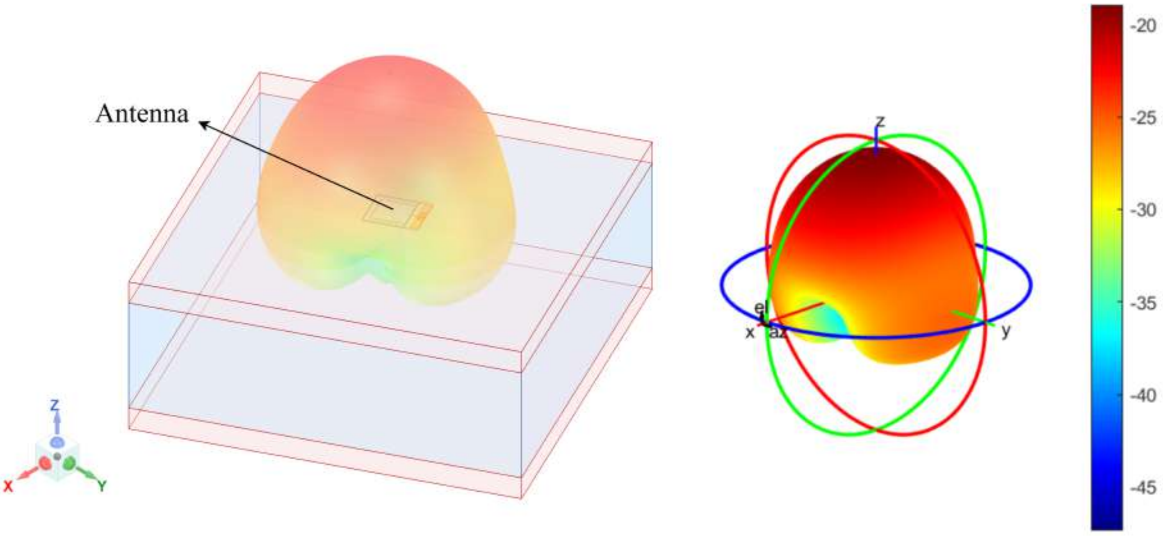

(a) (b)

Figure 2.16. The on-body radiation pattern of the proposed antenna: (a) The radiation pattern on the simple phantom (b) The 3D gain plot.

2.7. Antenna Fabrication

The fabrication process for the on-body flexible antenna involves several steps, due to its composition of two materials: HPFS and RTV-2 silicone, as described in earlier sections. The procedure to be followed for the antenna fabrication is given step by step below:

(i) The mould for the specific design is printed via a stereolithography(SLA) 3D printer.
(ii) HPFS material is prepared according to the instructions provided in Figure 2.4.
(iii) The moulds are assembled, ensuring only the radiating loop section of the substrate is made of HPFS.
(iv) The prepared HPFS is poured into the mould and placed in the vacuum oven for degassing.
(v) In order to have a smooth surface for the conductor, the mould is sandwiched via nuts.
(vi) HPFS is left at room temperature until it is completely cured.

(vii) Once HPFS is cured, the moulds are separated and RTV-2 silicone is poured into the other half.

(viii) The mould is sandwiched via nuts again, RTV-2 silicone is left to cure at room temperature.

(ix) When the substrate is prepared, the copper sheets for radiation, produced with ”Silhouette Cameo 4 Blade Cutter”, are placed onto it.

(x) Moulds for the superstrate are assembled, ensuring only the radiating loop part is made of HPFS.

(xi) The mould is sandwiched via nuts and the superstrate is left at room temperature until HPFS is completely cured.

(xii) After the HPFS part of the superstrate is cured, RTV-2 silicone is poured into the mould, and the curing process is repeated as before.

(xiii) Finally, the SMA connector is soldered to the antenna.

This method ensures the proper fabrication of the on-body flexible antenna, incorporating the necessary materials and techniques for its construction. Also, the fabrication steps are illustrated in Figure 2.17.

Table 2.5. The first resonant frequency and the reflection coefficient values at the first resonant and 403 MHz of the proposed antenna on simulation, phantom, and human body.

	Frequency(MHz)	**dB at Resonance**	**dB at 403 MHz**
Simulation	403.7	-29.32	-29.26
Phantom	383.8	-17.28	-16.38
Human Body	359.8	-18.49	-14.56

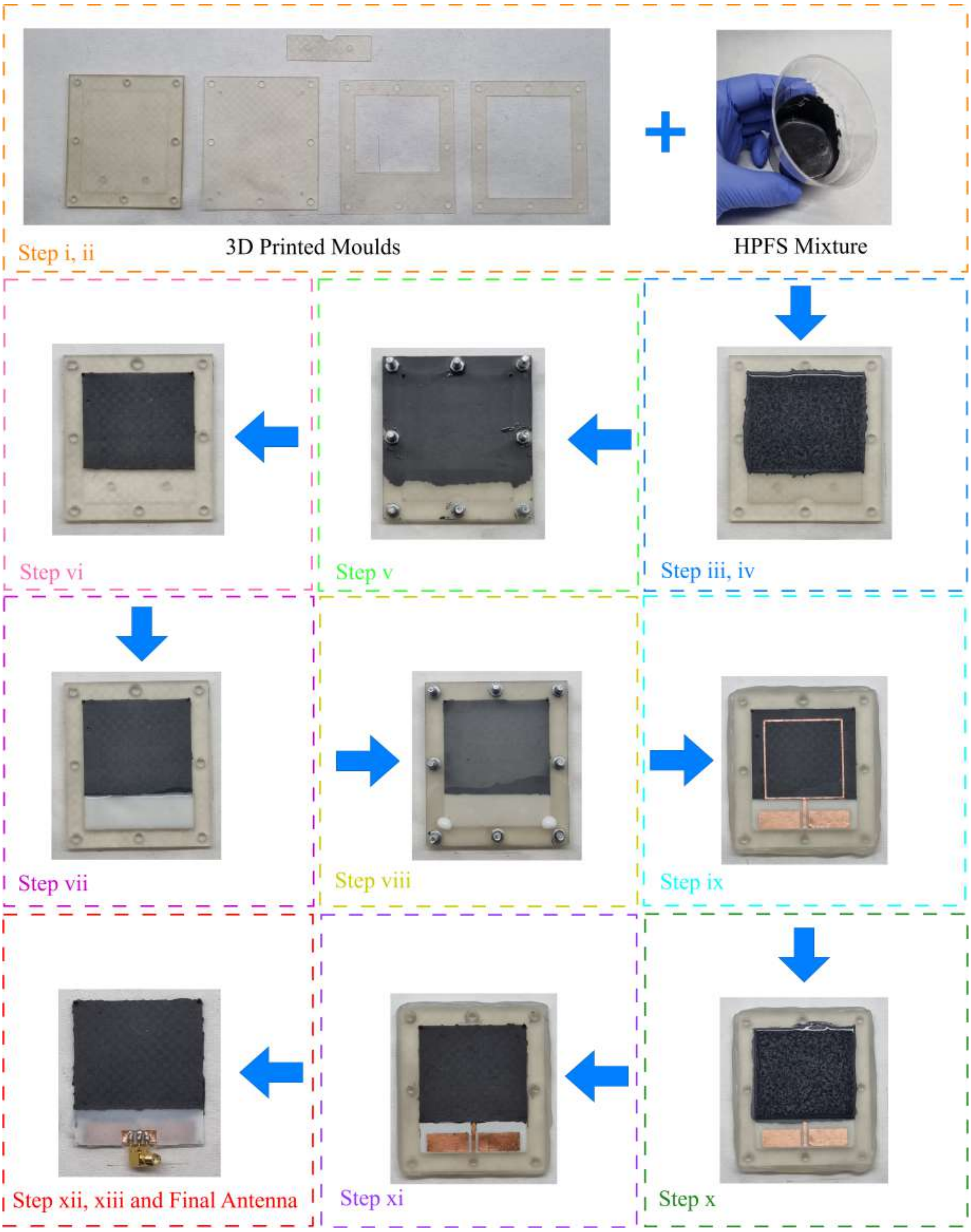

Figure 2.17. Fabrication process of the on-body flexible loop antenna.

In Figure 2.18, simulated and measured reflection coefficient plots of the proposed antenna are illustrated. Also, the first resonant frequency and reflection coefficient values at the resonant frequency are in Table 2.5. Additionally, the reflection coefficients at 403 MHz are included in the table in order to demonstrate that the antenna is operational in the frequency of operation. In the measured reflection coefficients, a shift in resonant frequency is observed. The antenna is designed based on the simplified model, discussed further in the subsequent chapter. Hence, the frequency shift is about 20 MHz in the measurements with phantom due to the similarity between the simulations and the measurement setup. This minor deviation may stem from factors such as the phantom used and fabrication-related issues. However, the deviation from the simulation is greater in human body measurements. This discrepancy is not a surprising result due to the variations in individual body compositions. Even though resonant frequency shifts are observed in phantom and human body measurements, the large bandwidth characteristics of the proposed antenna provide that the antenna is still operating in the MICS band with less than −14.5 dB of reflection coefficient.

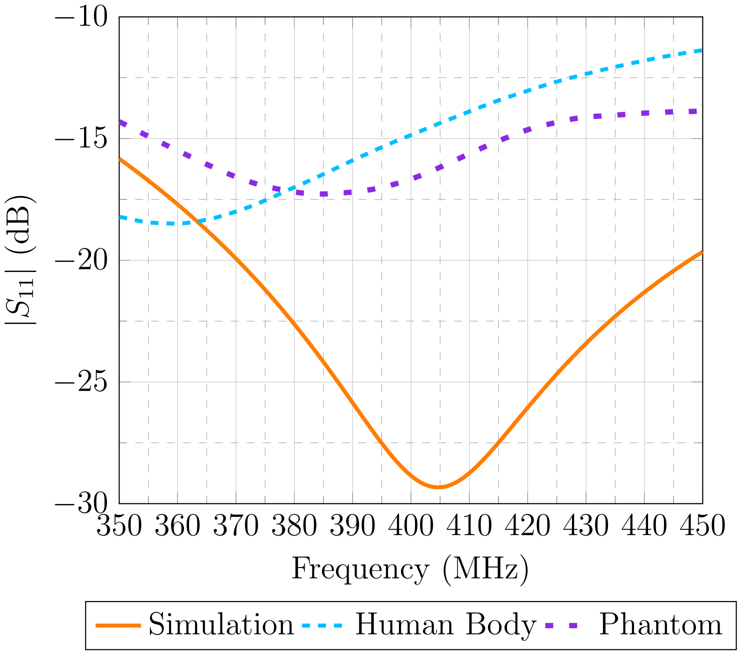

Figure 2.18. Simulated and measured reflection coefficient plots of the proposed antenna.

3. NUMERICAL MODELS AND RESULTS

In this chapter, numerical models and simulations are presented in detail, along with a comprehensive analysis of related results. The realistic simulation model and its simplification are explained in Section 3.1. This part is followed by Section 3.2 where the PE condition is simulated and the severity analysis based on the saline amount in the lung tissue is provided. Subsequently, Section 3.3 discusses how the transmission coefficient between the anterior and posterior antennas is related to PE and its severity.

3.1. Simplification of the Simulation Model

In the ANSYS HFSS simulation of the realistic human model, depicted in Figure 3.1, various organ and bone tissues are included, such as the lung, rib cage, heart, sternum, and stomach. These tissues have distinct shapes and dielectric properties, leading to longer simulation times and increased computational costs. Therefore, simplifying the realistic human model is essential to expedite progress. In order to simplify the realistic model, there are crucial parameters to determine as follows:

- Dimensions of the realistic human phantom
- Distances between the antennas and lungs
- Lung sizes such as radius and height
- Dielectric properties of the tissues

Initially, the total size of the simplified model is determined by using the values given in Figure 3.1(a). The final dimensions of the simplified model become 36 cm × 26 cm × 30 cm. Subsequently, two cylinders representing lungs are placed within the muscle phantom. The approximate dimensions of the lungs are illustrated in Figure 3.2. It is known that the left lung is smaller than the right lung due to the presence of the heart, as depicted in the figure. Still, two cylinders with a height of 28 cm and a radius of 13 cm are utilized to represent the right and left lungs, respectively.

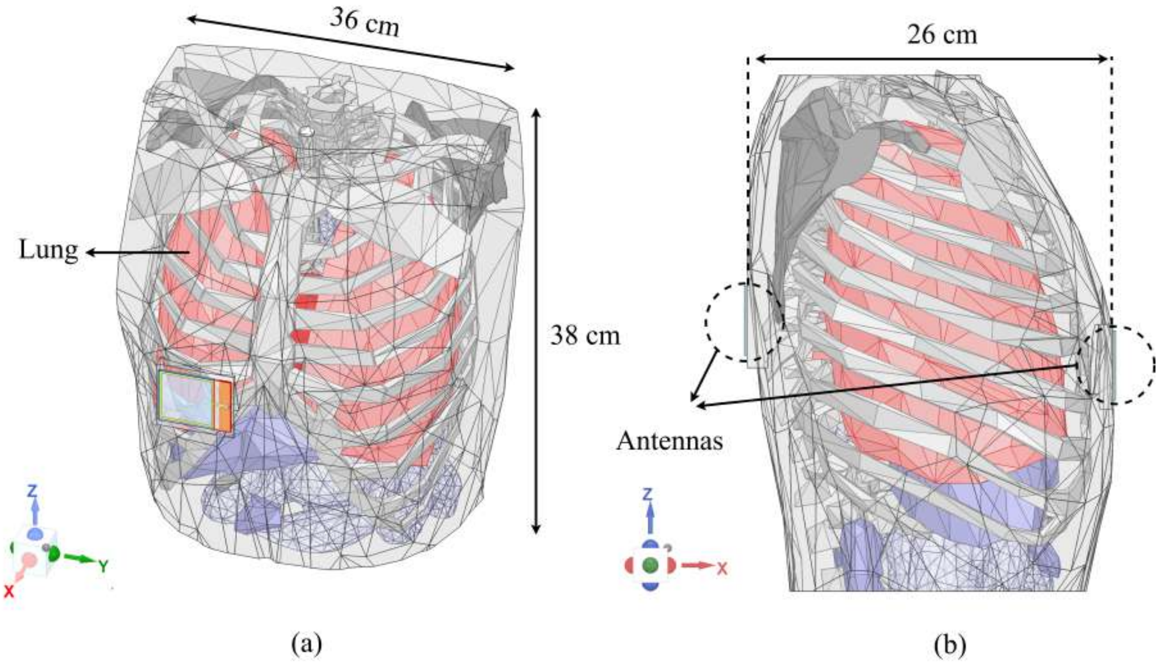

Figure 3.1. The realistic human model with approximate dimensions in HFSS: (a) Isometric view (b) Side view.

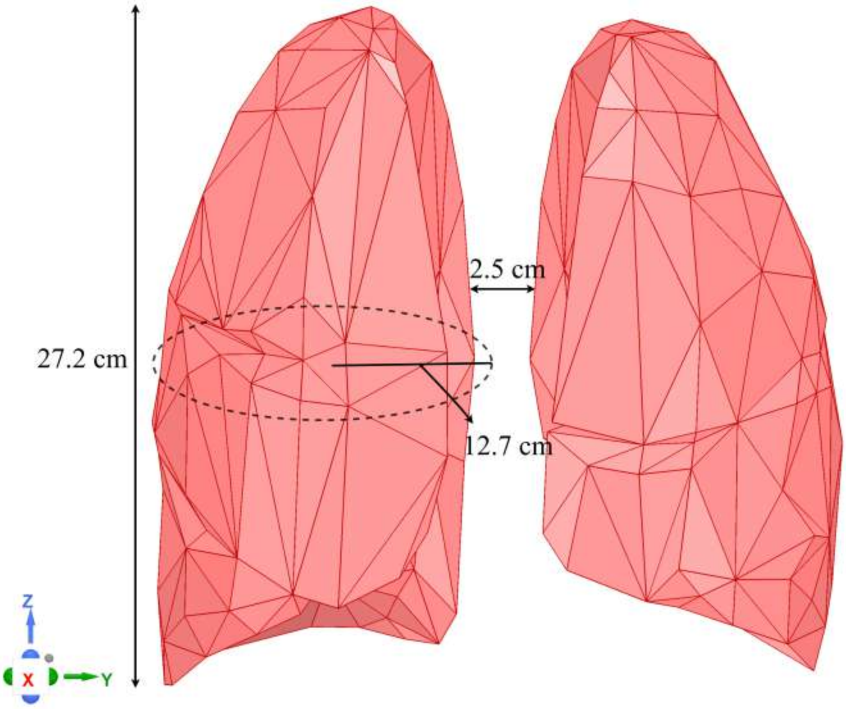

Figure 3.2. Approximate lung dimensions in the realistic human model.

Once the sizes of the simplified model are established, the dielectric properties of the simplified tissues are assigned. Instead of employing a multilayer phantom model, cylinders are designated to represent the inhaled lungs, while the remaining portion of the rectangular box is assigned to be muscle tissue. The results are expected to be similar by using only muscle based on the understanding that muscle tissue surrounds bones, organs, and other tissues. Frequency-dependent dielectric properties of muscle and inhaled lung tissues are given in Figure 3.3. Also, it could be observed that the relative permittivity and conductivity values of inflated lung and muscle tissue given in Table 1.1 are compatible with the frequency-dependent data.

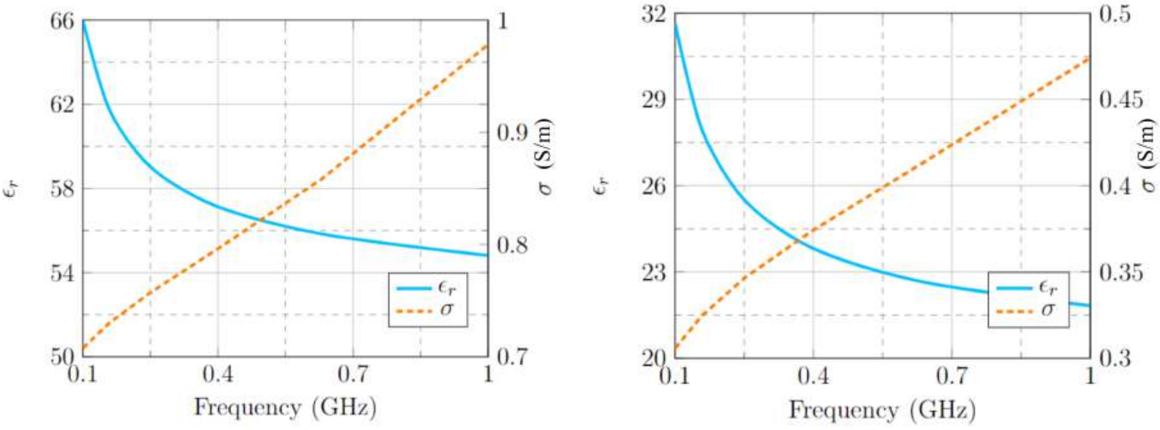

(a)

(b)

Figure 3.3. Frequency-dependent dielectric properties of phantoms in the simplified model: (a) Muscle (b) Inflated Lung.

As a result, the proposed simplified model and the positions of the antennas are demonstrated in Figure 3.4. Furthermore, the coherence between the simplified and realistic model is proved in Figure 3.5. The frequency range for the analysis is from 400 MHz to 406 MHz since the frequency range of interest is the MICS band in this work. The return loss values in both models are almost linear in this frequency range due to the wideband characteristics of the proposed loop antenna. It should be emphasized that the reflection coefficients of both models are less than −25 dB, which means that the antennas are operational in both models. Furthermore, the difference in transmission coefficients in both models is less than 2 dB, showing that employing a huge muscle phantom instead of a multilayer phantom is sufficient for the simplified model.

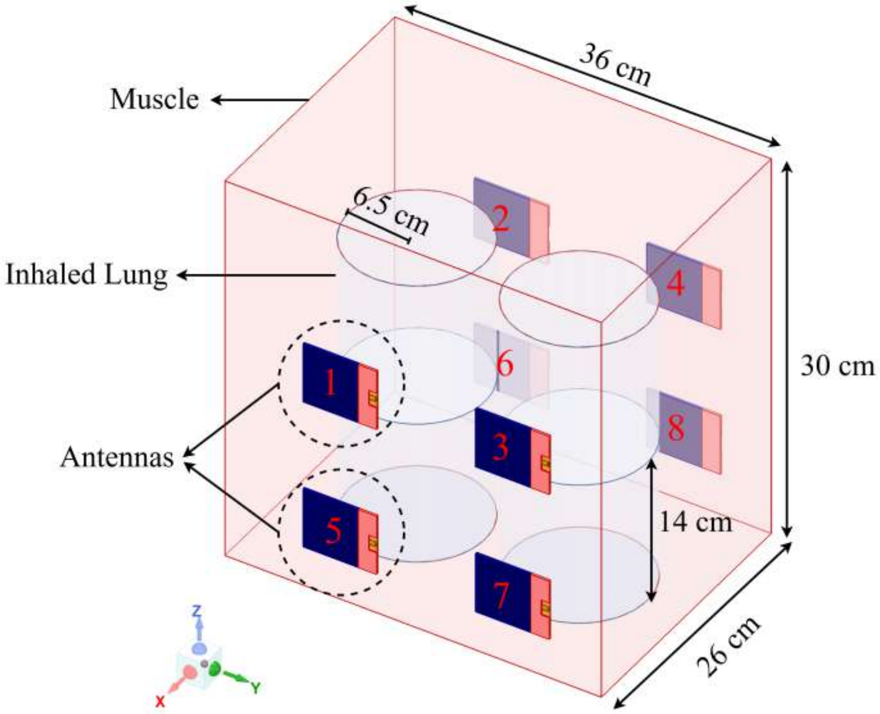

Figure 3.4. The simplified simulation setup: Four-element antenna array covering the lungs inside the torso model.

The 2D and 3D radiation patterns of the proposed on-body loop antenna on both models at the first resonant frequency are provided in Figure 3.7. Both 2D and 3D patterns show similar radiation characteristics, indicating that antennas operate in the same mode in both models. The maximum gain values are -19.65 dB and -19.79 dB for the realistic and simplified models, respectively. Also, 2D radiation patterns depicted in Figure 3.7(a) and (b) demonstrate that the maximum radiation of the antenna in both models stays the same.

We made sure that the realistic model could be replaced with the simplified model by comparing the antenna's input and transmission responses on both of them. After confirming the suitability of using the simplified model over the realistic model, it is important to check the coupling between the antennas on the same side of the torso.

The positioning of the antennas on the anterior torso is identical to the posterior. Hence, it is sufficient to check the coupling between one set. Therefore, simulation results of the coupling check of the anterior antennas are demonstrated in Figure 3.6. It is observed that the maximum coupling between the antennas is less than 42.5 dB, which is acceptable for the use of antenna arrays in the proposed model.

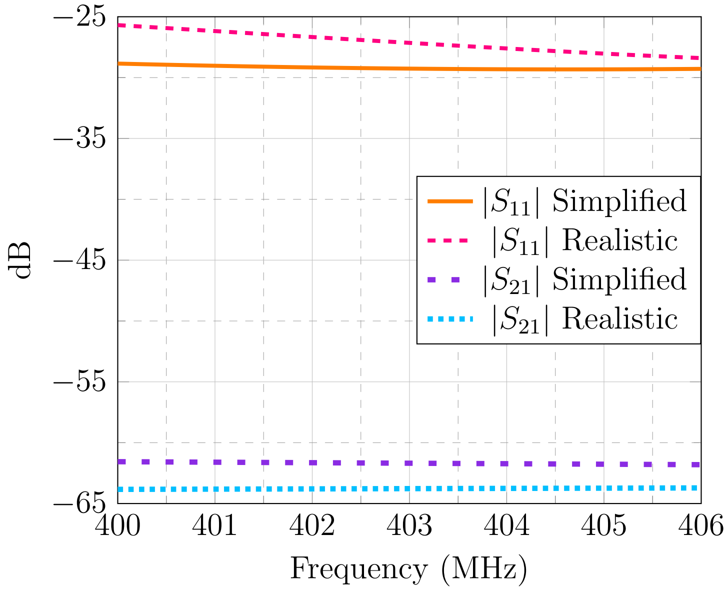

Figure 3.5. Reflection and transmission coefficient analysis of the simplified and realistic model in the MICS band.

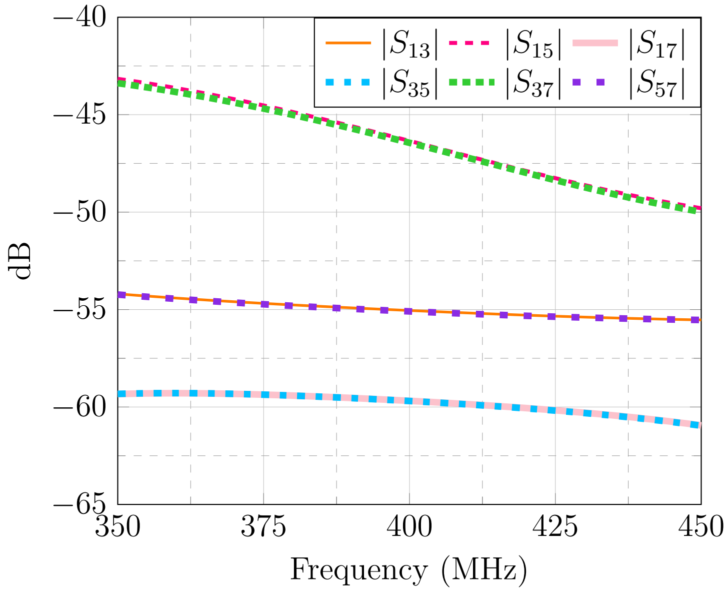

Figure 3.6. The coupling analysis of the anterior antennas.

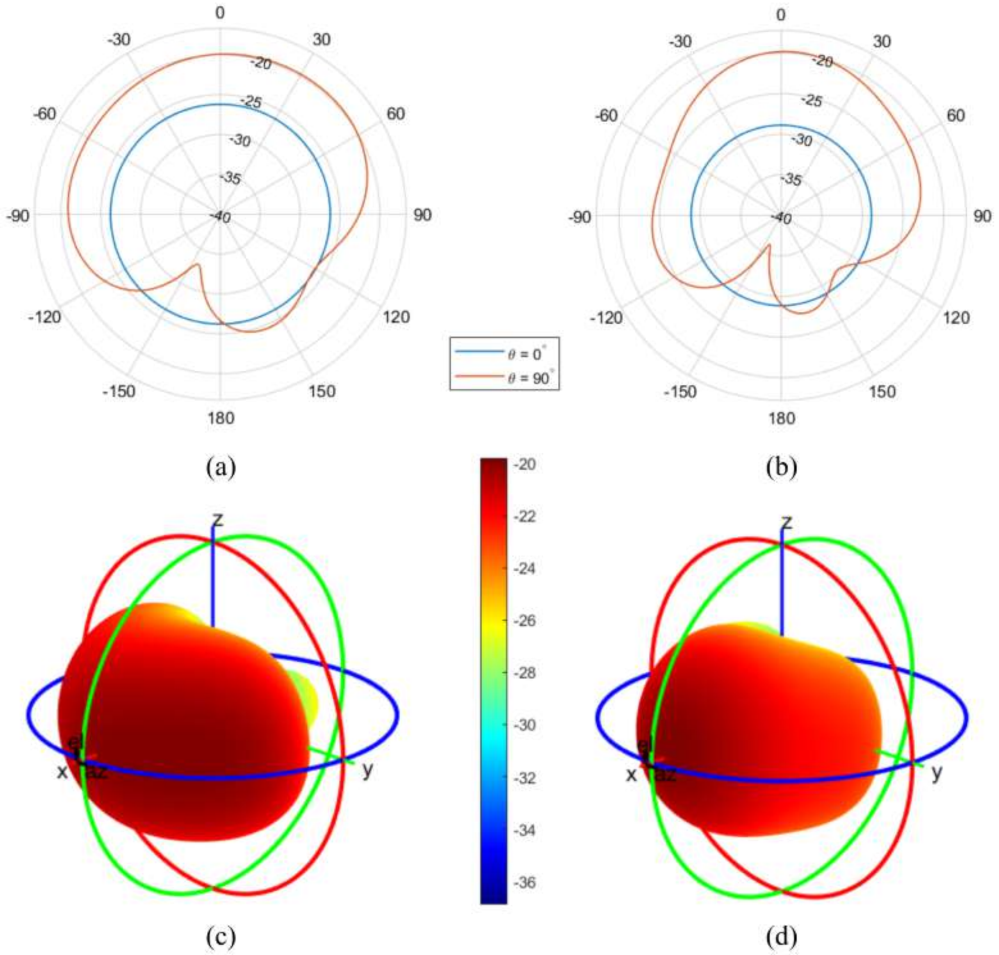

(a) (b) (c) (d)

Figure 3.7. The simulated 3D and 2D radiation patterns of the proposed antenna on the realistic and simplified models: (a) & (c) Realistic (b) & (d) Simplified.

3.2. Modeling Different Severity Levels of PE

In the case of PE, the alveoli in the lungs are filled up with a saline solution consisting of NaCl dissolved in water. The overall mass density of the solvent is 1.0046 g/cm^3 [2]. However, the dielectric properties of saline vary with both frequency and temperature, requiring calculations to determine these properties accurately. Preliminary works indicate that the dielectric properties could be represented by polynomial equations [98]. By employing these equations, it is found that the saline solution at body temperature (37°) has a relative permittivity value of 72.47 F/m and conductivity of 1.86 S/m at 400 MHz [2].

In the provided data by [25], the dielectric properties of inflated lung tissue are known, with relative permittivity of 23.8 and conductivity of 0.375, and they are shown in Table 1.1. Therefore, it is expected to observe that both the relative permittivity and conductivity are between the ranges of $[23.8, 72.47)$ and $[0.375, 1.86)$, respectively. As the amount of saline increases, both the relative permittivity and conductivity of the malignant lung tissue come closer to the upper bound. That is how the PE case is simulated with different severity cases in the simulations. These dielectric properties are assumed to be linearly dependent on the amount of saline build-up. So, the dielectric properties of malignant lung tissues with different PE severities are demonstrated in Table 3.1. Notably, the dielectric properties of 100% severity are not equal to the properties of saline due to the presence of lung tissue.

Table 3.1. Relative permittivity(ϵ_r) and electrical conductivity(σ) values of malignant lung tissue for different severity levels.

Edema Level	**Edema Severity**	ϵ_r	σ **(S/m)**
Healthy	0%	23.8	0.374
1	25%	35.4	0.731
2	50%	47	1.088
3	75%	58.6	1.445
4	100%	70.2	1.800

3.3. Transmission Analysis

The transmission analysis aims to localize and assess the severity of PE. Briefly, localization involves identifying the specific areas within the lungs where saline accumulation occurs, while severity analysis determines the extent of this accumulation. Due to the changed dielectric properties of the lung tissue during PE, depicted in Table 3.1, it is anticipated to observe variations in the level of the transmitted signal. In Figure 3.8, the return loss values of all antennas are given to be sure that all antennas are operating in the desired frequency band. Based on the simulation results, all antennas are operational, allowing the transmission analysis to proceed.

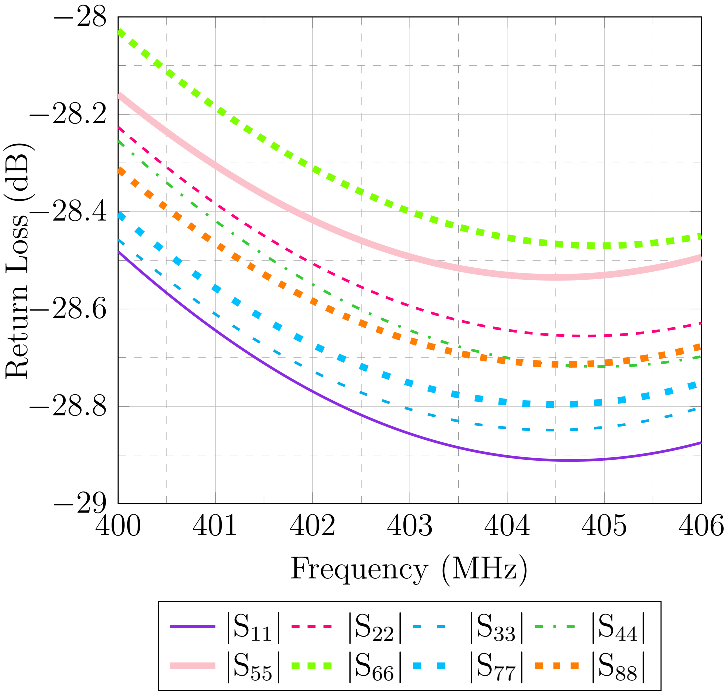

Figure 3.8. The reflection coefficient analysis of all anterior and posterior antennas.

In Figure 3.9, forward transmission coefficients for all posterior antennas, $|S_{2n}|$, $|S_{4n}|$, $|S_{6n}|$, $|S_{8n}|$, are illustrated. The plots consist of the direct and cross channels between the antennas. The largest transmission coefficient is the one in which the antenna pair directly faces each other with a distance of 26 cm for all cases. At the same time, the other transmission coefficients are less than −65 dB. This is mostly due to the increased antenna separation in these propagation channels. Small variations in transmission coefficients for upper pairs, Figure 3.9(a) and (b), and lower pairs, Figure 3.9(c) and (d), can be attributed to the antenna orientation in the setup in Figure 3.4. The antennas are placed so that the centres of the cylinders and loops are aligned. Hence, CPW feeding is between the conductive loop and the edge of the muscle block on the right side. Despite these small variations, all simulation results are as expected since the main factors are the propagation distance and dielectric properties of the lungs.

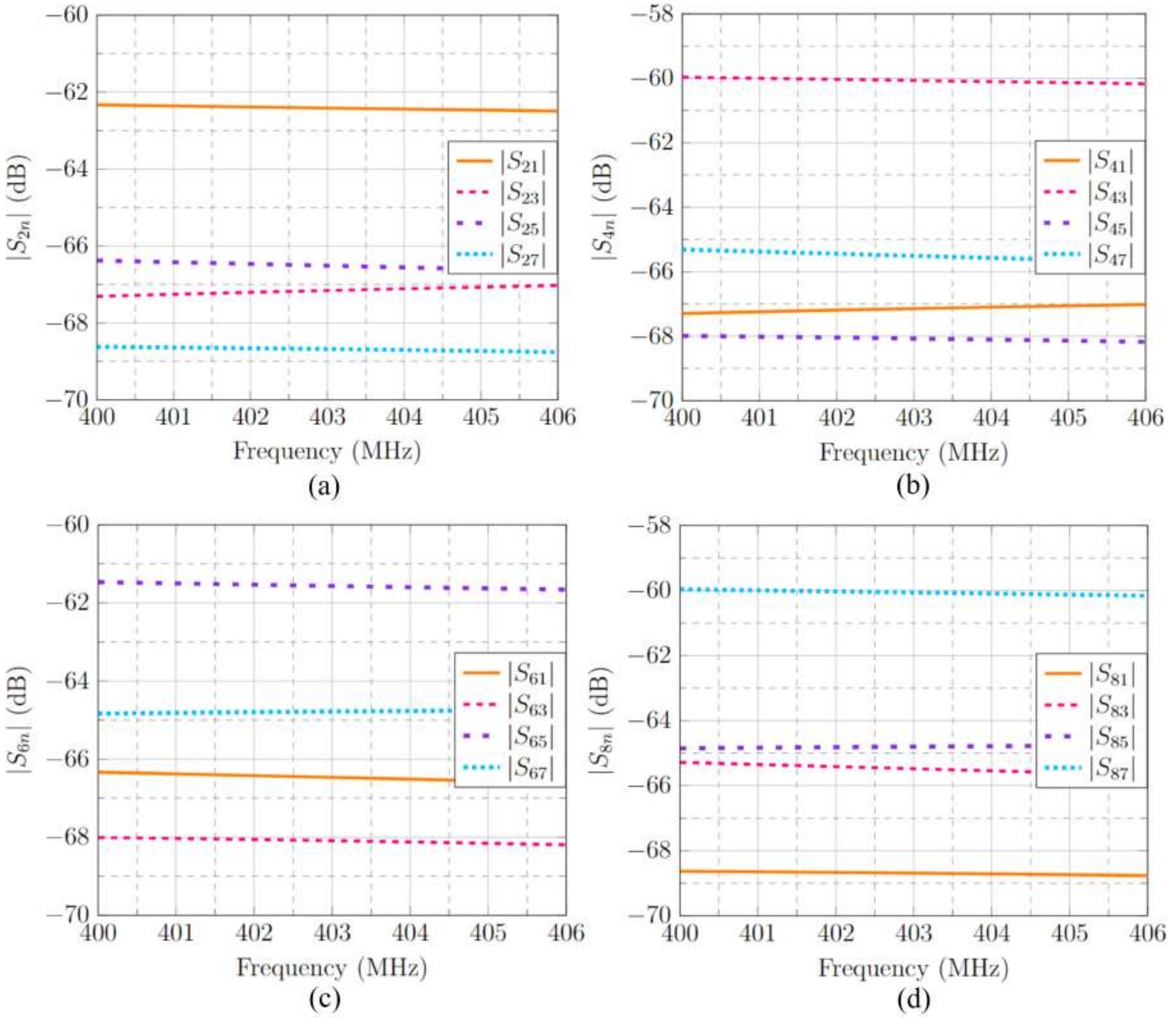

Figure 3.9. Transmission coefficient plots of all posterior antennas for healthy lung case: (a) Antenna #2 (b) Antenna #4 (c) Antenna #6 (d) Antenna #8.

Given the similarity in the outcomes, severity and localization analysis could proceed using antenna pairs 1 & 2 and 7 & 8. These pairs correspond to the simplified lung's upper left lobe and lower right lobe, respectively. In Figure 3.10, transmission coefficients of directly facing anterior and posterior antennas are depicted when different levels of edema are introduced to the upper left lobe. The introduction of PE results in the deterioration of transmission coefficients between the antennas due to the increased conductivity. However, this deterioration is particularly evident for the antenna pair covering the sick lobe. For instance, in Figure 3.10(a), $|S_{21}|$ decreases by approximately 8 dB from healthy to edema level 4 cases. On the other hand, the maximum transmission coefficient drop, other than $|S_{21}|$, is observed in $|S_{65}|$, given in Figure 3.10(c), which corresponds to the lower left lobe. This difference in $|S_{65}|$ is about 0.5 dB and caused by the proximity to the sick lobe. The other transmission coefficients, $|S_{43}|$ and $|S_{87}|$, remain largely consistent across all edema levels. Therefore, detection of the approximate location of PE and estimation of the amount of saline build-up could be facilitated by analyzing transmission coefficient variations in directly facing antennas.

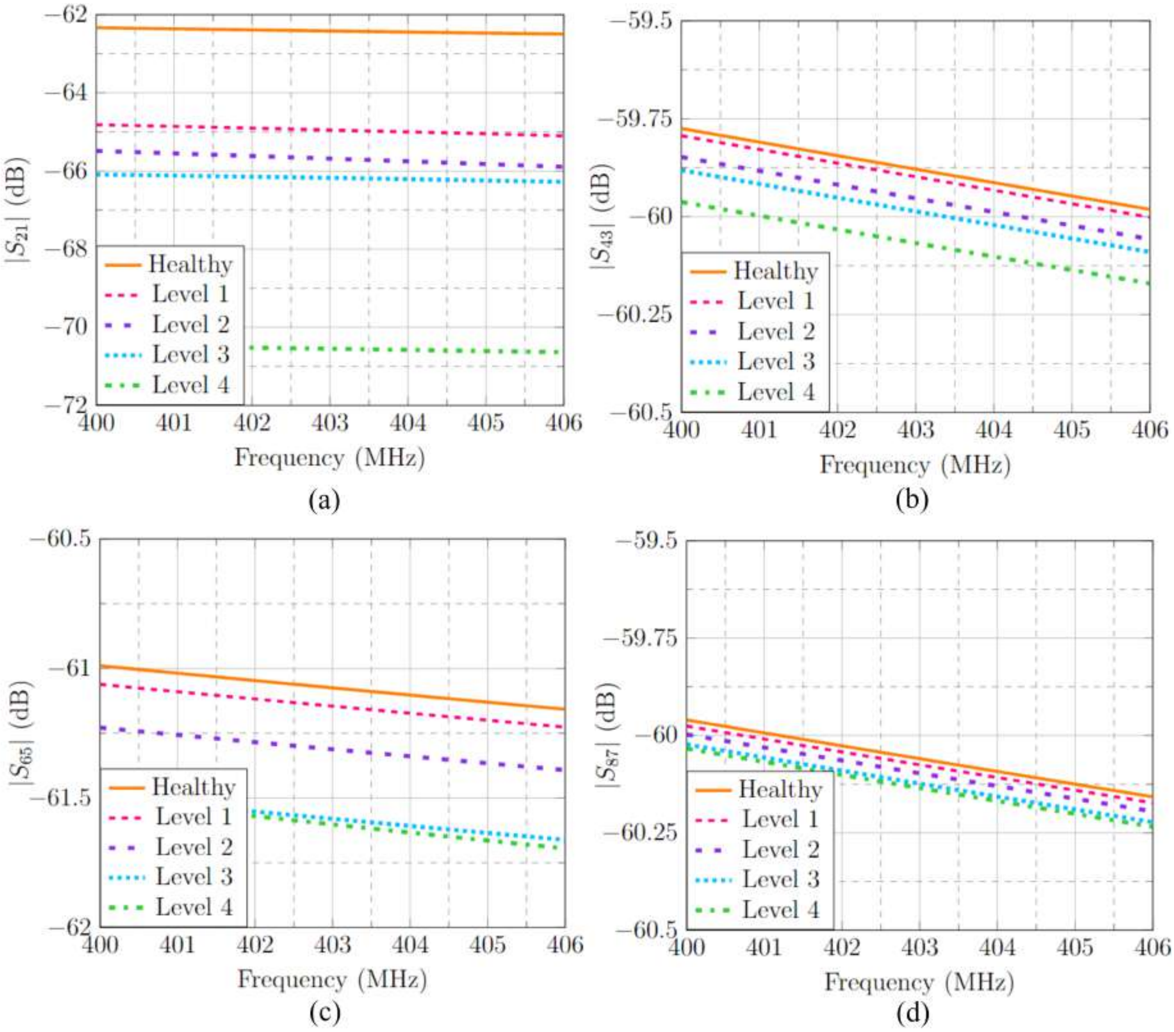

(a) (b) (c) (d)

Figure 3.10. Transmission coefficient plots of directly facing anterior and posterior antennas when different levels of edema are introduced to upper left lobe: (a) $|S_{21}|$ (b) $|S_{43}|$ (c) $|S_{65}|$ (d) $|S_{87}|$.

Furthermore, Figure 3.11 illustrates the transmission coefficients of directly facing antennas when different levels of edema are introduced to the lower right lobe. Similar to the upper right lobe scenario, the introduction of PE results in reduced transmission performance due to the increased conductivity. The deterioration in $|S_{21}|$, $|S_{43}|$, $|S_{65}|$ do not exceed 1 dB while the $|S_{87}|$ experiences a change of approximately 7 dB, indicating the location of fluid build-up. Notably, Figure 3.11(d) shows a significant change in $|S_{87}|$ from healthy to edema level 1, unlike other severity levels. However, variations in edema levels remain distinguishable.

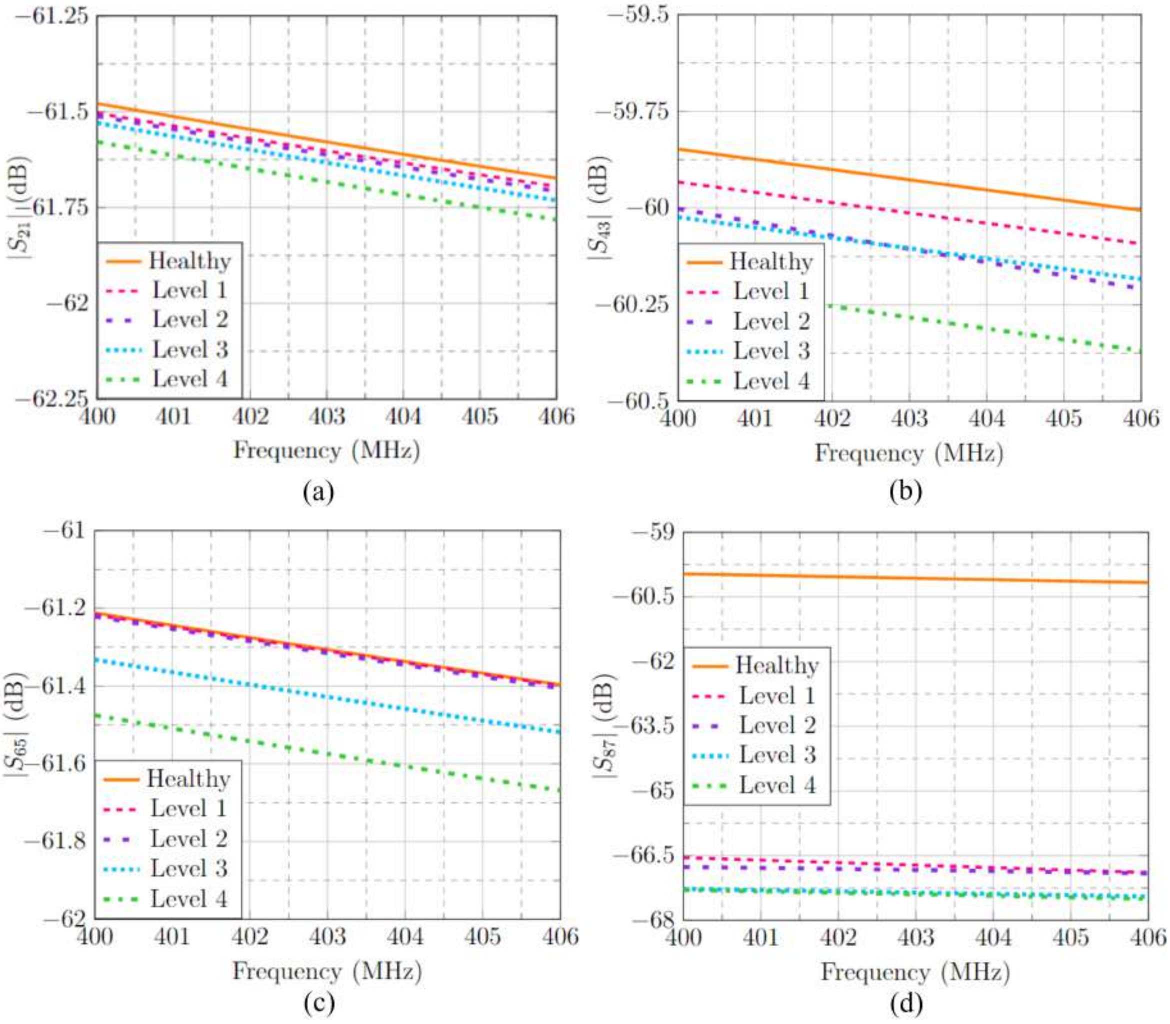

Figure 3.11. Transmission coefficient plots of directly facing anterior and posterior antennas when different levels of edema are introduced to lower right lobe: (a) $|S_{21}|$ (b) $|S_{43}|$ (c) $|S_{65}|$ (d) $|S_{87}|$.

4. MEASUREMENTS AND RESULTS

In this chapter, all measurement steps and results are presented in detail, along with a comprehensive analysis. The fabrication process of the measurement setup and its associated steps are elaborated upon in Section 4.1. Subsequently, required phantoms and their realization steps are provided in Section 4.2. This part is followed by Section 4.3 where the PE condition and its severity analysis are observed experimentally. Finally, measurements conducted during respiration on the human body are illustrated in Section 4.4 in order to demonstrate that the dynamic changes in the dielectric properties of lungs and the channel distances could be observed with the proposed loop antenna.

4.1. Fabrication of the Measurement Setup

4.1.1. Reduction of the Simplified Setup

In the ANSYS HFSS simulation, shown in Figure 3.4, the entire upper body excluding the arms and head is modelled, resulting in a total size of 36 cm × 26 cm × 30 cm. If a plexiglass rectangular box were to be realized based on these dimensions, it would require approximately 30 litres of phantom for measurements. Therefore, we decided to reduce the setup so that only one lung is analyzed as illustrated in Figure 4.1. Two antennas covering the upper left lobe are kept in order to realize the PE scenario and an additional posterior antenna facing the lower left lobe is placed for deeper analysis. Furthermore, it is important to check that the antennas are still operational and there is no surface wave propagating around the phantom that will change the transmission coefficient. This analysis is given in Figure 4.2. Approximately -30 dB of reflection coefficient values of antennas demonstrate that the proposed antenna is operational in the reduced model. Additionally, differences between transmission coefficients, $|S_{21}|$ and $|S_{31}|$, in reduced and initial models are less than 0.5 dB, proving that there is no surface wave propagation around the muscle phantom.

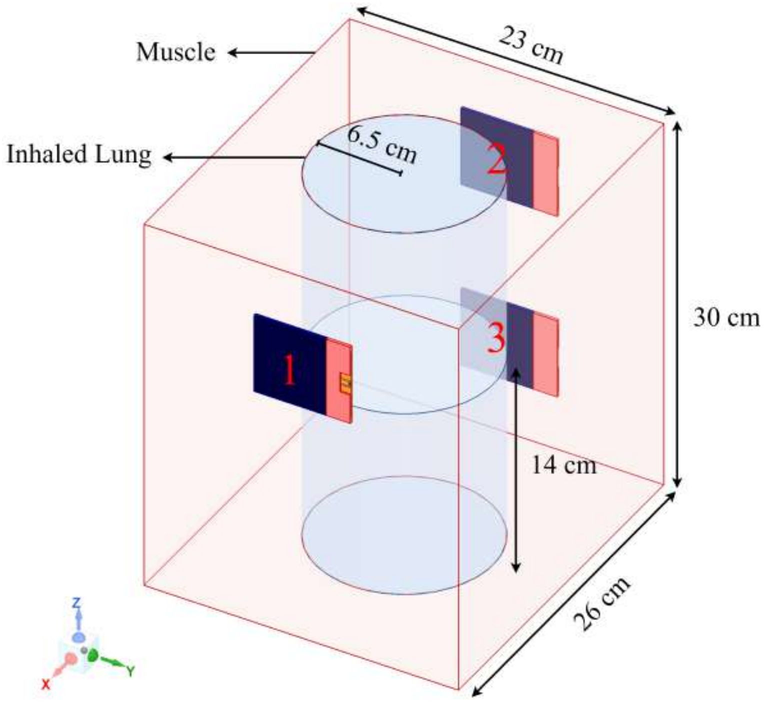

Figure 4.1. The reduced simplified setup: Three antennas, one on the anterior and two on the posterior torso, covering one lung.

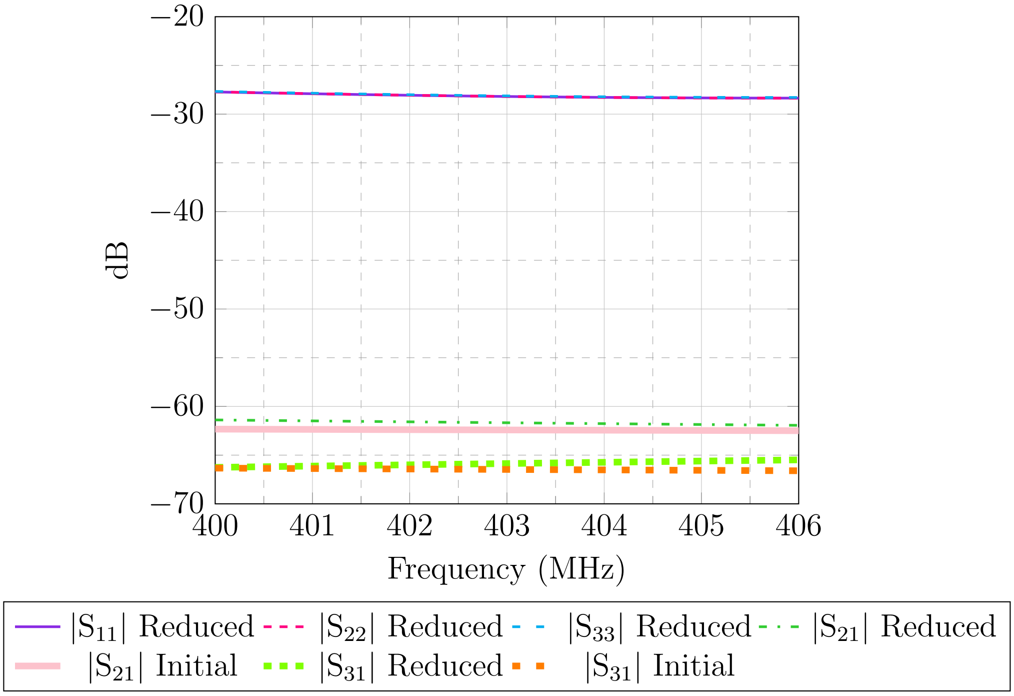

Figure 4.2. Reflection coefficients of the antennas in the reduced model and transmission coefficient comparison between the reduced and initial simplified models.

4.1.2. Realized Measurement Setup

In Figure 4.3, the HFSS model of the envisaged measurement setup is illustrated. The muscle phantom is poured into a rectangular plexiglass box and the lung is represented by cylinders filled with lung phantom. Antennas are positioned directly on the muscle phantom through the windows on the plexiglass and their positions are maintained using antenna holders. The hollow cylinders, aligner supports, and antenna holders are produced using "Clear" resin via an SLA 3D printer.

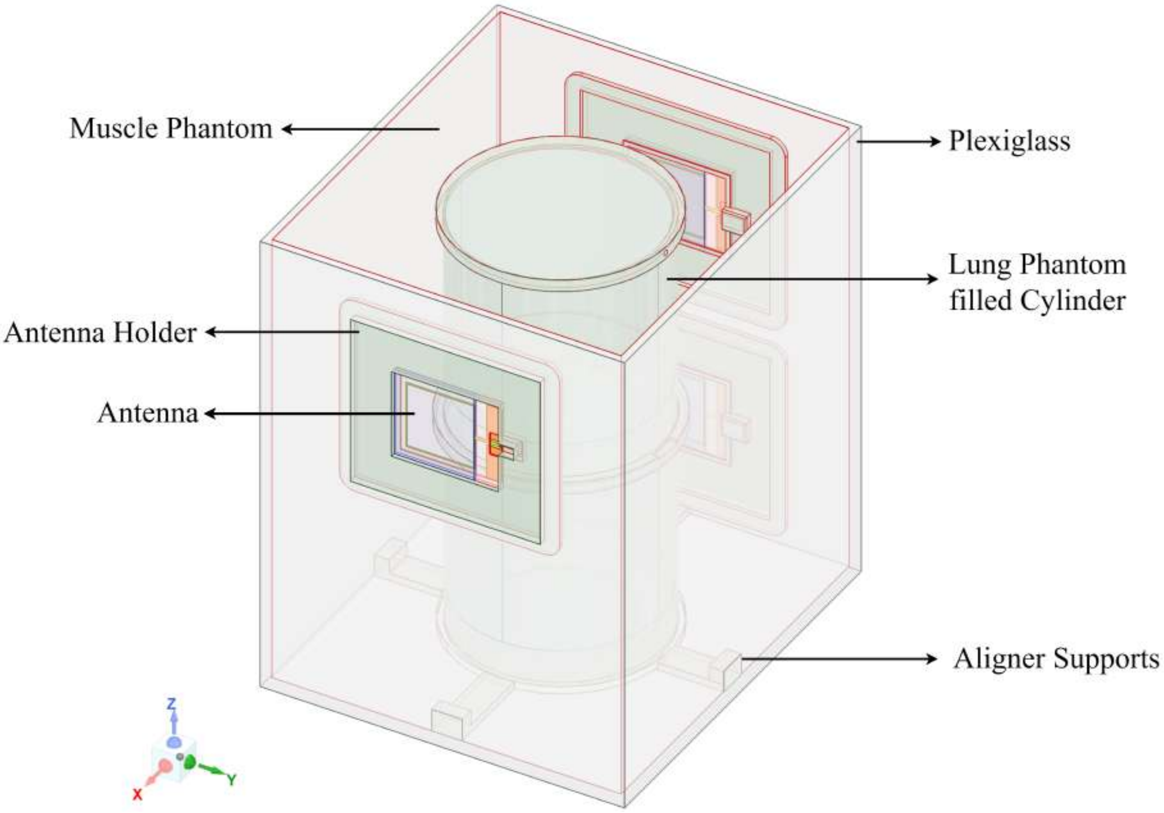

Figure 4.3. The simulation model for the realized setup including plexiglass and cured clear materials.

Here, it is essential to check whether the inclusion of cured clear resin affects the expected results. Therefore, another simulation is conducted by assigning frequency-dependent dielectric properties to the cured clear material. Figure 4.4 shows the results of this validation simulation. With less than -25 dB of reflection coefficients, it is clear that the addition of antenna holders does not alter the resonant frequency or deteriorate the matching. Moreover, transmission coefficients between the anterior and posterior antennas remain stable within a 1 dB range, confirming that the addition of clear materials does not significantly impact the transmission. Finally, the measurement setup is fabricated based on these validation results and it is shown in Figure 4.5.

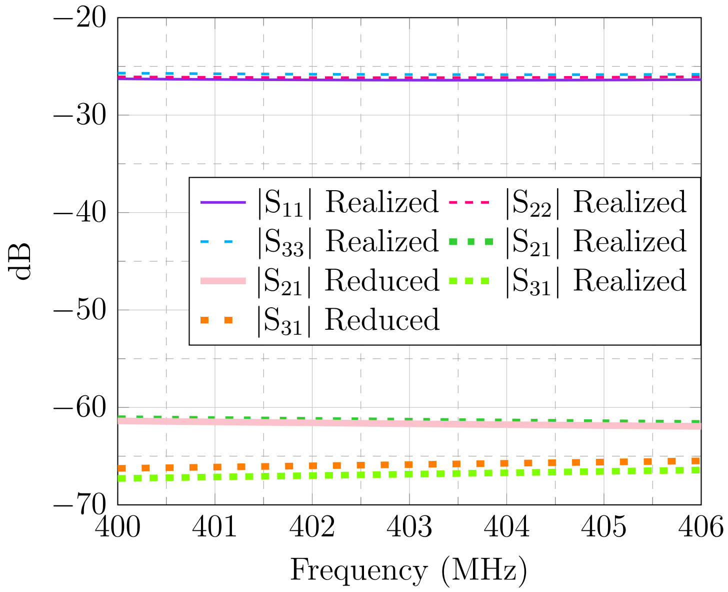

Figure 4.4. The reflection and transmission coefficient comparison between the reduced model and the realized model.

4.2. Phantom Production

4.2.1. Definition of Phantoms

In previous chapters, it is mentioned that the human body poses challenges to electromagnetic radiation due to its high relative permittivity and conductivity values. As a result, when developing antennas or other microwave devices that operate close to the body, it's crucial to consider these factors [99]. However, it's not always feasible to design or test devices directly on or inside the human body. This is where ”phantoms” come into play. These are materials engineered to mimic the dielectric properties of the human body [100]. By using phantoms, one can simulate the interactions between electromagnetic fields and the body in a controlled and safe manner for experimentation and testing purposes. Therefore, phantoms play a crucial role in measurement setups, ensuring an accurate assessment of antenna parameters when considering human body proximity [101].

Figure 4.5. The fabricated measurement setup with the antennas.

Phantoms are categorized in various ways in the literature, depending on their characteristics. Some common approaches include classification based on their final forms, main substances, or the part of the body they replicate. In terms of final forms, phantoms can be classified as solid phanto [102], semi-solid phantoms [103], and liquid phantoms [104]. Alternatively, they can be categorized by their main substances, such as water-based phantoms [104], oil-in-gelatine phantoms [105], Triton X100 phantoms [106], and 3D printed phantoms [107]. Lastly, phantoms can also be classified based on the body part they mimic, such as head phantoms [103], hip phantoms [104], and breast phantoms [108].

4.2.2. Fabricating Human Lung Phantom and Human Muscle Phantom

In this work, tissue-mimicking mixtures are water-based, liquid phantoms prepared using distilled water, sugar, salt, glycerol and sodium azide (NaN_3). While the muscle, edema level 2, edema level 4 phantoms are produced with distilled water, sugar, salt, and sodium azide, the healthy lung phantom is prepared by using only distilled water and glycerol. Due to the low permittivity and conductivity values of healthy lungs compared to the others, target dielectric values, 23.7 of permittivity and 0.375 of conductivity, are not achievable with a water-sugar mixture. The quantity of each ingredient to fill the hollow cylinders and plexiglass shown in Figure 4.5 is listed in Table 4.1.

Table 4.1. The quantity of each ingredient required for the human muscle, healthy lung, edema level 2, edema level 4 phantoms.

	Muscle	**Healthy Lung**	**Edema 2**	**Edema 4**
Distilled Water	13.2 L	1.95 L	2.6 L	2.5 L
Sugar	12 kg	-	2.7 kg	750 gr
Salt	360 gr	-	180 gr	60 gr
Glycerol	-	4 L	-	-
Sodium Azide	10 gr	-	5 gr	5 gr

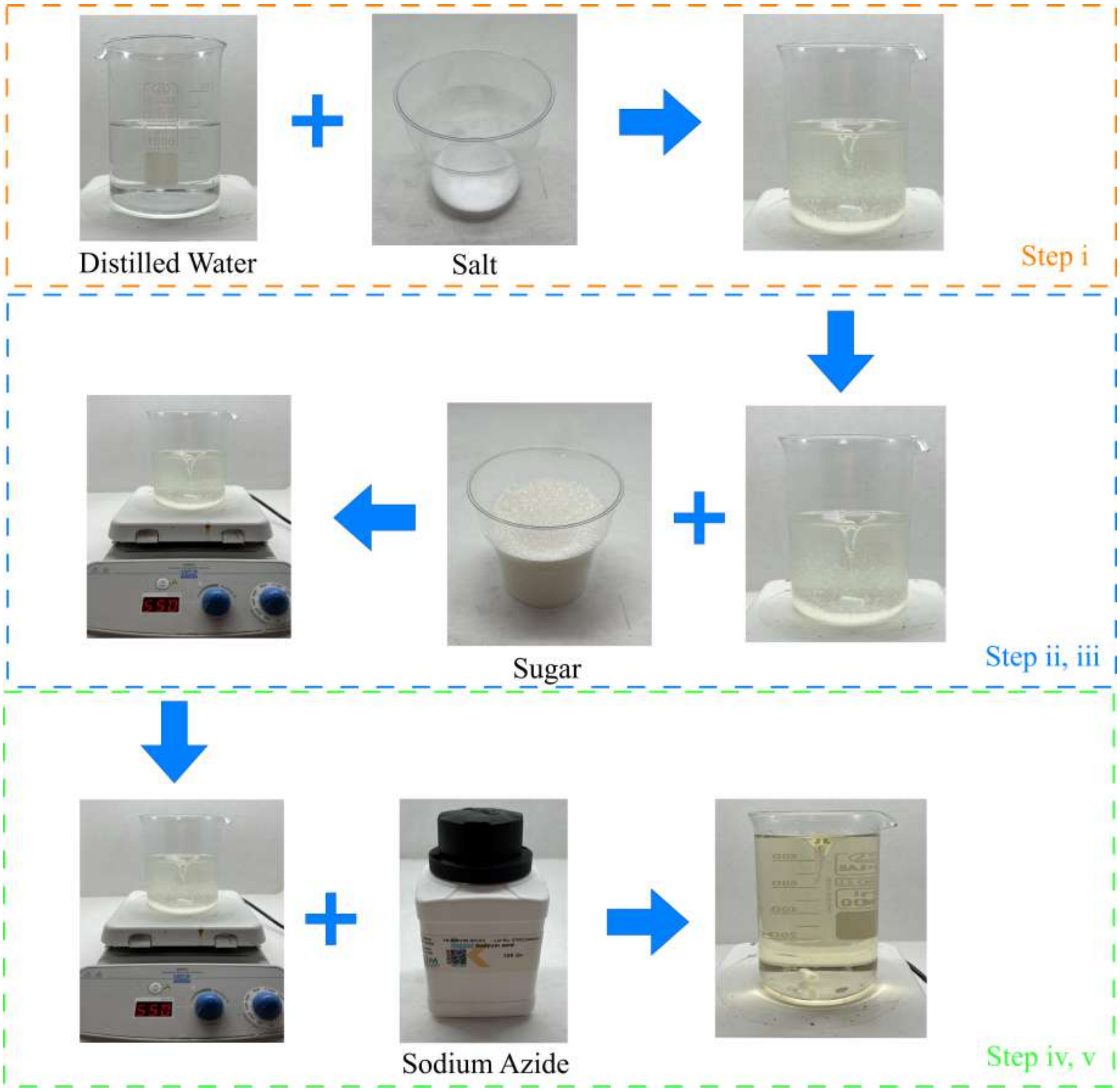

Figure 4.6. Fabrication process of phantoms including sugar and salt.

The procedure to be followed for the fabrication of muscle, edema level 2 and edema level 4 phantoms is as follows:

(i) Salt is added to water, and the mixture is stirred until the salt completely dissolves.
(ii) Sugar is slowly added to the mixture while it is being heated.
(iii) Once all the sugar is added, the mixture is heated and stirred until all the sugar dissolves completely.
(iv) Sodium azide is added to the mixture to prevent spoilage.

(v) The phantom is allowed to cool at room temperature while it is stirred.

The procedure to be followed for the fabrication of the healthy lung phantom is simpler than other phantoms due to its ingredients. The phantom is made by mixing distilled water with glycerol and stirring the mixture until it is completely uniform.

The given fabrication process is illustrated in Figure 4.6. Due to the high permittivity value of distilled water, it is the main source of permittivity in the mixture. Sugar is utilized to lower the overall permittivity, allowing for control over the final value. Also, salt is the source of conductivity and it is used to control the final conductivity value. Finally, sodium azide is included for preservation. In the healthy lung phantom, glycerol serves two important functions. It helps to lower the permittivity of the mixture while also regulating its conductivity.

4.2.3. Measurement of the Dielectric Properties

Before using the fabricated phantoms in the measurement setup directly, their dielectric properties must be measured in order to validate that the target relative permittivity and conductivity values are reached. The dielectric properties of these phantoms are measured by using Speag's DAK 3.5 dielectric measurement kit as shown in Figure 4.7.

The dielectric property measurements conducted with Speag's DAK 3.5 rely on the open-ended coaxial probe method. Briefly, the open-ended coaxial is a cut-off section of the 50Ω transmission line. The dielectric properties of the phantom are determined by measuring the change in reflection coefficient at the points where the probe makes contact with the phantom. The formulations and theoretical analysis of the open-ended coaxial probe method are explained in detail in [109]. Finally, the measured dielectric properties of each phantom are depicted in Figure 4.8. Also, the real and computed values at 400 MHz are tabulated in Table 4.2.

Figure 4.7. Relative permittivity and conductivity measurement of phantoms with Speag's DAK 3.5 dielectric measurement kit.

Table 4.2. Real and computed relative permittivity(ϵ_r) and conductivity(σ) values of phantoms at 400 MHz and their percent errors.

	Real Value		**Computed Value**		**Percent Error**	
Phantom	$\boldsymbol{\epsilon_r}$	$\boldsymbol{\sigma}$ **(S/m)**	$\boldsymbol{\epsilon_r}$	$\boldsymbol{\sigma}$ **(S/m)**	$\boldsymbol{\epsilon_r}$	$\boldsymbol{\sigma}$
Muscle	57.10	0.790	57.98	0.708	1.54%	10.3%
Healthy Lung	23.80	0.375	24.30	0.395	2.1%	5.3%
Edema 2	47.0	1.08	46.8	0.85	0.43%	20.4%
Edema 4	70.20	1.80	71.94	1.76	2.47%	2.23%

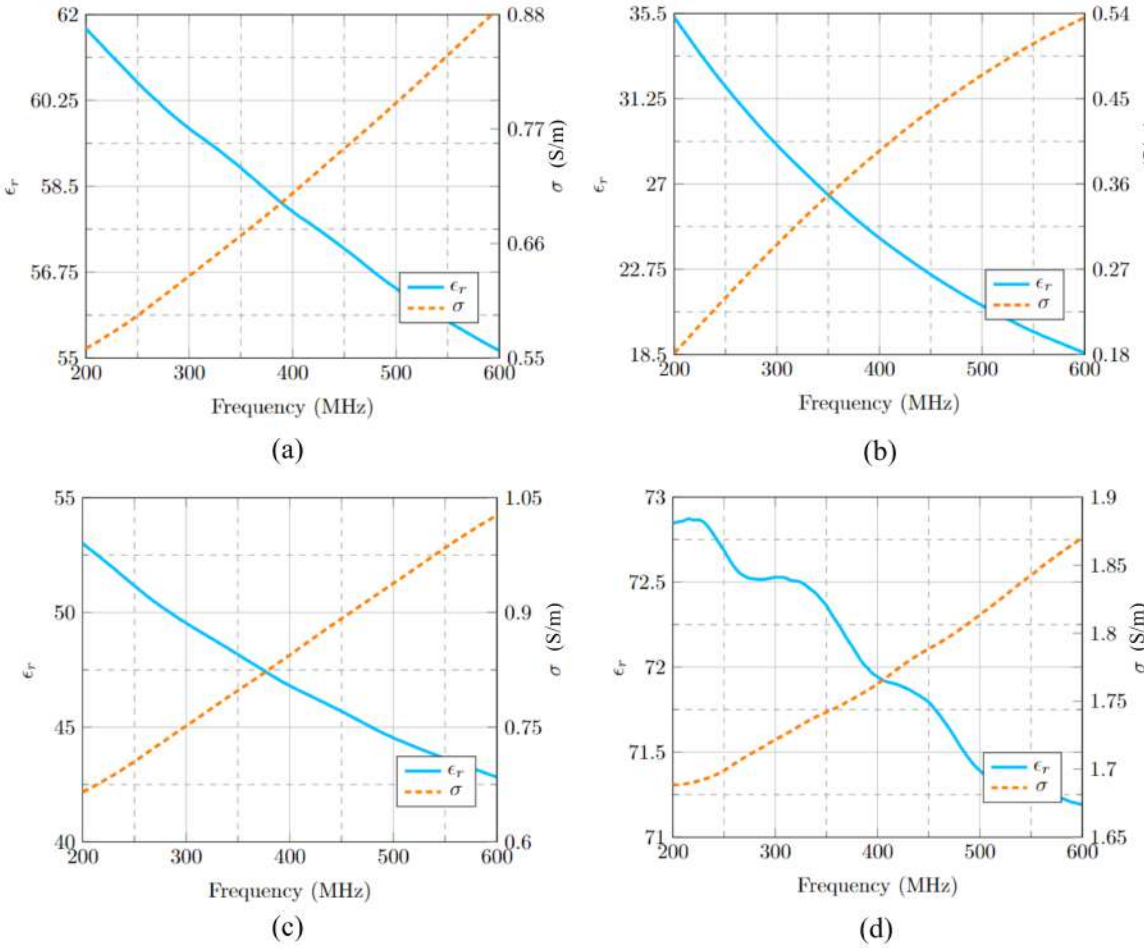

Figure 4.8. Frequency dependent relative permittivity(ϵ_r) and conductivity(σ) plots of fabricated phantoms: (a) Muscle (b) Healthy Lung (c) Edema Level 2 (d) Edema Level 4

4.3. Measurement Results on Realized Phantoms

After completing the fabrication of phantoms and measurement setup, the phantoms are poured into the cylinders and plexiglass, as illustrated in Figure 4.9. Additionally, Figure 4.10 depicts the measurement setup filled with muscle phantom and connected to the VNA.

The reflection coefficient analysis of three antennas is presented in Figure 4.11 in order to validate that these antennas are operating within the desired frequency band. According to the measurement results, all antennas exhibit a reflection coefficient of less than −16 dB, indicating that the antennas are operational in the MICS band.

Figure 4.12 presents both the localization and severity analysis of PE. In the simulation results, it's observed that the transmission coefficient between directly facing antennas consistently decreases regardless of the PE location due to increased conductivity. However, this decrease is more apparent between antennas covering the affected lobe. For instance, when the lower lobe is assigned to be PE, $|S_{21}|$ decreases by approximately 2 dB as in Figure 4.12(b). Nevertheless, the drop in $|S_{21}|$ is around 4.5 dB in the case of PE in the upper lobe as in Figure 4.12(a), indicating the location of PE.

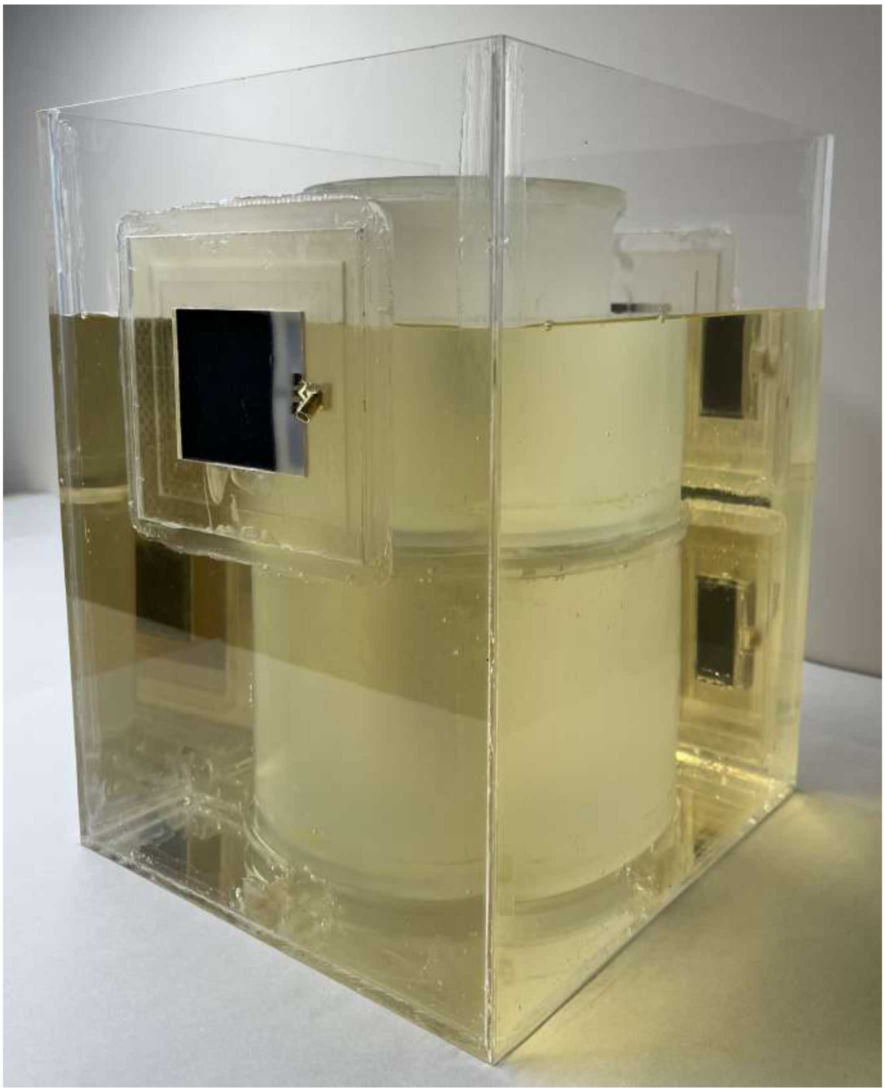

Figure 4.9. The measurement setup is being filled with muscle phantom.

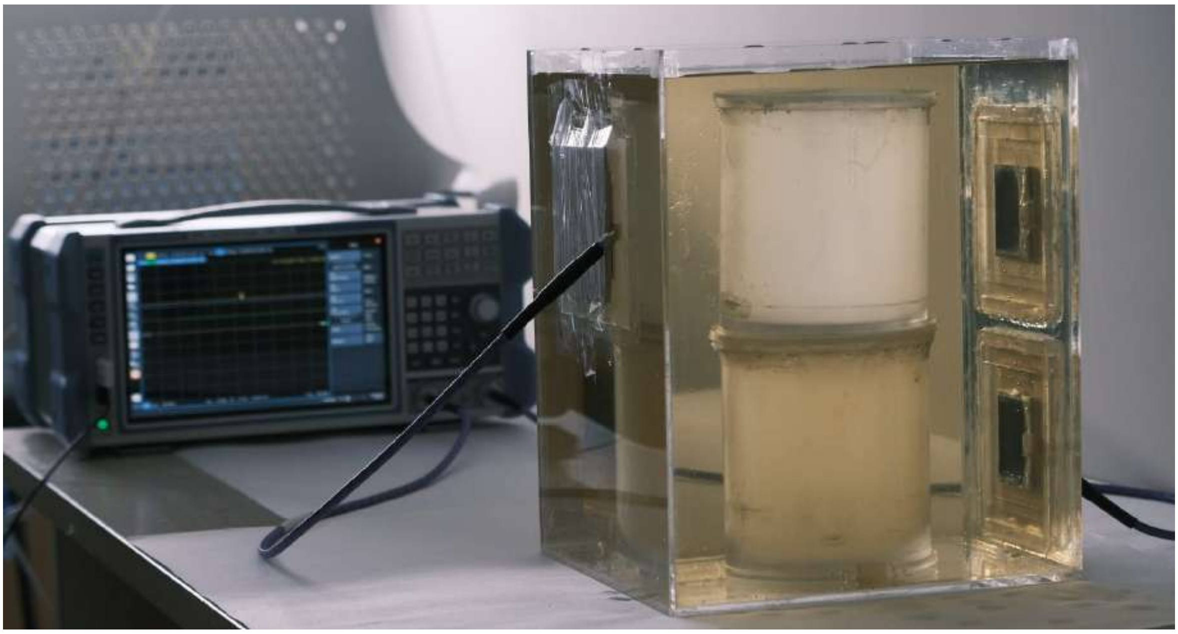

Figure 4.10. The measurement setup is filled with muscle phantom and connected to the VNA.

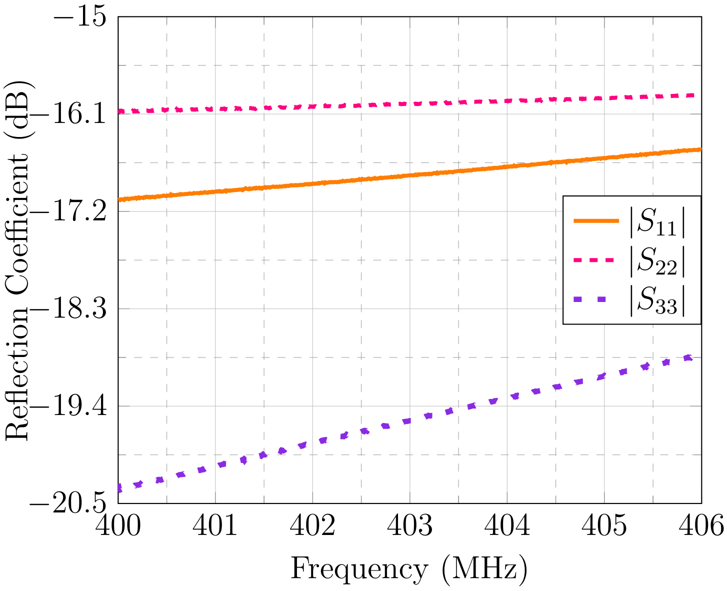

Figure 4.11. The reflection coefficient analysis of three fabricated antennas.

Moreover, it is expected to observe varying $|S_{21}|$ levels as the different lung phantoms are placed in the upper lobe. As found in the simulation result depicted in Figure 3.11(d), $|S_{21}|$ shows a significant change from healthy to edema level 2, unlike other severity levels. Similar results are observed in Figure 4.12(a). Even though the change in the transmission coefficient from edema level 2 to edema level 4 is small, two different phantoms have distinguishable $|S_{21}|$ levels, indicating that the severity analysis with the fabricated antenna is possible.

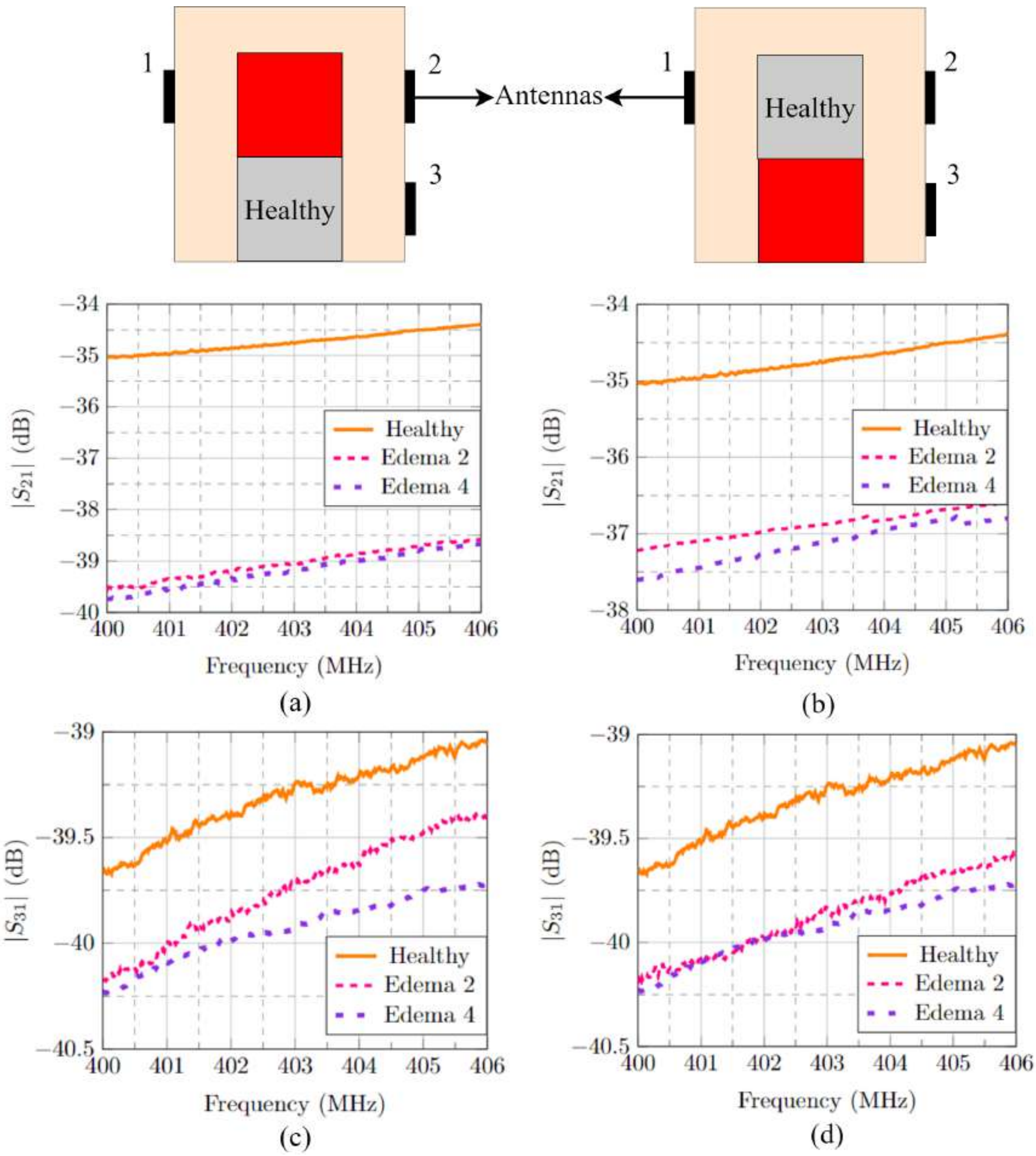

Figure 4.12. Transmission coefficient analysis for different edema levels and locations. The location of the varying lobe is given at the top of the plots. (a) Upper Lobe $|S_{21}|$ (b) Lower Lobe $|S_{21}|$ (c) Upper Lobe $|S_{31}|$ (d) Lower Lobe $|S_{31}|$.

Additionally, Figure 4.12(c) and (d) show the transmission coefficient in the cross channel. As anticipated, the transmission coefficients in these channels, for the same edema levels, are lower than those in the direct channels due to the increased channel distance. Also, increasing edema levels reduces the transmission coefficient in this channel due to the increased conductivity similar to the direct channels. However, the decrease in transmission coefficient is less than 1 dB as depicted in Figure 4.12(d). This suggests that relying solely on cross-channel analysis is insufficient for detecting and monitoring PE.

Although the change in the measured transmission coefficients closely follows the trends observed in simulation results, the measured values of the transmission coefficients are approximately 30 dB higher than the simulated values. This discrepancy might be attributed to two reasons. Firstly, despite efforts to minimize reflections from surrounding materials, undesired reflections may have occurred due to the large wavelength. Secondly, propagating surface waves may have contributed to the discrepancy. Although surface waves are not observed in simulation results depicted in Figure 4.2, fabrication-related issues of antenna, setup, or phantoms could have caused their occurrence, leading to an increase in transmission coefficients.

4.4. Measurement Results on Human Body

At the beginning of this project, an application was made to obtain the permission of the ethics committee for on-body measurements. The application was approved by the Sciences and Engineering Fields Human Research Ethics Committee(FMİNAREK) with the document number of 52247 on 17.02.2022. Therefore, another group of measurements was conducted on the author and two other voluntary researchers from our laboratory. Since these are not clinical experiments, the measurement results belong to healthy people. However, these measurements are aimed at tracking the tidal respiration process.

It should be emphasized that both the dielectric properties of the lung tissue and the channel distances between the antennas change during respiration. The dielectric properties of deflated and inflated lung tissues for a healthy person are given in Table

1.1. The inflated lung tissue has a relative permittivity of 23.8 and conductivity of 0.375, whereas, these values increase to 54.5 and 0.684, respectively, for deflated lung tissue.

Therefore, it is anticipated that monitoring tidal respiration with the proposed antenna aids the claim of monitoring PE. In this section, detailed information regarding the experiment and measurement results are given one by one for each subject and a common discussion about the results is given at the end.

4.4.1. Subject A

Table 4.3 provides the physical characteristics and distance information between the antennas for subject A. The distance between the antennas is measured using a ”U ruler” and is taken as the average of fully inhaled and fully exhaled values. Antenna 1, 2, and 3 correspond to the upper anterior, upper posterior, and lower posterior, respectively. These antennas are positioned on the body to cover the lung, with the anterior and posterior antennas aligned with the U ruler as shown in Figure 4.13.

Table 4.3. The physical characteristics and the distance information between the antennas of subject A.

Subject A	**Values**
Height	178 cm
Weight	80.2 kg
Dist. btw. 1-2	21.5 cm
Dist. btw. 1-3	23.8 cm

Measurements are conducted while the subject is seated at a fixed position, maintaining a constant distance from the VNA as illustrated in Figure 4.14. The measured reflection coefficient values of each antenna are presented in Figure 4.15. Finally, the measured transmission coefficients between the direct and cross channels at 403 MHz are depicted in Figure 4.16.

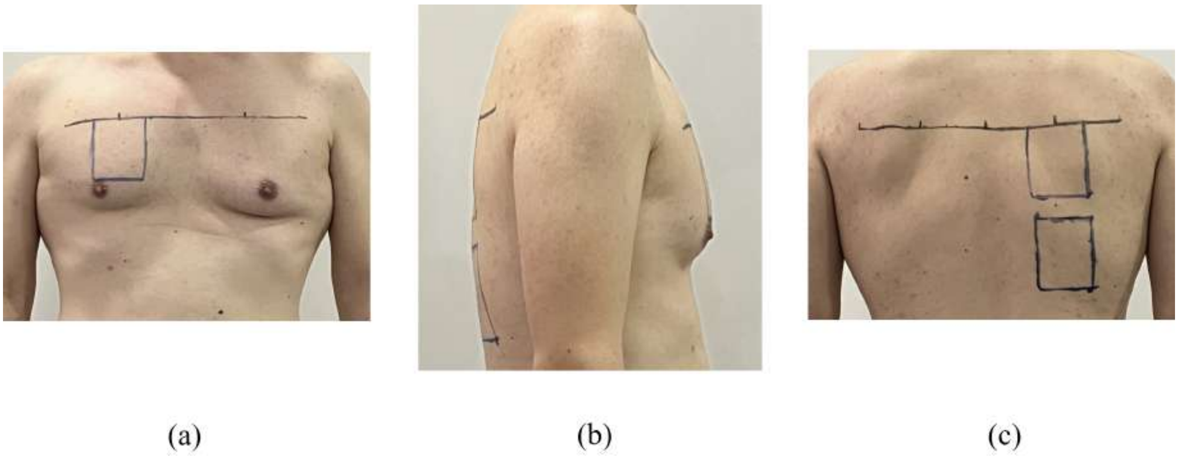

Figure 4.13. Antenna locations on subject A. (a) Front view (b) Side view (c) Back view.

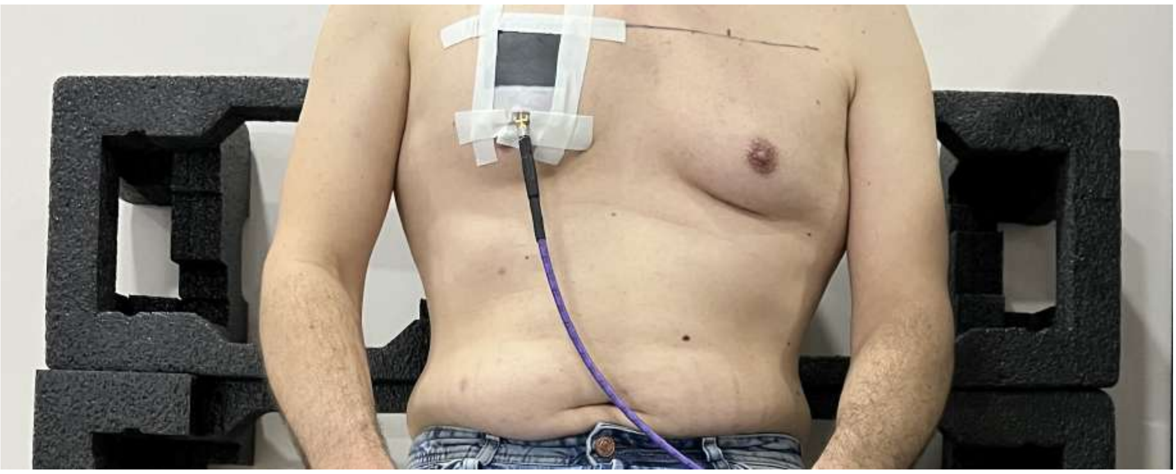

Figure 4.14. On-body measurements on subject A.

4.4.2. Subject B

Table 4.4 provides the physical characteristics and distance information between the antennas for subject B. The distance between the antennas is measured using a ”U ruler” and is taken as the average of fully inhaled and fully exhaled values. Similar to subject A, antennas are positioned on the body to cover the lung, with the anterior and posterior antennas aligned with the U ruler as shown in Figure 4.17.

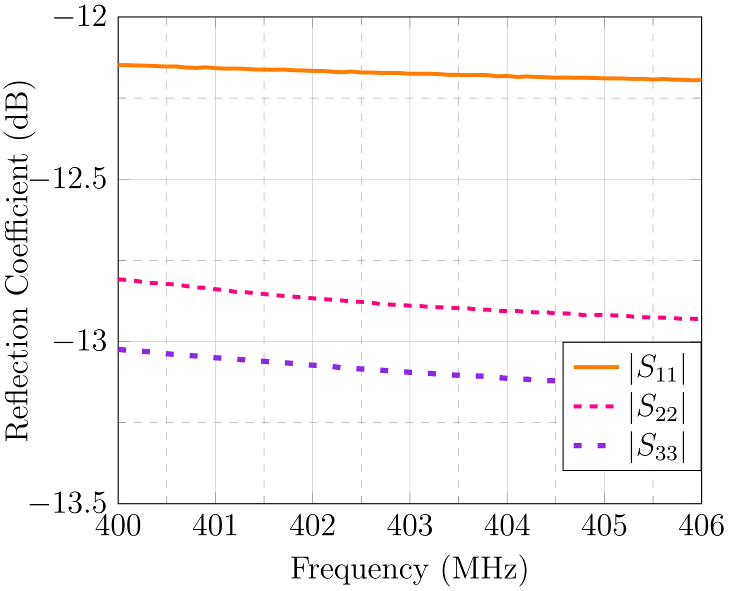

Figure 4.15. Reflection coefficients of all antennas on subject A.

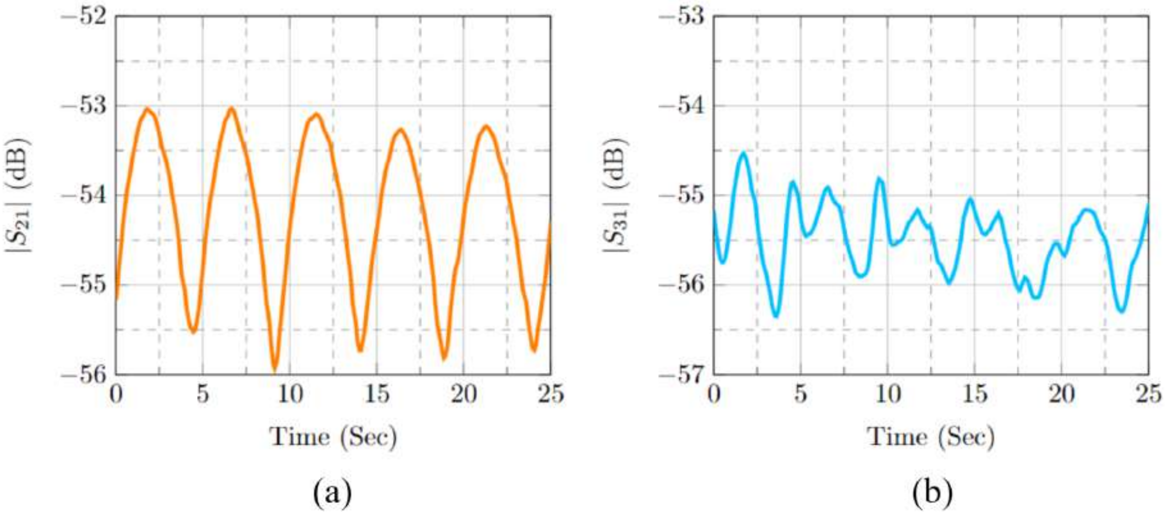

Figure 4.16. The transmission coefficient analysis at 403 MHz on subject A during respiration. (a) $|S_{21}|$ (b) $|S_{31}|$.

Measurements are conducted while the subject is seated at a fixed position, maintaining a constant distance from the VNA as illustrated in Figure 4.18. The measured reflection coefficient values of each antenna are presented in Figure 4.19. Additionally, the measured transmission coefficients between the direct and cross channels at 403 MHz are depicted in Figure 4.20.

Table 4.4. The physical characteristics and the distance information between the antennas of subject B.

Subject B	Values
Height	183 cm
Weight	98.6 kg
Dist. btw. 1-2	24 cm
Dist. btw. 1-3	26.6 cm

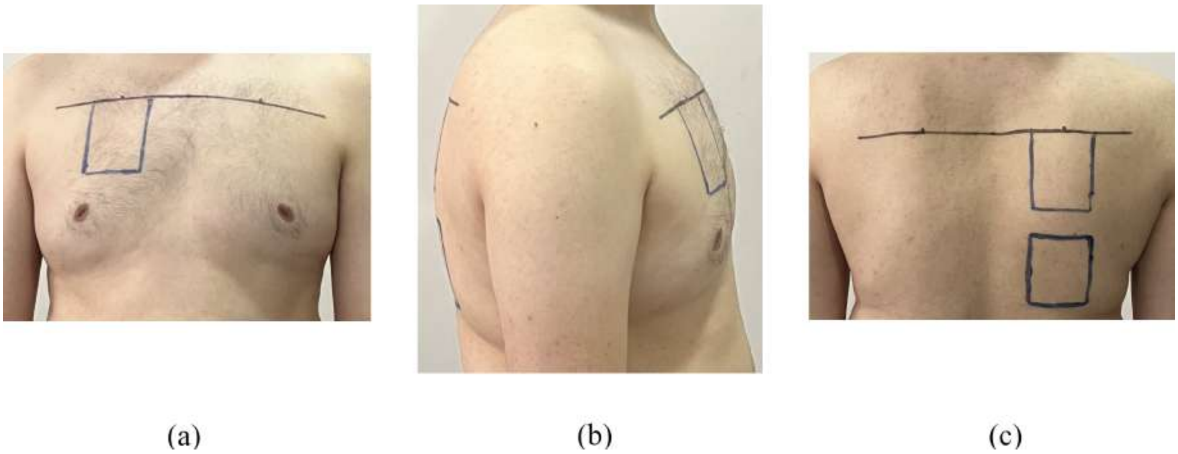

Figure 4.17. Antenna locations on subject B. (a) Front view (b) Side view (c) Back view.

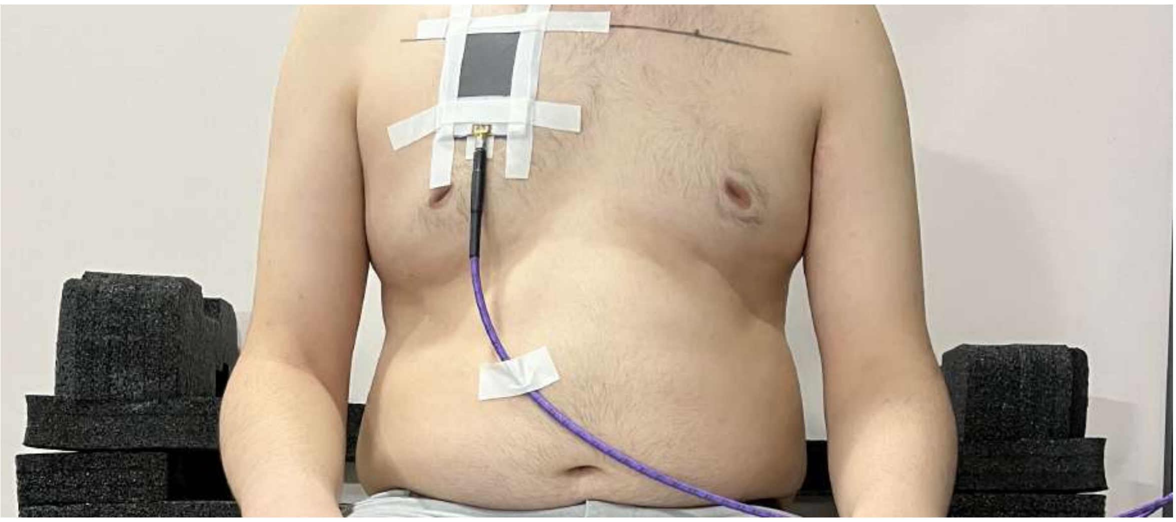

Figure 4.18. On-body measurements on subject B.

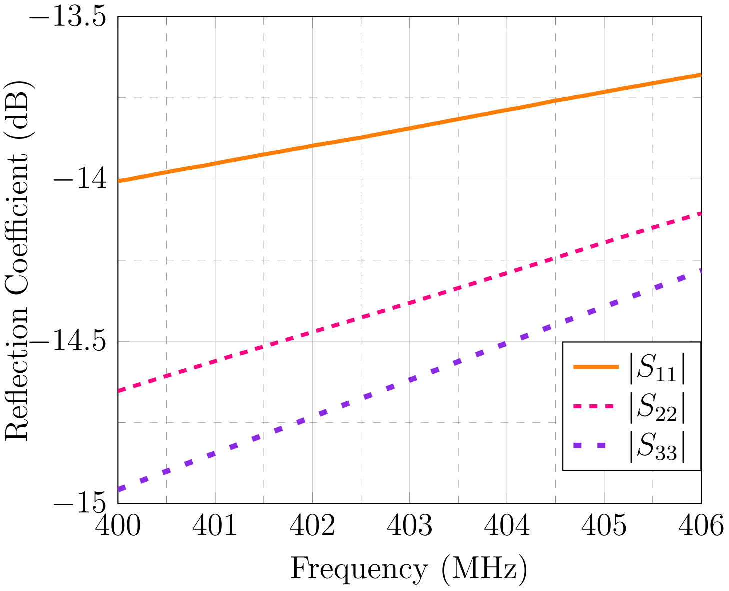

Figure 4.19. Reflection coefficients of all antennas on subject B.

4.4.3. Subject C

Table 4.5 provides the physical characteristics and distance information between the antennas for subject C. The distance between the antennas is measured using a ”U ruler” and is taken as the average of fully inhaled and fully exhaled values. Similar to subjects A and B, antennas are positioned on the body to cover the lung, with the anterior and posterior antennas aligned with the U ruler as shown in Figure 4.21.

Table 4.5. The physical characteristics and the distance information between the antennas of subject C.

Subject C	**Values**
Height	190 cm
Weight	110 kg
Dist. btw. 1-2	26.3 cm
Dist. btw. 1-3	28 cm

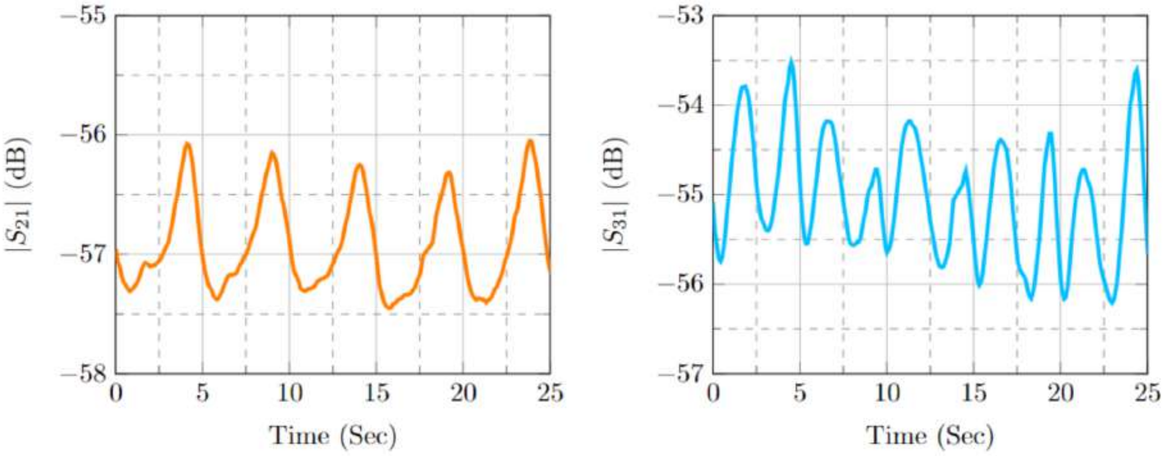

(a) (b)

Figure 4.20. The transmission coefficient analysis at 403 MHz on subject B during respiration. (a) $|S_{21}|$ (b) $|S_{31}|$.

(a) (b) (c)

Figure 4.21. Antenna locations on subject C. (a) Front view (b) Side view (c) Back view.

Measurements are conducted while the subject is seated at a fixed position, maintaining a constant distance from the VNA as illustrated in Figure 4.22. The measured reflection coefficient values of each antenna are presented in Figure 4.23. Also, the measured transmission coefficients between the direct and cross channels at 403 MHz are depicted in Figure 4.24.

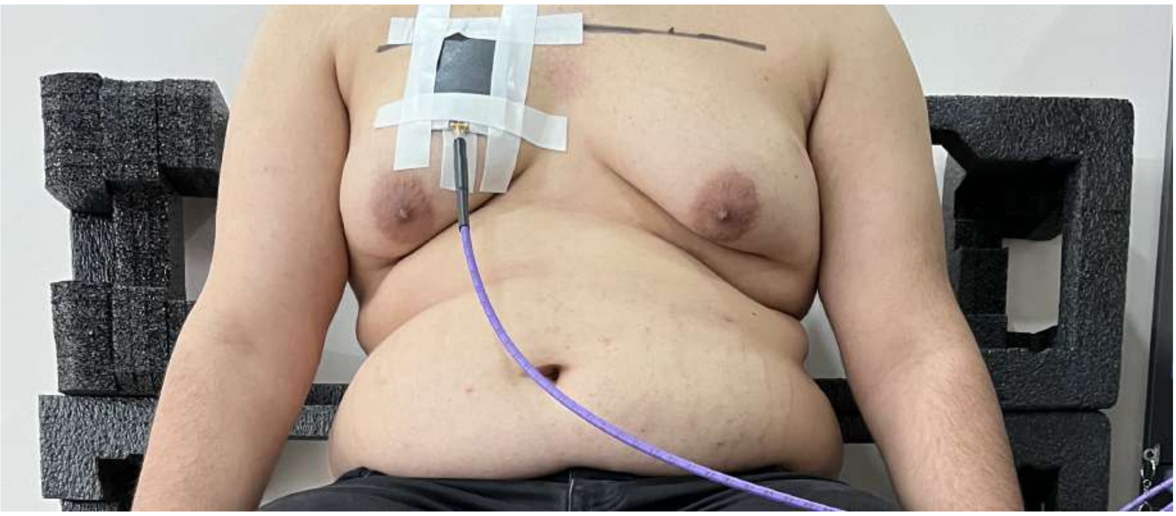

Figure 4.22. On body measurements on subject C.

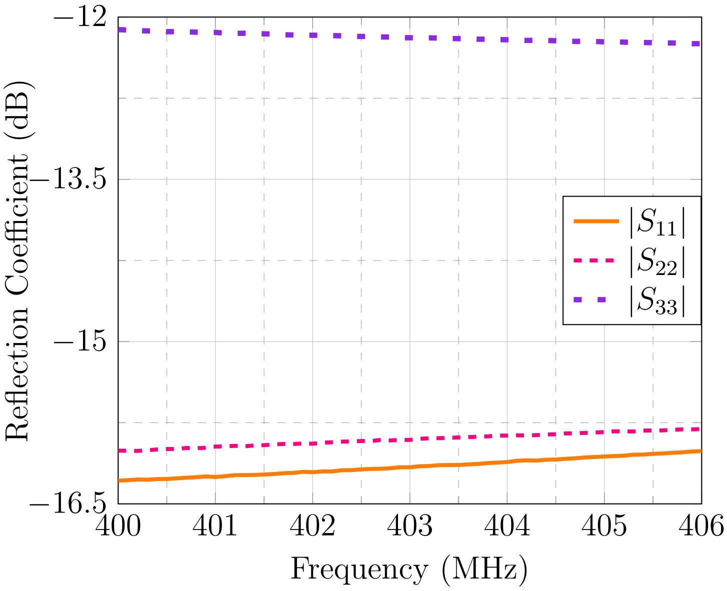

Figure 4.23. Reflection coefficients of all antennas on subject C.

4.4.4. Discussion

The measured reflection coefficient plots presented in Figures 4.15, 4.19, and 4.23 confirm that the antennas are operational on each subject. It is noticed that the reflection coefficient values of antennas not only vary among subjects but also, depend on the location where the antennas are placed on the body. It is known that the body composition of each person is different from each other. Hence, it is expected to observe different reflection coefficients for each subject. The variations in reflection coefficients among antennas on the same subject might be explained by the conformability analysis provided in Figure 2.15. As demonstrated in this figure, slight variations may occur in both the reflection coefficient and the resonant frequency as the bending of the antenna changes. Hence, the observed differences in reflection coefficients of the antennas on the same subject might be attributed to this phenomenon. Despite this difference, it is also shown that the antennas are operational in the MICS band and the transmission analysis could be conducted.

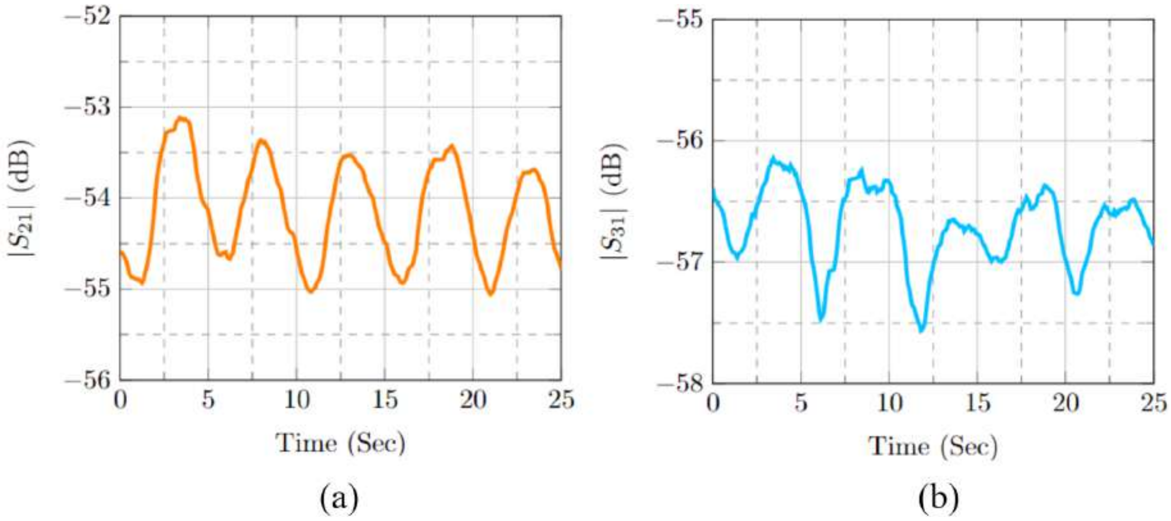

Figure 4.24. The transmission coefficient analysis at 403 MHz on subject C during respiration. (a) $|S_{21}|$ (b) $|S_{31}|$.

The transmission coefficient analysis plots at 403 MHz for each subject are depicted in Figures 4.16, 4.20, and 4.24. In order to conduct these measurements, a 24-BPM metronome and a MATLAB code are employed to automate the running and saving of measurements on the VNA. The 24-BPM metronome ensures that each breathing cycle lasts for 5 seconds, with inhalation and exhalation each lasting 2.5 seconds. During the measurements, the subjects synchronize their breathing with the metronome, allowing for the estimation at which second the subjects breathe in and out from the measurement results. Also, a transmission coefficient at one frequency point is analyzed to observe dynamic changes. Hence, 403 MHz which is the center frequency of the MICS band is chosen for the respiration analysis.

During exhalation, the distance between the antennas decreases. Additionally, the relative permittivity of the lung tissue increases and becomes closer to the relative permittivity of the muscle tissue, resulting in a reduction of reflections at the tissue boundaries. Therefore, it is expected to observe an increase in transmission coefficients during exhalation and a decrease during inhalation. In order to verify this hypothesis, measurements on subject A are started during exhalation, while those on subjects B and C are started during inhalation. As presented in Figure 4.16(a), the $|S_{21}|$ increases for approximately 2.5 seconds and then decreases about the same amount for another 2.5 seconds during subject A's respiration cycle. On the other hand, subjects B and C, starting their measurements during inhalation, exhibit the opposite trend: The $|S_{21}|$ levels decrease in the first half of the respiration cycle and increase in the latter half as shown in Figures 4.20(a) and 4.24(a). Thus, it is shown that the changing trends in $|S_{21}|$ across all subjects align with the expectations.

In addition to the transmission coefficients in direct channels, the measurements in cross channels are illustrated in Figures 4.16(b), 4.20(b), and 4.24(b). Unlike the expected pattern observed in direct channels, the measured transmission coefficients in cross channels, denoted as $|S_{31}|$, do not follow a consistent trend similar to $|S_{21}|$. This discrepancy could be attributed to the increased distance between antennas, leading to heightened exposure to noise and resulting in significant deviations in $|S_{31}|$ values. Therefore, it is deduced that analyzing cross channels alone is insufficient for the detection and monitoring of PE, which aligns with the inference in the measurements conducted with realized phantoms.

Finally, the measured transmission coefficient values in both direct and cross channels are consistently below 52 dB, closer to the simulated values compared to those obtained from phantom measurements. This variance from the simulation could be reasoned by similar factors such as undesired reflections and surface waves, as mentioned in phantom measurements. Despite the variation from simulated values, the trend of change in the transmission coefficient remains consistent across all results. This consistency demonstrates the capability of the proposed on-body flexible antenna for detecting and monitoring PE.

5. CONCLUSION

PE presents a significant health concern and it is the most common indication of almost all pulmonary disorders. Hence, early detection and continuous monitoring are critical for effective management and treatment. Therefore, various approaches including WBAN systems have been proposed especially in the last decade. In this thesis, we have explored the feasibility of utilizing on-body wearable flexible antennas for the detection and monitoring of PE.

First of all, the antenna proposed in this thesis is a coplanar waveguide loop antenna designed to operate within the MICS band. It is fabricated on a novel HPFS which has a relative permittivity value of 11.44 and a loss tangent value of 0.021 at 405 MHz. By utilizing this HPFS, it is aimed to achieve both the desired miniaturization and user acceptance. The high permittivity facilitates miniaturization, while the flexible and conformable nature of the substrate ensures user acceptance and practicality. With the design and fabrication of the proposed antenna, the detection and monitoring of PE are analyzed in both numeric and realized models.

In the numeric model, localization and severity of PE are analyzed. Localization analysis is achieved by examining the transmission coefficients in the direct channels between the antennas, while the severity analysis is conducted by monitoring the decrease in the transmission coefficient. The dielectric properties of lung-representing cylinders are assigned to be healthy lung and PE with different edema levels for these analyses. In the simulation results of the numeric model, it is demonstrated that the proposed antenna can be used in the localization and severity analysis of PE.

After completing the numeric analysis and fabricating the antenna, the tissue-mimicking phantoms representing muscle tissue, healthy lung, edema level 2, and edema level 4 phantoms are prepared. These phantoms are used to evaluate the performance of the proposed on-body antenna. Our measurements with these phantoms demonstrate that PE localization can be achieved by analyzing the direct channels between antennas. Additionally, it is observed that increased relative permittivity and conductivity of the lung result in a noticeable deterioration of the transmission coefficient, enabling the severity analysis of PE. These findings highlight the utility of the proposed antenna for both localizing and assessing the severity of PE.

Finally, another series of measurements are conducted on the human body in order to analyze the antenna performance on different body compositions. These measurements involve the author and two other volunteers and the data are collected during respiration cycles. It is anticipated that if exhalation and inhalation can be monitored properly, PE existence in the lung can also be detected due to the extremely high dielectric properties of saline. In these measurements, it is observed that variations in the reflection coefficient among individuals and even within the same subject due to the bending in the antenna. Furthermore, the analysis of transmission coefficients in direct channels between antennas demonstrates that the respiration cycle could be accurately tracked. These findings prove the potential of our proposed antenna for detecting and monitoring PE, highlighting its adaptability to diverse body compositions and bending.

REFERENCES

1. World Health Organization, “World Bank and WHO: Half the World Lacks Access to Essential Health Services, 100 Million Still Pushed into Extreme Poverty because of Health Expenses”, 2017, `https://www.who.int/news-room/detail/13-12-2017-world-bank-and-who-half-the-world-lacks-access-to-essential-health-services-100-million-still-pushed-into-extreme-poverty-because-of-health-expenses`, accessed on November 9, 2023.

2. Ladic, K., K. Sayrafian, U. Bengi and S. Dumanli, “A Wearable Wireless Monitoring System for the Detection of Pulmonary Edema”, *2021 IEEE Global Communications Conference*, pp. 1–5, Madrid, Spain, 2021.

3. Otto, C., A. Milenković, C. Sanders and E. Jovanov, “System Architecture of a Wireless Body Area Sensor Network for Ubiquitous Health Monitoring”, *Journal of Multimedia*, Vol. 1, pp. 307–326, 2005.

4. Jung, J., K. Ha, J. Lee, Y. S. Kim and D.-Y. Kim, “Wireless Body Area Network in a Ubiquitous Healthcare System for Physiological Signal Monitoring and Health Consulting”, *International Journal of Signal Processing, Image Processing and Pattern Recognition*, Vol. 1, pp. 47–54, 2008.

5. N. Cho, J. B., T. Roh and H. Yoo, “A Planar MICS Band Antenna Combined With a Body Channel Communication Electrode for Body Sensor Network”, *IEEE Transactions on Microwave Theory and Techniques*, Vol. 57, No. 10, pp. 2515–2522, 2009.

6. National Guideline Centre (UK), *Chronic Heart Failure in Adults: Diagnosis and Management*, National Institute for Health and Care Excellence, London, 2018.

7. Ware, L. B. and M. A. Matthay, “Clinical practice. Acute Pulmonary Edema”, *The New England Journal of Medicine*, Vol. 353, No. 26, pp. 2788–2796, 2005.

8. Jessup, M. and S. Brozena, “Heart Failure”, *The New England Journal of Medicine*, Vol. 348, No. 20, pp. 2007–2018, 2003.

9. Acute Respiratory Distress Syndrome Network, R. G. Brower, M. A. Matthay, A. Morris, D. Schoenfeld, B. T. Thompson and A. Wheeler, “Ventilation with Lower Tidal Volumes as Compared with Traditional Tidal Volumes for Acute Lung Injury and the Acute Respiratory Distress Syndrome”, *The New England Journal of Medicine*, Vol. 342, No. 18, pp. 1301–1308, 2000.

10. Fan, E., D. Brodie and A. S. Slutsky, “Acute Respiratory Distress Syndrome: Advances in Diagnosis and Treatment”, *Journal of the American Medical Association*, Vol. 319, No. 7, p. 698, 2018.

11. Mathhay, M. A., R. L. Zemans, G. A. Zimmerman, Y. M. Arabi, J. R. Beitler, A. Mercait, M. Herridge, A. G. Randolph and C. S. Calfee, “Acute Respiratory Distress Syndrome”, *Nature Reviews. Disease Primers*, Vol. 5, No. 1, p. 18, 2019.

12. Hansell, D. M., A. A. Bankier, H. MacMahon, T. C. McLoud, N. L. Müller and J. Remy, “Fleischner Society: Glossary of Terms for Thoracic Imaging”, *Radiology*, Vol. 246, No. 3, pp. 697–722, 2008.

13. Azlan, M., B. Muneer and B. S. Chowdhry, “Lungs Fluid Accumulation Detection Using Microwave Imaging Technique”, *2022 International Conference on Emerging Technologies in Electronics, Computing and Communication*, pp. 1–4, Jamshoro, Sindh, Pakistan, 2022.

14. Lindow, T., S. Quadrelli and M. Ugander, “Noninvasive Imaging Methods for Quantification of Pulmonary Edema and Congestion: A Systematic Review”, *JACC: Cardiovascular Imaging*, Vol. 16, No. 11, pp. 1469–1484, 2023.

15. Pennati, F., A. Angelucci, L. Morelli, S. Bardini, E. Barzanti, F. Cavallini, A. Conelli, G. D. Federico, C. Paganelli and A. Aliverti, “Electrical Impedance Tomography: From the Traditional Design to the Novel Frontier of Wearables”, *Sensors*, Vol. 23, No. 3, p. 1182, 2023.

16. Trepte, C. J., C. R. Phillips, J. Sola, A. Adler, S. A. Haas, M. Rapin, S. H. Böhm and D. A. Reuter, “Electrical Impedance Tomography (EIT) for Quantification of Pulmonary Edema in Acute Lung Injury”, *Critical Care*, Vol. 20, No. 1, p. 18, 2016.

17. Yang, F., W. Ser, J. Yu, D. C.-G. Foo, D. P. S. Yeo, P.-L. Chia and J. Wong, “Lung Water Detection Using Acoustic Techniques”, *2012 34th Annual International Conference of the IEEE Engineering in Medicine and Biology Society*, pp. 1–4, San Diego, CA, 2012.

18. Januzzi, J. L., R. V. Kimmenade, J. Lainchbury, A. Bayes-Genis, J. Ordonez-Llanos, M. Santalo-Bel, Y. M. Pinto and M. Richards, “NT-proBNP Testing for Diagnosis and Short-Term Prognosis in Acute Destabilized Heart Failure: An International Pooled Analysis of 1256 Patients”, *European Heart Journal*, Vol. 27, No. 3, pp. 330–337, 2006.

19. Bhoil, R., A. Ahluwalia, R. Chopra, M. Surya and S. Bhoil, “Signs and Lines in Lung Ultrasound”, *Journal of Ultrasonography*, Vol. 21, No. 86, pp. 225–233, 2021.

20. Ruben T. Lucassen *et al.*, “Deep Learning for Detection and Localization of B-Lines in Lung Ultrasound”, *IEEE Journal of Biomedical and Health Informatics*, Vol. 27, No. 9, pp. 4352–4361, 2023.

21. Lichtenstein, D. A. and G. A. Meziere, “Relevance of Lung Ultrasound in the Diagnosis of Acute Respiratory Failure*: The BLUE Protocol”, *Chest*, Vol. 134, No. 1, pp. 117–125, 2008.

22. Dumanli, S., "Challenges of Wearable Antenna Design", *2016 46th European Microwave Conference*, pp. 1350–1352, London, United Kingdom, 2016.

23. Augustine Kachiramattom, R., *Electromagnetic Modelling of Human Tissues and Its Application on the Interaction Between Antenna and Human Body in the Ban Context*, Ph.D. Thesis, Université Paris-Est, 2009.

24. Camelia, G., "Compilation of the Dielectric Properties of Body Tissues at RF and Microwave Frequencies.", 1996, `https://api.semanticscholar.org/CorpusID:108808148`, accessed on November 23, 2023.

25. IT'IS Foundation, "It'Is Foundation Dielectric Properties Database", 1999, `https://itis.swiss/virtual-population/tissue-properties/database/`, accessed on November 23, 2023.

26. Li, H.-B., K. Y. Yazdandoost and B. Zhen, *Wireless Body Area Network*, River Publishers, Aalborg, Denmark, 2010.

27. Peyman, A., C. Gabriel and E. Grant, "Complex Permittivity of Sodium Chloride Solutions at Microwave Frequencies", *Bioelectromagnetics*, Vol. 28, No. 4, pp. 264–274, 2007.

28. Feng, Y., S. Wee, Y. Jufeng, D.-G. Foo, D. Yeo, C. Pow-Li and J. Wong, "Lung Water Detection Using Acoustic Techniques", *2012 Annual International Conference of the IEEE Engineering in Medicine and Biology Society*, pp. 4258–4261, San Diego, CA, 2012.

29. Celik, N., R. Gagarin, G. C. Huang, M. F. Iskander and B. W. Berg, "Microwave Stethoscope: Development and Benchmarking of a Vital Signs Sensor Using Computer-Controlled Phantoms and Human Studies", *IEEE Transactions on Biomedical Engineering*, Vol. 61, No. 8, pp. 2341–2349, 2014.

30. Celik, N., R. Gagarin, Y. Hyoung-sun and M. F. Iskander, “A Noninvasive Microwave Sensor and Signal Processing Technique for Continuous Monitoring of Vital Signs”, *IEEE Transactions on Biomedical Engineering*, Vol. 10, No. 1, pp. 286–289, 2011.

31. Mulligan, K., A. Adler and R. Goubran, “Detecting Regional Lung Properties Using Audio Transfer Functions of the Respiratory System”, *2009 Annual International Conference of the IEEE Engineering in Medicine and Biology Society*, pp. 2057–2058, Minneapolis, MN, 2009.

32. Coombs, T., A. Ercole and M. Crisp, “Use of RF Signal Attenuation & Delay for the Detection of Pulmonary Oedema”, *2023 Photonics & Electromagnetics Research Symposium*, pp. 664–671, Prague, Czech Republic, 2023.

33. Leong, C., Y. Xiao, Z. Yun and M. F. Iskander, “Non-Invasive Stethoscope for Continuous Assessment of Lung Water: Towards AI-based Data Augmentation and Prediction”, *2022 IEEE International Symposium on Antennas and Propagation and USNC-URSI Radio Science Meeting*, pp. 341–342, Denver, CO, USA, 2022.

34. Iskander, M. F., C. Leong, P. Shukla, S. Clemens and Z. Yun, “Monitoring COVID-19 Patients Using Cardio-Pulmonary Stethoscope RF Technology: Computer Simulation Study Using CT Scans of Patients”, *IEEE Access*, Vol. 10, No. 1, pp. 103296–103302, 2022.

35. Salman, S., Z. Wang, E. Colebeck, A. Kiourti, E. Topsakal and J. L. Volakis, “Pulmonary Edema Monitoring Sensor With Integrated Body-Area Network for Remote Medical Sensing”, *IEEE Transactions on Antennas and Propagation*, Vol. 62, No. 5, pp. 2787–2794, 2014.

36. Susskind, C., “Possible Use of Microwaves in the Management of Lung Disease”, *Proceedings of the IEEE*, Vol. 61, No. 5, pp. 286–289, 1973.

37. Ahdi Rezaeieh, S., Y.-Q. Tan and A. Abbosh, “Design of Coupling Medium for Pulmonary Edema Microwave Detection System”, *2013 IEEE Antennas and Propagation Society International Symposium*, pp. 2057–2058, Orlando, FL, USA, 2013.

38. Pedersen, P. C., C. C. Johnson, C. H. Durney and D. G. Bragg, “Microwave Reflection and Transmission Measurements for Pulmonary Diagnosis and Monitoring”, *IEEE Transactions on Biomedical Engineering*, Vol. BME-25, No. 1, pp. 40–48, 1978.

39. Ahdi Rezaeieh, S., A. Zamani, K. Bialkowski and A. Abbosh, “Foam Embedded Wideband Antenna Array for Early Congestive Heart Failure Detection With Tests Using Artificial Phantom With Animal Organs”, *IEEE Transactions on Antennas and Propagation*, Vol. 63, No. 11, pp. 5138–5143, 2015.

40. Dogu, S., I. Dilman, M. Cayoren and I. Akduman, “Imaging of Pulmonary Edema with Microwaves — Preliminary Investigation”, *2017 10th International Conference on Electrical and Electronics Engineering*, pp. 1054–1057, Bursa, Turkey, 2017.

41. Ahdi Rezaeieh, S., A. Zamani, K. Bialkowski and A. Abbosh, “Loop-Dipole Composite Antenna for Wideband Microwave-Based Medical Diagnostic Systems With Verification on Pulmonary Edema Detection”, *IEEE Antennas and Wireless Propagation Letters*, Vol. 15, No. 1, pp. 838–841, 2016.

42. Ahdi Rezaeieh, S., A. Zamani, K. Bialkowski, A. Mahmoud and A. Abbosh, “Feasibility of Using Wideband Microwave System for Non-Invasive Detection and Monitoring of Pulmonary Oedema”, *Sci Rep*, Vol. 5, No. 1, p. 14047, 2015.

43. Azlan, M., B. Muneer and B. S. Chowdhry, “Lungs Fluid Accumulation Detection Using Microwave Imaging Technique”, *2022 International Conference on Emerging Technologies in Electronics, Computing and Communication*, pp. 1–4,

Jamshoro, Sindh, Pakistan, 2022.

44. Ertek, D., G. Kucuk and E. Bilgin, “A Microwave Imaging Scheme for Detection of Pulmonary Edema and Hemorrhage”, *2022 30th Signal Processing and Communications Applications Conference*, pp. 1–4, Safranbolu, Turkey, 2022.

45. Ahdi Rezaeieh, S., A. Zamani, K. Bialkowski and A. Abbosh, “Novel Microwave Torso Scanner for Thoracic Fluid Accumulation Diagnosis and Monitoring”, *Scientific Reports*, Vol. 7, No. 1, p. 304, 2017.

46. Ahdi Rezaeieh, S., K. Bialkowski and A. Abbosh, “Microwave System for the Early Stage Detection of Congestive Heart Failure”, *IEEE Access*, Vol. 2, No. 1, pp. 921–929, 2014.

47. Ahdi Rezaeieh, S., A. Zamani, K. Bialkowski, A. Abbosh and Y. Wang, “Wideband Unidirectional Antenna of Folded Structure in Microwave System for Early Detection of Congestive Heart Failure”, *IEEE Transactions on Antennas and Propagation*, Vol. 63, No. 10, pp. 4557–4562, 2015.

48. Zamani, A., A. Darvazehban, S. Ahdi Rezaeieh and A. Abbosh, “Three-Dimensional Electromagnetic Torso Imaging Using Reconfigurable Antennas”, *2019 13th European Conference on Antennas and Propagation*, pp. 1–3, Krakow, Poland, 2019.

49. Kumar, A. and R. K. Badhai, “A Dual-Band On-Body Printed Monopole Antenna for Body Area Network”, *2017 International Conference on Inventive Systems and Control*, pp. 1–5, Coimbatore, India, 2017.

50. Godeneli, K., U. Bengi, O. A. Kati and S. Dumanli, “A Wearable Dual-Mode Repeater Antenna for Implant Communications”, *IEEE Transactions on Antennas and Propagation*, Vol. 70, No. 2, pp. 868–875, 2022.

51. Magill, M. K., G. A. Conway and W. G. Scanlon, “A Wearable Dual-Mode Re-

peater Antenna for Implant Communications", *IEEE Transactions on Antennas and Propagation*, Vol. 68, No. 5, pp. 3515–3524, 2020.

52. Dumanli, S., "A Digitally Assisted Repeater Antenna for Implant Communications", *2017 11th European Conference on Antennas and Propagation*, pp. 181–184, Paris, France, 2017.

53. Wang, J., E. G. Lim, M. P. Leach, Z. Wang, R. Pei, Z. Jiang and Y. Huang, "A 403 MHz Wireless Power Transfer System With Tuned Split-Ring Loops for Implantable Medical Devices", *IEEE Transactions on Antennas and Propagation*, Vol. 70, No. 2, pp. 1355–1366, 2022.

54. Kwon, K., J. Tak and J. Choi, "Design of a Triple-Band On-Body Antenna for a Biomedical Repeater Application", *2013 IEEE Antennas and Propagation Society International Symposium*, pp. 2093–2094, Orlando, FL, USA, 2013.

55. Kiourti, A., J. R. Costa, C. A. Fernandes and K. S. Nikita, "A Broadband Implantable and a Dual-Band On-Body Repeater Antenna: Design and Transmission Performance", *IEEE Transactions on Antennas and Propagation*, Vol. 62, No. 6, pp. 2899–2908, 2014.

56. Xu, L.-J., Z. Duan, Y.-M. Tang and M. Zhang, "A Dual-Band On-Body Repeater Antenna for Body Sensor Network", *IEEE Antennas and Wireless Propagation Letters*, Vol. 15, No. 1, pp. 1649–1652, 2016.

57. Miah, M. S., C. Icheln and K. Haneda, "A Dual-band Repeater Antenna for On-Body Receiver Unit of Wireless Capsule Endoscope", *2020 14th European Conference on Antennas and Propagation*, pp. 1–4, Copenhagen, Denmark, 2020.

58. Blauert, J. and A. Kiourti, "Bio-Matched Horn: A Novel 1–9 GHz On-Body Antenna for Low-Loss Biomedical Telemetry With Implants", *IEEE Transactions on Antennas and Propagation*, Vol. 67, No. 8, pp. 5054–5062, 2019.

59. Felicio, J. M., J. R. Costa and C. A. Fernandes, “Dual-Band Skin-Adhesive Repeater Antenna for Continuous Body Signals Monitoring”, *IEEE Journal of Electromagnetics, RF and Microwaves in Medicine and Biology*, Vol. 2, No. 1, pp. 25–32, 2018.

60. Abbas, S. M., H. Zahra, R. Hashmi, K. P. Eselle and J. L. Volakis, “Compact On-Body Antennas for Wearable Communication Systems”, *2019 International Workshop on Antenna Technology*, pp. 65–66, Miami, FL, USA, 2019.

61. See, T. S. and Z. N. Chen, “Experimental Characterization of UWB Antennas for On-Body Communications”, *IEEE Transactions on Antennas and Propagation*, Vol. 57, No. 4, pp. 866–874, 2009.

62. Dang, Q. H., S. J. Chen, N. Nguyen-Trong and C. Fumeaux, “Multifunctional Reconfigurable Wearable Textile Antennas Using Coplanar Reconfiguration Modules”, *IEEE Transactions on Antennas and Propagation*, Vol. 71, No. 5, pp. 3806–3815, 2023.

63. Gao, G.-P., B. Hu, S.-F. Wang and C. Yang, “Wearable Circular Ring Slot Antenna With EBG Structure for Wireless Body Area Network”, *IEEE Antennas and Wireless Propagation Letters*, Vol. 17, No. 3, pp. 434–437, 2018.

64. Ashyap, A. Y., S. H. B. Dahlan, Z. Z. Abidin, S. K. A. Rahim, H. A. Majid, A. S. M. Alqadami and M. E. Atrash, “Fully Fabric High Impedance Surface-Enabled Antenna for Wearable Medical Applications”, *IEEE Access*, Vol. 9, No. 1, pp. 6948–6960, 2021.

65. Dang, Q. H., S. J. Chen, D. C. Ranasinghe and C. Fumeaux, “A Frequency-Reconfigurable Wearable Textile Antenna With One-Octave Tuning Range”, *IEEE Transactions on Antennas and Propagation*, Vol. 69, No. 12, pp. 8080–8089, 2021.

66. Abbasi, M. A. B., S. S. Nikolaou, M. A. Antoniades, M. Nikolic Stevanovic and P. Vryonides, "Compact EBG-Backed Planar Monopole for BAN Wearable Applications", *IEEE Transactions on Antennas and Propagation*, Vol. 65, No. 2, pp. 453–463, 2017.

67. Watanabe, T. and H. Iwasaki, "Wearable Finger Dual Band Antenna for BAN", *2012 IEEE-APS Topical Conference on Antennas and Propagation in Wireless Communications*, pp. 51–54, Cape Town, WP, South Africa, 2012.

68. Agneessens, S., P. Van Torre, E. Tanghe, G. Vermeeren, W. Joseph and H. Rogier, "On-Body Wearable Repeater as a Data Link Relay for In-Body Wireless Implants", *IEEE Antennas and Wireless Propagation Letters*, Vol. 11, No. 1, pp. 1714–1717, 2012.

69. Alqadami, A., A. Zamani, A. Trakic and A. Abbosh, "Flexible Electromagnetic Cap for Three-Dimensional Electromagnetic Head Imaging", *IEEE Transactions on Biomedical Engineering*, Vol. 68, No. 9, pp. 2880–2891, 2021.

70. Rodriguez-Duarte, D., J. Tobon Vasquez, S. De Luque Arias, R. Scapaticci, L. Crocco and F. Vipiana, "A Portable Microwave Scanner for Brain Stroke Monitoring: Design, Implementation and Experimental Validation", *2022 16th European Conference on Antennas and Propagation*, pp. 1–5, Madrid, Spain, 2022.

71. Hamouda, H., P. Le Thuc, R. Staraj and G. Kossiavas, "Dualband MICS/WIFI Small Antenna for Portable Applications in Telemedicine", *2013 IEEE Antennas and Propagation Society International Symposium*, pp. 2081–2082, Orlando, FL, USA, 2013.

72. Ray, M. K. and K. Mandal, "Shorting Pin and Slot Loaded Dual Band Microstrip Antenna for MICS and GPS Applications", *2018 IEEE Indian Conference on Antennas and Propogation*, pp. 1–4, Hyderabad, India, 2018.

73. Koulouridis, S., G. Kiziltas, Y. Zhou, D. J. Hansford and J. L. Volakis, "Polymer–Ceramic Composites for Microwave Applications: Fabrication and Performance Assessment", *IEEE Transactions on Microwave Theory and Techniques*, Vol. 54, No. 12, pp. 4202–4208, 2006.

74. Shi, Y., L. M. Bhowmik, A. Amert and K. Whites, "An Effective Method for Fabrication of 3-D Dielectric Materials Using Polymer-Ceramic Composites", *2014 IEEE Antennas and Propagation Society International Symposium*, pp. 225–226, Memphis, TN, USA, 2014.

75. Moore, R., "Effects of a Surrounding Conducting Medium on Antenna Analysis", *IEEE Transactions on Antennas and Propagation*, Vol. 11, No. 3, pp. 216–225, 1963.

76. Skrivervik, A. K., M. Bosiljevac and Z. Sipus, "Fundamental Limits for Implanted Antennas: Maximum Power Density Reaching Free Space", *IEEE Transactions on Antennas and Propagation*, Vol. 67, No. 8, pp. 4978–4988, 2019.

77. Gao, M., D. Nikolayev, M. Bosiljevac, Z. Šipuš and A. K. Skrivervik, "Rules of Thumb to Assess Losses of Implanted Antennas", *2021 15th European Conference on Antennas and Propagation*, pp. 1–5, Dusseldorf, Germany, 2021.

78. Gao, M., Z. Šipuš and A. K. Skrivervik, "On the Maximum Power Density of Implanted Antennas within Simplified Body Phantoms", *2022 16th European Conference on Antennas and Propagation*, pp. 1–5, Madrid, Spain, 2022.

79. Jelinek, L., J. Liska, M. Capek, V. Losenicky and M. Gustafsson, "Maximum Radiation Efficiency of Implanted Antennas Employing a Novel Hybrid Method", *2021 IEEE International Symposium on Antennas and Propagation and USNC-URSI Radio Science Meeting*, pp. 1339–1340, Singapore, Singapore, 2021.

80. Liska, J., M. Gao, L. Jelinek, M. Capek and A. Skrivervik, "Maximum Radiation

Efficiency of an Implantable Antenna: The Role of High-Order Modes", *2023 17th European Conference on Antennas and Propagation*, pp. 1–5, Florence, Italy, 2023.

81. Soares, I. V., M. Gao, E. Cil, Z. Šipuš, A. K. Skrivervik, J. S. Ho and D. Nikolayev, "Wireless Powering Efficiency of Deep-Body Implantable Devices", *IEEE Transactions on Microwave Theory and Techniques*, Vol. 71, No. 6, pp. 2680–2692, 2023.

82. Balanis, C. A., *Antenna Theory: Analysis and Design*, John Wiley & Sons, New York, 2016.

83. Volakis, J. L., *Antenna Engineering Handbook*, McGraw-Hill Education, New York, 2007.

84. Stutzman, W. L. and G. A. Thiele, *Antenna Theory and Design*, John Wiley & Sons, Hoboken, 2012.

85. Kraus, J. D., *Antennas For All Applications*, McGraw-Hill, New York, 2002.

86. Chen, W. K., *The Electrical Engineering Handbook*, Elsevier Academic Press, Boston, 2005.

87. Nguyen, V. H., H. P. Phan, M. H. Hoang, D. S. Nguyen, M. C. Dang, T. Nguyen-Tran, N. A. Tran, A. Hoang and E. Fribourg-Blanc, "Improving Radiation Characteristics of UHF RFID Antennas by Zigzag Structures", *The 2011 International Conference on Advanced Technologies for Communications*, pp. 102–105, Da Nang, Vietnam, 2011.

88. Milligan, T. A., *Modern Antenna Design*, John Wiley & Sons, Hoboken, 2005.

89. Wadell, B. C., *Transmission Line Design Handbook*, Artec House, Boston, 2003.

90. Pozar, D. M., *Microwave Engineering*, John Wiley & Sons, Hoboken, 2012.

91. Browne, J., "Broadband Amps Sport Coplanar Waveguide", *Microwaves RF*, Vol. 26, No. 2, pp. 131–134, 1987.

92. Simons, R. N., *Coplanar Waveguide Circuits, Components, and Systems*, John Wiley & Sons, Newark, NJ, 2001.

93. Microwaves101 and EverythingRF, "Coplanar Waveguide Calculator", `https://microwaves101.com/calculators/`, accessed on February 21, 2023.

94. Skrivervik, A. K., M. Bosiljevac, J. Trajkovikj, B. Fuchs and Z. Sipus, "Design Considerations for Wearable Antennas", *2016 URSI International Symposium on Electromagnetic Theory*, pp. 524–527, Espoo, Finland, 2016.

95. Conway, G. A. and W. G. Scanlon, "Antennas for Over-Body-Surface Communication at 2.45 GHz", *IEEE Transactions on Antennas and Propagation*, Vol. 57, No. 4, pp. 844–855, 2009.

96. Paracha, K. N., S. K. Abdul Rahim, P. J. Soh and M. Khalily, "Wearable Antennas: A Review of Materials, Structures, and Innovative Features for Autonomous Communication and Sensing", *IEEE Access*, Vol. 7, No. 1, pp. 56694–56712, 2019.

97. ANSYS, "ANSYS High Frequency Structure Simulator", `http://www.ansys.com/products/electronics/ansys-hfss`, accessed on September, 2019.

98. Peyman, A., C. Gabriel and E. H. Grant, "Complex Permittivity of Sodium Chloride Solutions at Microwave Frequencies", *Bioelectromagnetics*, Vol. 28, No. 4, pp. 264–274, 2007.

99. Mobashsher, A. T. and A. M. Abbosh, "Artificial Human Phantoms: Human Proxy in Testing Microwave Apparatuses That Have Electromagnetic Interaction

with the Human Body", *IEEE Microwave Magazine*, Vol. 16, No. 6, pp. 42–62, 2015.

100. Garcia-Pardo, C., C. Andreu, A. Fornes-Leal, S. Castelló-Palacios, S. Perez-Simbor, M. Barbi, A. Vallés-Lluch and N. Cardona, "Ultrawideband Technology for Medical In-Body Sensor Networks: An Overview of the Human Body as a Propagation Medium, Phantoms, and Approaches for Propagation Analysis", *IEEE Antennas and Propagation Magazine*, Vol. 60, No. 3, pp. 19–33, 2018.

101. Pellegrini, A., A. Brizzi, L. Zhang, K. Ali, Y. Hao, X. Wu, C. C. Constantinou, Y. Nechayev, P. S. Hall, N. Chahat, M. Zhadobov and R. Sauleau, "Antennas and Propagation for Body-Centric Wireless Communications at Millimeter-Wave Frequencies: A Review [Wireless Corner]", *IEEE Antennas and Propagation Magazine*, Vol. 55, No. 4, pp. 262–287, 2013.

102. Guraliuc, A. R., M. Zhadobov, O. De Sagazan and R. Sauleau, "Solid Phantom for Body-Centric Propagation Measurements at 60 GHz", *IEEE Transactions on Microwave Theory and Techniques*, Vol. 62, No. 6, pp. 1373–1380, 2014.

103. Mobashsher, A. T. and A. M. Abbosh, "Three-Dimensional Human Head Phantom With Realistic Electrical Properties and Anatomy", *IEEE Antennas and Wireless Propagation Letters*, Vol. 13, No. 1, pp. 1401–1404, 2014.

104. Cil, E. and S. Dumanli, "Characterization of an Implanted Antenna inside a 3D Printed Multilayer Hip Phantom", *2019 13th European Conference on Antennas and Propagation*, pp. 1–4, Krakow, Poland, 2019.

105. Ruvio, G., R. Solimene, A. Cuccaro, J. E. Browne, D. Gaetano and M. J. Ammann, "Experimental Microwave Breast Cancer Detection with Oil-on-Gelatin Phantom", *2013 International Conference on Electromagnetics in Advanced Applications*, pp. 871–874, Turin, Italy, 2013.

106. Joachimowicz, N., C. Conessa, T. Henriksson and B. Duchêne, “Breast Phantoms for Microwave Imaging”, *IEEE Antennas and Wireless Propagation Letters*, Vol. 13, No. 1, pp. 1333–1336, 2014.

107. Burfeindt, M. J., T. J. Colgan, R. O. Mays, J. D. Shea, N. Behdad, B. D. Van Veen and S. C. Hagness, “MRI-Derived 3-D-Printed Breast Phantom for Microwave Breast Imaging Validation”, *IEEE Antennas and Wireless Propagation Letters*, Vol. 11, No. 1, pp. 1610–1613, 2012.

108. Klemm, M., J. A. Leendertz, D. Gibbins, I. J. Craddock, A. Preece and R. Benjamin, “Microwave Radar-Based Breast Cancer Detection: Imaging in Inhomogeneous Breast Phantoms”, *IEEE Antennas and Wireless Propagation Letters*, Vol. 8, No. 1, pp. 1349–1352, 2009.

109. Çil, E., *A Reconfigurable Wearable Slot Antenna Design Suitable for Smart Glasses*, Master’s Thesis, Boğaziçi University, 2018.

APPENDIX A: LIST OF PUBLICATIONS

This work has been conducted with Kamran Sayrafian and Katjana Krhac, researchers at National Institute of Standards and Technology (NIST). Additionally, fabrication and measurements are supported by TUBITAK 1004 Center of Excellence under project number 22AG016. The resulting publications are listed below:

- **U. Bengi**, K. Krhac, K. Sayrafian, and S. Dumanli, "A Wearable Flexible Loop Antenna for In-Body Beamforming", 2024 IEEE International Symposium on Antennas and Propagation and ITNC-USNC-URSI Radio Science Meeting (AT AP-S), accepted (March 2023).
- **U. Bengi**, B. F. Ozcan, and S. Dumanli, "Utilization of a Novel High-Permittivity Flexible Substrate for the Design of a Wearable Antenna for In-Body Communications", 2023 IEEE International Conference on Mıcrowaves, Communications, Antennas, Biomedical Engineering & Electronics Systems (COMCAS), accepted (July 2023).
- K. Krhac, **U. Bengi**, S. Dumanli, and K. Sayrafian, "A Wearable Wireless Monitoring System for the Detection of Pulmonary Edema", 2021 IEEE Global Communication Conference, published (February 2022).
- **U. Bengi**, B. F. Ozcan, and S. Dumanli, "Beden İçi İletişim için Giyilebilir Anten Tasarımında Yüksek Dielektrik Sabitli Esnek Alttaş Kullanımı", 2023 URSI Turkey Scientific Congress and National General Assembly, published (September 2023).

APPENDIX B: COPYRIGHT PERMISSION

Figure 1.1 has been sourced from the research presented in [7]. Permission for its inclusion has been granted by the Massachusetts Medical Society (MMS), the publisher of the New England Journal of Medicine. In order to use content from publications of MMS in a thesis, one should include the consent sentence below in their work:

Figure 1.1 is reproduced with explicit permission obtained from [7], under the copyright of the Massachusetts Medical Society.

APPENDIX C: USE OF PRODUCTIVE ARTIFICIAL INTELLIGENCE

In this thesis, ChatGPT developed by OpenAI was used for language refinement and text editing purposes.